THE EUROPEAN
PHYSICAL JOURNAL C

In situ calibration of large-radius jet energy and mass in 13 TeV proton–proton collisions with the ATLAS detector

ATLAS Collaboration[*]

CERN, 1211 Geneva 23, Switzerland

Abstract The response of the ATLAS detector to large-radius jets is measured in situ using 36.2 fb^{-1} of $\sqrt{s} = 13$ TeV proton–proton collisions provided by the LHC and recorded by the ATLAS experiment during 2015 and 2016. The jet energy scale is measured in events where the jet recoils against a reference object, which can be either a calibrated photon, a reconstructed Z boson, or a system of well-measured small-radius jets. The jet energy resolution and a calibration of forward jets are derived using dijet balance measurements. The jet mass response is measured with two methods: using mass peaks formed by W bosons and top quarks with large transverse momenta and by comparing the jet mass measured using the energy deposited in the calorimeter with that using the momenta of charged-particle tracks. The transverse momentum and mass responses in simulations are found to be about 2–3% higher than in data. This difference is adjusted for with a correction factor. The results of the different methods are combined to yield a calibration over a large range of transverse momenta (p_T). The precision of the relative jet energy scale is 1–2% for 200 GeV $< p_T < 2$ TeV, while that of the mass scale is 2–10%. The ratio of the energy resolutions in data and simulation is measured to a precision of 10–15% over the same p_T range.

1 Introduction

Signatures with high p_T, massive particles such as Higgs bosons, top quarks, and W or Z bosons have become ubiquitous during Run 2 of the Large Hadron Collider (LHC). These particles most often decay hadronically. Due to their large transverse momentum, the decay products become collimated and may be reconstructed as a single jet with large radius parameter R [1,2] (a 'large-R' jet). The sensitivity of searches and measurements that use large-R jets depends on an accurate knowledge of the transverse momentum p_T and mass m responses of the detector [3]. A calibration of the

large-R energy and mass scales derived using Monte Carlo simulation yields uncertainties as large as 10%. The calibration described in this paper results in a reduction of these uncertainties by more than a factor of three.

In this paper, a suite of in situ calibration techniques is described which measure the response in proton–proton (pp) collision data at $\sqrt{s} = 13$ TeV. The results of several methods are combined to provide a calibration that defines the nominal large-R jet energy scale (JES) and the jet mass scale (JMS). These measurements provide a significant increase in the precision with which the large-R jet p_T and mass scales are known across most of the kinematically accessible phase space. The jet energy and mass resolutions (JER, JMR) are also measured in situ and compared with the predictions of Monte Carlo simulations (MC). Additional uncertainties on jet substructure observables used to identify boosted objects are derived from data in Ref. [4].

Jet reconstruction starts with clusters of topologically connected calorimeter cell signals. These topological clusters, or 'topo-clusters', are brought to the hadronic scale using the local hadronic cell weighting scheme (LCW) [5]. Large-R jets are reconstructed with the anti-k_t algorithm [6] using a radius parameter $R = 1.0$. The jets are groomed with the 'trimming' algorithm of Ref. [7], which removes regions of the jet with a small relative contribution to the jet transverse momentum. This procedure reduces the impact from additional pp interactions in the event and from the underlying event, improving the energy and mass resolution.

The several stages of the ATLAS large-R jet calibration procedure are illustrated in Fig. 1. The trimmed large-R jets are calibrated to the energy scale of stable final-state particles using corrections based on simulations. This jet-level correction is referred to as the simulation-based calibration and includes a correction to the jet mass [8]. Finally, the jets are calibrated in situ using response measurements in pp collision data. A correction based on a statistical combination of data-to-simulation ratios of these response measurements is applied only to data and adjusts for the residual (typically 2–3%) mismodelling of the response. Uncertainties in the JES
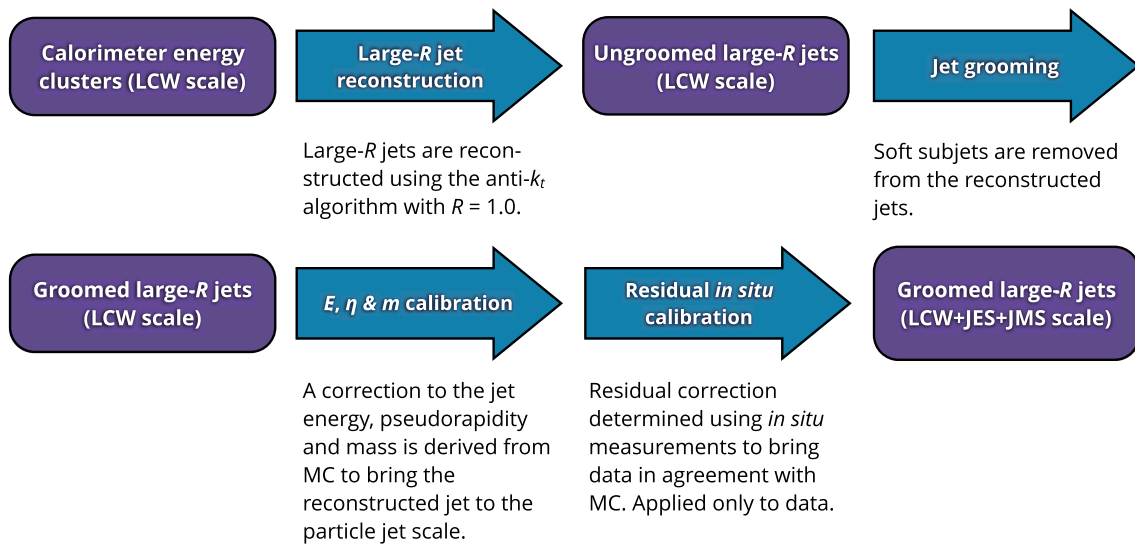
[*] e-mail: atlas.publications@cern.ch

Fig. 1 Overview of the large-R jet reconstruction and calibration procedure described in this paper. The calorimeter energy clusters from which jets are reconstructed have already been adjusted to point at the event's primary hard-scatter vertex

Fig. 2 Schematic representation of the events used to measure the JES and JER: **a** a dijet event, **b** a Z+jet or γ+jet event and **c** a multijet event with several jets recoiling against the leading (large-R) jet. The labels J_i refer to the ith leading large-R jet, while j_i refers to the ith leading small-R jet that fulfils $\Delta R(J_1, j) > 1.4$. $\Delta\phi$ is the difference between the azimuthal angle of the jet and the reference object, while $\Delta\alpha$ is the difference between the azimuthal angle of the jet and the vectorial sum of the recoil system momenta

(a) dijet event   **(b)** Z+jet or γ+jet event   **(c)** multijet event
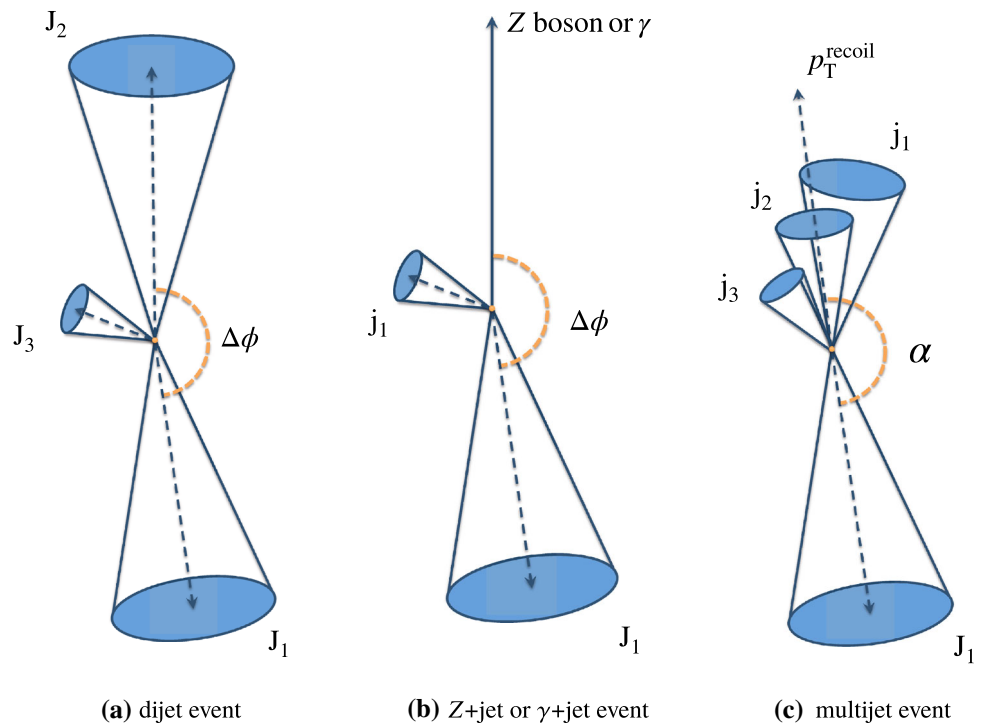
and JMS are derived by propagating uncertainties from the individual in situ response measurements through the statistical combination.

The in situ calibration is determined in two separate steps. In the first step, the JES is measured with the same methods used to calibrate small-R jets [9]. These techniques rely on the transverse momentum balance in a variety of final states, illustrated in Fig. 2. The JES correction factor is a product of two terms. The absolute calibration is derived from a statis-

tical combination of three measurements from Z+jet, γ+jet, and multijet events in the central region of the detector. A relative intercalibration, derived using dijet events, propagates the well-measured central JES into the forward region of the detector. The in situ calibration accounts for detector effects which are not captured by simulation. The JES correction is applied as a four-momentum scale factor to jets in data; therefore, it also affects the jet mass calibration.

In the second step of the in situ calibration, the jet mass response is measured using two methods following the application of the in situ JES correction. The mass response is measured in lepton+jets top quark pair production ($t\bar{t}$ production) [10] with a fit to the peaks in the jet mass distribution formed by high-p_T W bosons and top quarks decaying into fully hadronic final states. A second measurement is performed with the R_{trk} method [3], which takes advantage of the independent measurements by the calorimeter and the inner tracker. This method provides a calibration for the calorimeter jet mass measurement over a broad p_T range. The results from the two methods are combined as a smooth function of p_T in two mass bins, which could be applied to data as an in situ correction as outlined in Sect. 8.

The JER and JMR are also measured in situ and compared with the prediction of the simulation. The dijet balance method takes advantage of the transverse momentum balance in dijet events to extract the JER. The JMR is obtained from fits to the top quark and W boson mass peaks in high-p_T lepton+jets $t\bar{t}$ events.

Sections 2 and 3 provide overviews of the ATLAS detector, the data set studied, and the simulations used in this paper. Section 4 describes the reconstruction of large-R jets in ATLAS. The following section presents the results of the balance methods that measure the jet energy scale: the intercalibration, which uses dijet events to ensure a uniform response over the central and forward regions of the detector in Sect. 5.1, the Z+jet balance method in Sect. 5.2, the γ+jet balance method in Sect. 5.3, and the multijet balance method in Sect. 5.4. Section 6 presents the methods that are used to measure the jet mass response: the R_{trk} method and its results for the energy and mass scale in Section 6.1 and the fits to the W boson and top quark mass peaks in high-p_T lepton+jets $t\bar{t}$ events in Sect. 6.2, which are also used to measure the JMR. The measurement of the JER in dijet events is discussed in Sect. 7. The methodology of the combination procedure is presented in Sect. 8, as well as the resultant combined in situ calibration of the JES and JMS. Sect. 9 summarizes the results.

2 The ATLAS detector and data set

The ATLAS experiment consists of three major sub-detectors: the inner detector, the calorimeters, and the muon spectrometer. The inner detector, closest to the interaction point, is used to track charged particles in a 2 T axial magnetic field produced by a thin superconducting solenoid. It consists of a pixel detector, a silicon tracker equipped with micro-strip detectors, and a transition radiation tracker that provides a large number of space points in the outermost layers of the tracker. It covers the pseudorapidity[1] range $|\eta| < 2.5$. Surrounding the tracker and solenoid, a sampling calorimeter measures the energy of particles produced in the collisions with $|\eta| < 4.9$. The energies of electrons and photons are measured precisely in a high-granularity liquid-argon electromagnetic calorimeter. The cylindrical "barrel" covers $|\eta| < 1.475$, and the "endcaps" on either end of the detector cover $1.375 < |\eta| < 3.2$. An iron/scintillator tile calorimeter measures the energy of hadrons in the central rapidity range, $|\eta| < 1.7$, and a liquid-argon hadronic endcap calorimeter provides coverage for $1.5 < |\eta| < 3.2$. The forward liquid-argon calorimeter measures electrons, photons, and hadrons for $3.2 < |\eta| < 4.9$. Finally, a muon spectrometer in the magnetic field of a system of superconducting air-core toroid magnets identifies muons in the range $|\eta| < 2.7$ and measures their transverse momenta. The ATLAS trigger system consists of a hardware-based first-level trigger followed by a software-based high-level trigger, which apply a real-time selection to reduce the up to 40 MHz LHC collision rate to an average rate of events written to storage of 1 kHz [11]. A detailed description of the ATLAS experiment is given in Ref. [12].

The data set used in this analysis consists of pp collisions delivered by the LHC at a centre-of-mass energy of $\sqrt{s} = 13$ TeV during 2015 and 2016. The specific trigger requirements vary among the various in situ analyses and are described in the relevant sections. All data are required to meet ATLAS standard quality criteria. Data taken during periods in which detector subsystems were not fully functional are discarded. Data quality criteria also reject events that have significant contamination from detector noise or with issues in the read-out. The remaining data correspond to an integrated luminosity of 36.2 fb^{-1}.

Due to the high luminosity of the LHC, multiple pp collisions occur during each bunch crossing. Interactions which occur within the bunch crossing of interest (in-time pile-up) or in neighbouring bunch crossings (out-of-time pile-up) may alter the measured energy or mass scale of jets or lead to the reconstruction of additional 'stochastic' jets, seeded by upwards fluctuations in the local pile-up energy density. The average number of additional pp collisions per bunch crossing is 24 in the Run 2 data from 2015 and 2016 analysed here.

---

[1] The ATLAS reference system is a Cartesian right-handed coordinate system, with the nominal collision point at the origin. The anticlockwise beam direction defines the positive z-axis, while the positive x-axis is defined as pointing from the collision point to the centre of the LHC ring and the positive y-axis points upwards. The azimuthal angle ϕ is measured around the beam axis, and the polar angle θ is measured relative to the z-axis. Pseudorapidity is defined as $\eta = -\ln[\tan(\theta/2)]$, and transverse energy is defined as $E_T = E \sin\theta$.

3 Simulations

The data are compared with detailed simulations of the ATLAS detector response [13] based on the Geant4 [14] toolkit. Hard-scatter events for all processes studied were simulated with several different event generators to assess possible systematic effects due to limitations in the physics modelling. Several different simulation packages were also used to hadronize final-state quarks and gluons in order to compare the impact of various models of hadronization and parton showering on the measurements.

Dijet events were generated using several different generator configurations. Depending on the analysis, nominal dijet samples were generated using either PYTHIA 8 (v8.186) [15] or POWHEG- BOX 2.0 [16–18] interfaced with PYTHIA 8. These samples were generated with the A14 set of tuned parameters [19] and the NNPDF2.3 LO parton distribution function (PDF) set [20]. Samples generated with HERWIG 7 [21] and SHERPA v2.1 [22] were used for comparison. The HERWIG 7 sample used the UE-EE-5 set of tuned parameters [23] and CTEQ6L1 PDF set [24]. The SHERPA leading-order multileg generator includes $2 \rightarrow 2$ and $2 \rightarrow 3$ processes at matrix element level, combined using the CKKW prescription [25].

Z+jets events are generated using POWHEG- BOX 2.0 interfaced to the Pythia 8.186 parton shower model. The CT10 PDF set is used in the matrix element [26]. The AZNLO set of tuned parameters [27] is used, with PDF set CTEQ6L1, for the modelling of non-perturbative effects. The EvtGen 1.2.0 program [28] is used for the properties of b- and c-hadron decays. Photos++ 3.52 [29] is used for QED emissions from electroweak vertices and charged leptons. Samples of Z+jet events are compared to a second sample generated using SHERPA 2.2.1. Matrix elements are calculated for up to 2 partons at NLO and 4 partons at LO using Comix [30] and OpenLoops [31] and merged with the SHERPA parton shower [32] according to the ME+PS@NLO prescription [33]. The NNPDF30nnlo PDF set is used in conjunction with dedicated parton shower tuning developed by the SHERPA authors. γ+jets events are compared to a sample generated with the SHERPA 2.1.1 event generator. Matrix elements are calculated with up to 3 or 4 partons at LO and merged with the SHERPA parton shower according to the ME+PS@LO prescription. The CT10 PDF set is used in conjunction with dedicated parton shower tuning developed by the SHERPA authors. Z+jets events are generated using POWHEG- BOX 2.0 interfaced to the Pythia 8.186 parton shower model. The CT10 PDF set is used in the matrix element [26]. The AZNLO set of tuned parameters [27] is used, with PDF set CTEQ6L1, for the modelling of non-perturbative effects. The EvtGen 1.2.0 program [28] is used for the properties of b- and c-hadron decays. Photos++ 3.52 [29] is used for QED emissions from electroweak

vertices and charged leptons. Samples of Z+jet events are compared to a second sample generated using SHERPA 2.2.1. Matrix elements are calculated for up to 2 partons at NLO and 4 partons at LO using Comix [30] and OpenLoops [31] and merged with the SHERPA parton shower [32] according to the ME+PS@NLO prescription [33]. The NNPDF30nnlo PDF set is used in conjunction with dedicated parton shower tuning developed by the SHERPA authors. γ+jets events are compared to a sample generated with the SHERPA 2.1.1 event generator. Matrix elements are calculated with up to 3 or 4 partons at LO and merged with the SHERPA parton shower according to the ME+PS@LO prescription. The CT10 PDF set is used in conjunction with dedicated parton shower tuning developed by the SHERPA authors.

For γ+jet events, PYTHIA 8 was used as the nominal generator, where the $2 \rightarrow 2$ matrix element is convolved with the NNPDF2.3LO PDF set. The A14 event tune was used. These events are compared to a sample generated with SHERPA v2.1.1, which includes up to four jets in the matrix element. These events were generated using the default SHERPA tune and the CT10 PDF set.

Top quark pair production and single top production in the s-channel and Wt final state were simulated at NLO accuracy with POWHEG- BOX v2 [34] and the CT10 PDF set. For electroweak t-channel single top quark production, POWHEG- BOX v1 was used, which utilizes the four-flavour scheme for NLO matrix element calculations together with the fixed four-flavour PDF set CT10f4. In all cases, the nominal sample was interfaced with PYTHIA 8 with the CTEQ6L1 PDF set, which simulates the parton shower, fragmentation, and underlying event. The h_{damp} parameter in POWHEG, which regulates the p_{T} of the first additional emission beyond the Born level and thus the p_{T} of the recoil emission against the $t\bar{t}$ system, was set to the mass of the top quark (172.5 GeV). Systematic uncertainties in the modelling of hadronization were evaluated using a POWHEG sample interfaced to HERWIG 7. W+jet events, simulated in SHERPA v2.2.0, are considered as a background to $t\bar{t}$ production.

The effect of pile-up on reconstructed jets was modelled by overlaying multiple simulated minimum-bias inelastic pp events on the signal event. These additional events were generated with PYTHIA 8, using the A2 set of tuned parameters [35] and MSTW2008LO PDF set [36]. The distribution of the average number of interactions per bunch crossing in simulated samples is reweighted to match that of the analyzed dataset.

4 Large-R jet reconstruction and simulation calibration

This section describes the reconstruction of large-R jets and the grooming procedure. Three classes of jets are used: calorimeter jets, particle-level (or 'truth') jets, and track

jets. The large-R jets considered in this paper are reconstructed using the anti-k_t algorithm [6] with a radius parameter $R = 1.0$. For balancing and veto purposes, jets reconstructed with radius parameter $R = 0.4$ ('small-R jets') are used in some parts of the analysis with their own calibration procedures applied [9]. The specific implementation of the jet clustering algorithm used is taken from the FASTJET package [37,38].

4.1 Large-R jets

Calorimeter jets are formed from topological clusters of calorimeter cells. The clusters are seeded by cells with an energy significantly above the calorimeter noise. The large-R jets used in this paper are reconstructed using topological clusters that are calibrated to correct for response differences between energy deposition from electromagnetic particles (electrons and photons) and hadrons with the LCW scheme of Ref. [5]. Small-R jets reconstructed from "electromagnetic scale" topo-clusters are used as a reference system in the multijet balance method of Sect. 5.4. Results are labelled with "LCW" or "EM" to indicate the calibration of the clusters. Topological clusters are defined to be massless. The four-momenta of these topo-clusters, initially defined as pointing to the geometrical centre of the ATLAS detector, are adjusted to point towards the hard-scatter primary vertex of the event, which is defined as the primary vertex with the largest associated sum of track p_T^2.

To reduce the effects of pile-up, soft emissions, and the underlying event on jet substructure measurement, the trimming algorithm is applied to the jets. Trimming reclusters the jet constituents of each $R = 1.0$ jet using the k_t algorithm [39] and $R_{sub} = 0.2$, producing a collection of subjets for each jet. Subjets with $p_T^{subjet}/p_T^{jet} < 0.05$ are removed, and the jet four-momentum is recalculated from the remaining constituents.

In this paper, trimmed large-R jets with $p_T > 200$ GeV and $|\eta| < 2.5$ are studied.

4.2 Particle-level jets and the simulation-based jet calibration

The reference for the simulation-based jet calibration is formed by particle-level jets. These are created by clustering stable particles originating from the hard-scatter interaction in the simulation event record which have a lifetime τ in the laboratory frame such that $c\tau > 10$ mm. Particles that do not leave significant energy deposition in the calorimeter (i.e. muons and neutrinos) are excluded. Particle-level jets are reconstructed and trimmed using the same algorithms as those applied to large-R jets built from topological clusters,

incorporating the grooming procedure within the jet definition.

After reconstruction of the calorimeter jets, a correction derived from a sample of simulated dijet events is applied to restore the average reconstructed calorimeter jet energy scale to that of particle-level jets. A correction is also applied to the η of the reconstructed jet to correct for a bias relative to particle-level jets in certain regions of the detector [40]. Both corrections are applied as a function of the reconstructed jet energy and the detector pseudorapidity, η_{det}, defined as the pseudorapidity calculated relative to the geometrical centre of the ATLAS detector. This yields a better location of the energy-weighted centroid of the jet than the use of the pseudorapidity calculated relative to the hard-scatter primary vertex.

Reconstructed jets are matched to particle-level jets using an angular matching procedure that minimizes the distance $\Delta R = \sqrt{(\Delta \phi)^2 + (\Delta \eta)^2}$. The energy response is defined as E_{reco}/E_{truth}, where E_{reco} is the reconstructed jet energy prior to any calibration (later denoted E_0) and E_{truth} is the energy of the corresponding particle-level jets. The mass response is defined as m_{reco}/m_{truth}, where m_{reco} and m_{truth} represent the jet mass of the matched detector-level and particle-level jets, respectively. The average response is determined in a Gaussian fit to the core of the response distribution. The parameterization of the average jet energy response $R_E = \langle E_{reco}/E_{truth} \rangle$ used for the simulation calibration is presented as a function of η_{det} and for several values of the truth jet energy in Fig. 3a. The correction is typically 5–10%, with a weak dependence on the jet energy and a characteristic structure in η_{det} that reflects the calorimeter geometry.

The simulation-based JES correction factor c_{JES} is determined as a function of the jet energy and pseudorapidity η_{det}. It is applied to the jet four-momentum as a multiplicative scale factor. The pseudorapidity correction $\Delta \eta$ only changes the direction. This means that the reconstructed large-R jet energy, mass, η, and p_T become

$$E_{reco} = c_{JES} E_0, \quad m_{reco} = c_{JES} m_0, \quad \eta_{reco} = \eta_0 + \Delta \eta,$$
$$p_T^{reco} = c_{JES} |\vec{p}_0|/\cosh(\eta_0 + \Delta \eta),$$

where the quantities E_0, m_0, η_0, and $\vec{p}_0$ refer to the jet properties prior to any calibration, as determined by the trimming algorithm. The quantities c_{JES} and $\Delta \eta$ are smooth functions of the large-R jet kinematics. None of the calibration steps affect the azimuthal angle ϕ of the jet.

The large-R jet invariant mass is calibrated in a final step. This is important when using the jet mass in physics analyses, because the jet mass is more sensitive than the transverse momentum to soft, wide-angle contributions and to cluster merging and splitting, as well as to the calorimeter geometry. For the mass correction the jet mass response $R_m = \langle m_{reco}/m_{truth} \rangle$ is determined using the same proce-

(a)
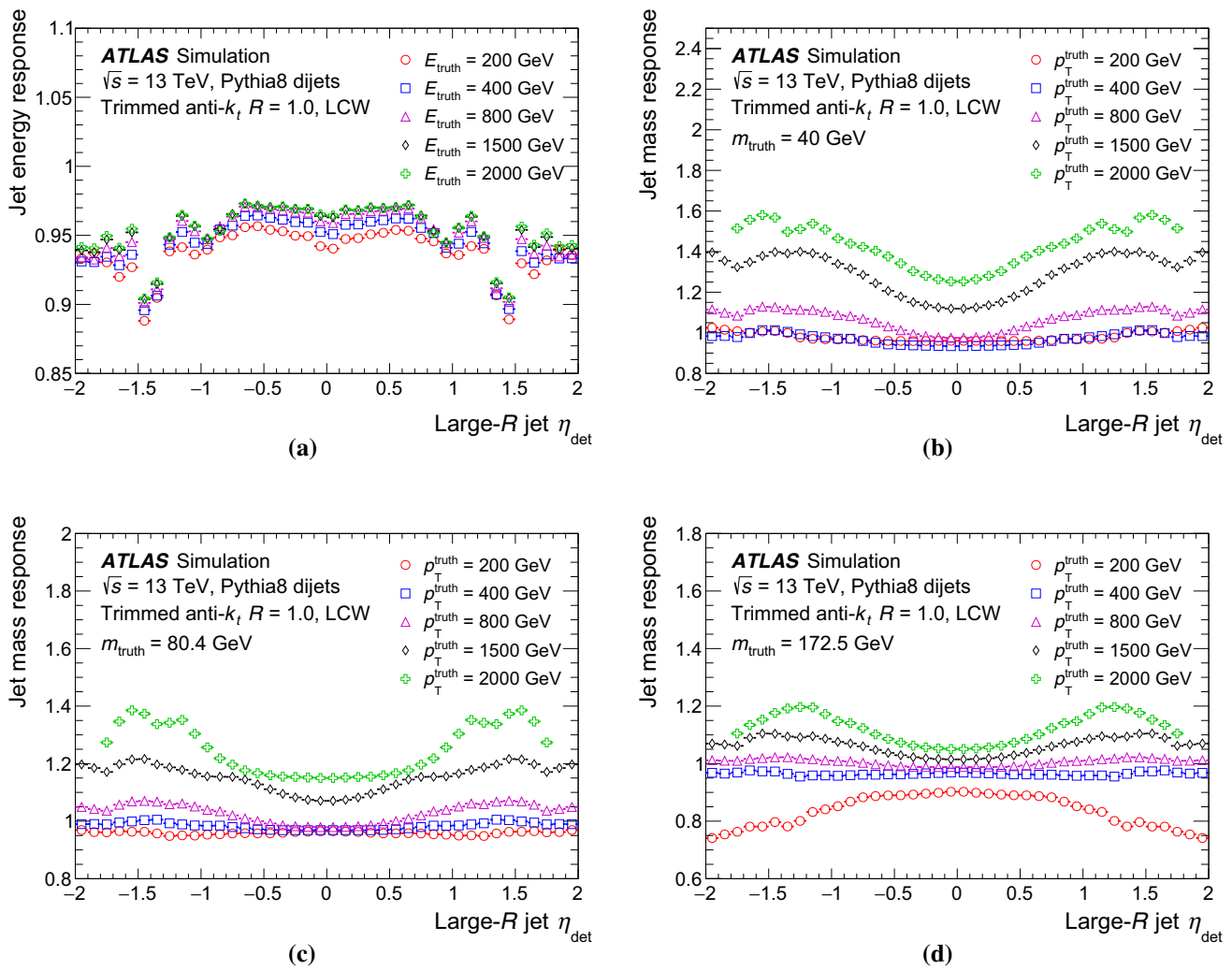

(b)

(c)

(d)

Fig. 3 The response for **a** the jet energy and **b–d** the jet mass of large-R jets. The jet energy response is presented as a function of jet detector pseudorapidity η_{det} for several values of the truth jet energy, ranging from 200 GeV to 2 TeV. The jet mass response is presented as a function of jet pseudorapidity for several values of the jet transverse momentum from 200 GeV to 2 TeV and for three representative values of the truth jet mass: **b** 40 GeV, representing a typical value for quark or gluon jets, **c** the W boson mass, and **d** the top quark mass. The response is determined in simulation of dijet events as the ratio of the reconstructed jet mass to the mass of the corresponding particle-level jet. These results are used to define the jet-level mass correction applied in the simulation calibration

dure as for the jet energy calibration. The mass calibration is applied after the standard JES calibration. The mass response is presented in Fig. 3 for three representative values of the truth jet mass: 40 GeV in panel (b), the W boson mass in panel (c), and the top quark mass in panel (d). The mass response is close to unity for jets with p_T between 200 and 800 GeV and as large as 1.5 for very energetic jets with relatively low mass. Several effects can impact the jet mass response. The reconstructed mass can be artificially increased by the splitting of topo-clusters during their creation. This effect is particularly important for jets with small particle-level mass relative to their p_T ($m/p_T \lesssim 0.05$). Similarly, when several particles form one topo-cluster, or when particles fail to produce any topo-cluster, the mass response is decreased. This effect is significant for jets with large particle-level mass relative to their p_T ($m/p_T \gtrsim 0.5$).

The simulation-based correction to the large-R jet mass c_{JMS} is applied as a function of the jet E_{reco}, η_{det}, and $\log(m_{\text{reco}}/E_{\text{reco}})$, keeping the large-$R$ jet energy fixed and thus allowing the p_T to vary [40]. This factor is also a smooth function of the large-R jet kinematics. This has the following impact on the reconstructed jet kinematics:

$$E_{\text{reco}} = c_{\text{JES}} E_0, \ m_{\text{reco}} = c_{\text{JES}} c_{\text{JMS}} m_0, \ \eta_{\text{reco}} = \eta_0 + \Delta\eta,$$
$$p_T^{\text{reco}} = c_{\text{JES}}\sqrt{E_0^2 - c_{\text{JMS}}^2 m_0^2}/\cosh(\eta_0 + \Delta\eta).$$

All results that correspond to jets that are brought to the particle-level with the simulation-based calibration are labelled with "JES+JMS".

4.3 Tracks and track jets

Tracks are reconstructed from the hits generated by charged particles passing through the inner tracking detector (ID). They are required to have $p_T > 500$ MeV. To reduce fake tracks, candidate tracks must be composed of at least one pixel detector hit and at least six hits in the silicon tracker. The track transverse impact parameter $|d_0|$ relative to the primary vertex must be less than 1.5 mm and the longitudinal impact parameter $|z_0|$ multiplied by $\sin \theta$ relative to the primary vertex must be less than 3 mm [41,42].

Jets reconstructed from charged-particle tracks are used as a reference in calibration and uncertainty studies, taking advantage of the independence of instrumental systematic effects between the ID and the calorimeter. Track jets are reconstructed by applying the same jet reconstruction procedure to tracks as those used when constructing the topo-cluster jets described above, including the jet trimming algorithm. Track jets are not calibrated.

4.4 The combined jet mass

The jet mass resolution is improved by combining the jet mass measurement in the calorimeter with the measurement of the charged component of the jet within the ID [43–51]. A track jet is reconstructed from ID tracks with $p_T > 500$ MeV which are ghost-associated [52] to the topo-cluster large-R jet. The measurement of this track jet's mass is multiplied by the ratio of the transverse momenta of the calorimeter jet and the track jet to obtain the track-assisted mass:

$$m^{TA} = m^{track} \frac{p_T^{calo}}{p_T^{track}}. \tag{1}$$

where m^{TA} is the track-assisted mass, m^{track} the mass obtained from the tracker, and p_T^{calo} and p_T^{track} are the transverse momenta measured respectively by the calorimeter and tracker. This alternative mass measurement has better resolution for high-p_T jets with low values of m/p_T. A weighted least-squares combination of the mass measurements is subsequently performed with weights:

$$m^{comb} = w_{calo} m^{calo} + w_{TA} m^{TA},$$

where w_{calo} and w_{TA} are determined by the expected mass resolutions σ_{calo} and σ_{TA} of the calorimeter and track-assisted measurements, using the central 68% inter-quantile range of the jet mass response distribution in dijet events:

$$w_{calo} = \frac{\sigma_{calo}^{-2}}{\sigma_{calo}^{-2} + \sigma_{TA}^{-2}}, \quad w_{TA} = \frac{\sigma_{TA}^{-2}}{\sigma_{calo}^{-2} + \sigma_{TA}^{-2}},$$

such that the resolution of the combined mass measurement is always better than either of the two inputs within the sample from which the weights are derived. In this paper, in situ measurements are presented for the jet mass reconstructed from topo-clusters and for the track-assisted mass. The constraint $w_{calo} + w_{TA} = 1$ ensures that the combined mass is calibrated, if the scales of both mass definitions are fixed.

5 In situ p_T response measurements

In this section, the methods used to derive the in situ calibration for the energy (or transverse momentum) response are presented. These methods use p_T conservation in events where a large-R jet recoils against a well-measured reference object. The first method is based on the p_T balance in dijet events with a central ($|\eta_{det}| \leq 0.8$) and a forward ($|\eta_{det}| > 0.8$) jet. It is applied after the simulation calibration described in Sect. 4. The η-intercalibration corrects the p_T of forward jets to make the jet energy response uniform as a function of pseudorapidity. After the η-intercalibration procedure, three further balance methods are used to provide an absolute p_T scale calibration. In the Z+jet balance method, the recoiling system is a reconstructed $Z \to \mu^+ \mu^-$ or $Z \to e^+ e^-$ decay, in the γ+jet balance method it is a photon, and in the multijet balance method the system is formed by several calibrated small-R jets with low p_T. These three methods offer complementary coverage over a broad p_T range. The Z+jet balance method provides the most precise results in the low-p_T interval between 200 and 500 GeV, the γ+jet balance between 500 GeV and 1 TeV, and the multijet balance extends to 2.5 TeV. Results of the three methods are presented in this section and are combined into a global constraint on the JES in Sect. 8.

5.1 Dijet η-intercalibration

The relative η-intercalibration extends the jet calibration to the forward detector region, $0.8 < |\eta| < 2.5$. It is derived from the differences in the p_T balance between a central reference and a forward jet in data and simulations. The η-intercalibration is determined in dijet events using a procedure similar to that used for small-R jets [53]. The p_T balance of the dijet system is characterized by its asymmetry $\mathcal{A}$, defined in terms of the forward (probe) and central (reference) jet p_T (p_T^{probe} and p_T^{ref}) as

$$\mathcal{A} = \frac{p_T^{probe} - p_T^{ref}}{p_T^{avg}},$$

where $p_T^{avg} = (p_T^{probe} + p_T^{ref})/2$. The central reference jets are required to be within $|\eta| < 0.8$. The balancing probe jet η_{det}

Table 1 Summary of the dijet topology selection and systematic variations considered for the η-intercalibration analysis. The label J$_3$ refers to the third trimmed $R = 1.0$ jet in the event after ordering the jets in p_T

Variable	Nominal selection	Up variation	Down variation
$p_T^{J_3}/p_T^{avg}$	< 0.4	< 0.5	< 0.3
$\Delta\phi(\text{ref}, \text{probe})$	> 2.5	> 2.8	> 2.2

defines the detector region whose response is being probed. The asymmetry distribution is studied in bins of p_T^{avg} and the probe jet η_{det}. In each bin, the relative response difference between the central and forward jets is

$$R_{rel} = \left\langle \frac{p_T^{probe}}{p_T^{ref}} \right\rangle = \frac{2 + \langle \mathcal{A} \rangle}{2 - \langle \mathcal{A} \rangle}, \tag{2}$$

where $\langle \mathcal{A} \rangle$ is the mean value of the asymmetry. The asymmetry distribution is approximately Gaussian, and the mean value is extracted using a Gaussian fit to the core of the distribution.

Large-R jets with p_T from 180 GeV to 2 TeV within $|\eta| < 2.5$ are considered. Dijet events in data are selected using several dedicated single-jet triggers based on small-R jets. Their efficiency has been evaluated for large-R jets and each trigger is used in its region of full efficiency for those jets. These triggers provide enough events for this technique

to be used over a wide range of p_T. To ensure a $2 \rightarrow 2$ body topology, events with energetic additional radiation are vetoed with an upper cut on the transverse momentum of the third jet J_3, and the leading two jets are required to satisfy a minimum angular separation in azimuth. Both of these requirements are varied in order to derive systematic uncertainties accounting for their impact on the response measurements. These selections and systematic variations are summarized in Table 1. No pile-up jet tagging employing the Jet Vertex Tagger likelihood measure (JVT) [54,55] is applied for large-R jets, since in this kinematic region the contamination by pile-up jets is negligible.

The relative jet-p_T response R_{rel} is shown in Fig. 4 as a function of the large-R jet pseudorapidity for data, POWHEG+PYTHIA 8, and SHERPA for two p_T intervals. The relative jet response as a function of the large-R jet p_T is shown in Fig. 5 for two pseudorapidity ranges of the probe jet. In the central region, the relative responses of all three samples agree by design. The relative response in data increases in the forward region due to features of the experimental response which are not well-reproduced in the simulation and hence not accounted for in the simulation-based JES calibration factor c_{JES}. Compared to the measured response, the prediction remains relatively constant around unity. The difference between the simulated and measured responses reaches about 5% around $|\eta| = 2.5$. Similar trends are observed for $R = 0.4$ jets in Ref. [9]. In the lower panel of Figs. 4 and 5, the ratio of simulation to data is shown. An interpolation
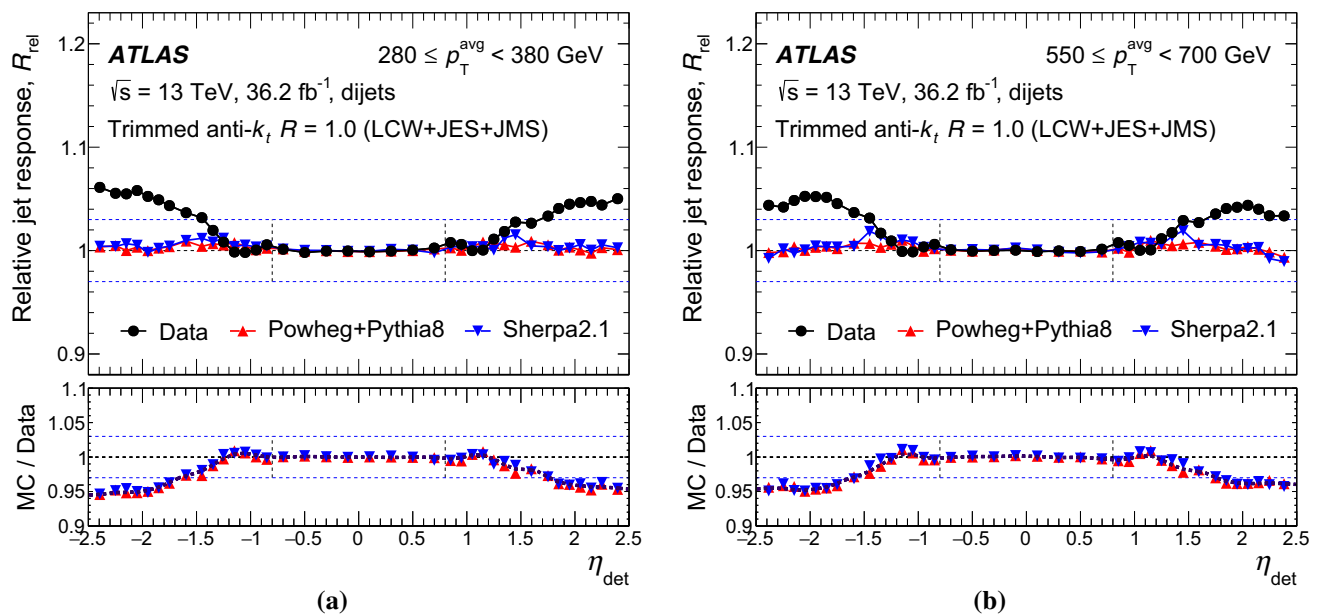

(a)

(b)

Fig. 4 The relative large-R jet response R_{rel} as a function of the large-R jet detector pseudorapidity η_{det} in two representative average transverse momentum p_T^{avg} bins **a** 280 GeV < p_T^{avg} < 380 GeV and **b** 550 GeV < p_T^{avg} < 700 GeV. The average response with in the refer-

ence region $|\eta_{det}| < 0.8$ is unity by construction. In the lower panels, the dotted lines interpolating between POWHEG+PYTHIA markers are obtained by smoothing with a filter using a sliding Gaussian kernel
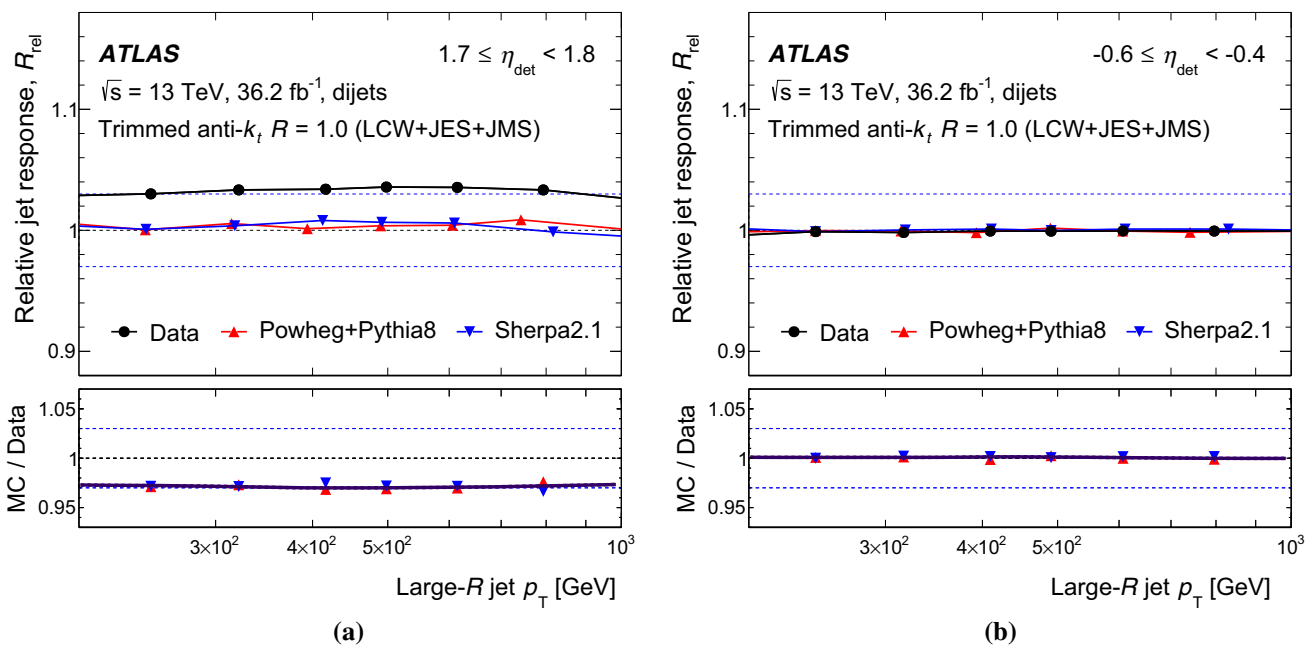
Fig. 5 The relative large-R jet response R_{rel} as a function of the large-R jet p_T in two representative detector pseudorapidity η_{det} bins in the forward and central reference regions **a** $1.7 < \eta_{det} < 1.8$ and **b** $-0.6 < \eta_{det} < -0.4$. In the lower panels, the lines interpolating between POWHEG+PYTHIA markers are obtained by smoothing with a filter using a sliding Gaussian kernel
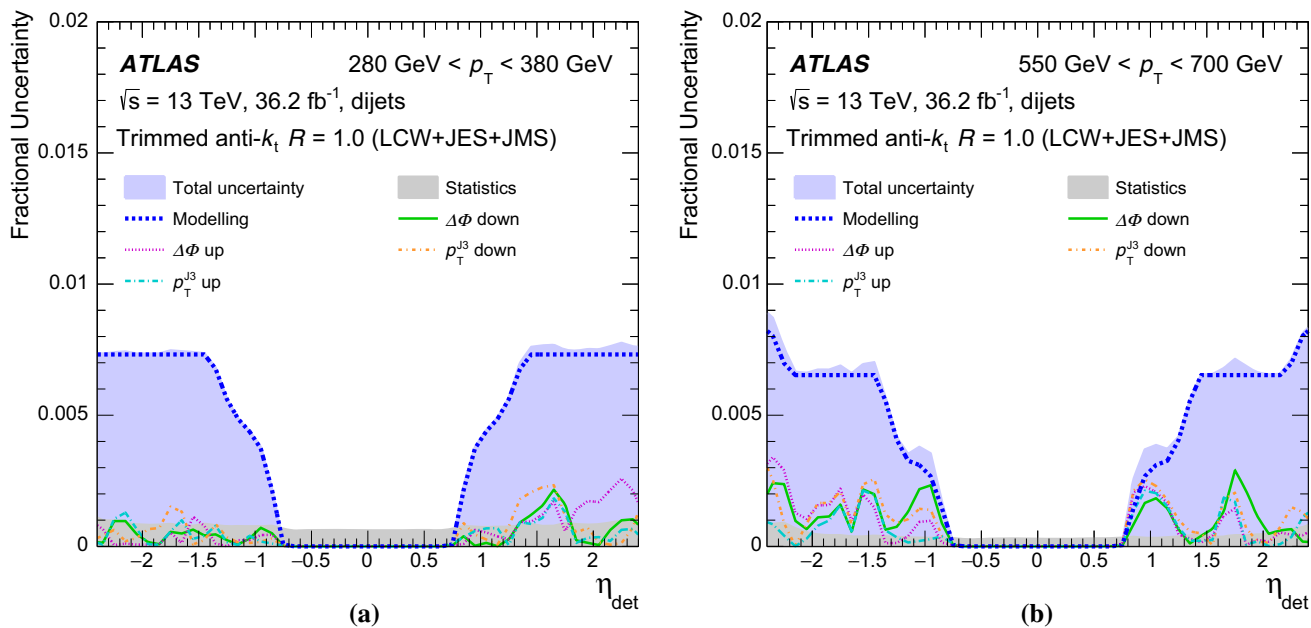

Fig. 6 Uncertainties associated with the large-R jet η-intercalibration as a function of detector pseudorapidity η_{det} in two representative average transverse momentum p_T^{avg} bins **a** 280 GeV $< p_T^{avg} < 380$ GeV and **b** 550 GeV $< p_T^{avg} < 700$ GeV. The uncertainties evaluated using variations of the dijet topology selection are negligible relative to the simulation modelling uncertainty, which typically amounts to a 1% uncertainty for large-R jets within $0.8 < |\eta_{det}| < 2.0$

using a filter with a sliding Gaussian kernel across η_{det} yields a smooth function of jet p_T and η_{det}. The inverse of this smooth function is taken as the η-intercalibration correction factor $c_{rel}(p_T, \eta_{det})$, which is applied as a jet four-momentum scale factor.

The uncertainties associated with the η-intercalibration are shown in Fig. 6 for two representative p_T bins. The uncertainties associated with the veto on additional radiation and the $\Delta\phi$ requirement placed on the dijet topology are derived by varying these selection criteria to the values

listed in Table 1 and re-deriving the calibration. An additional systematic uncertainty accounts for the choice of event generator and parton shower models. The simulation uncertainty is derived by comparing the relative jet-p_T response for two event generators: POWHEG+PYTHIA 8 and SHERPA. In general, the uncertainties associated with the derived calibration are small, amounting to a $\sim 1\%$ uncertainty within the region of interest for large-R jets ($|\eta| < 2.0$). Uncertainties originating from the kinematic requirements made to select events are typically negligible, except in the highest p_T^{avg} bins.

5.2 Z+jet balance

For large-R jets within $|\eta_{\text{det}}| < 0.8$, an in situ calibration is derived by examining the p_T balance of a large-R jet and a leptonically decaying Z boson, either $Z \rightarrow e^+ e^-$ or $Z \rightarrow \mu^+ \mu^-$ (Fig. 2b). Both of these channels provide a precise, independent reference measurement of the jet energy, either from the inner detector and muon spectrometer tracks used to reconstruct muons or from the well-measured electromagnetic showers and inner detector tracks used to reconstruct electrons. The applicable range of this calibration is limited by the kinematic range where Z boson production is relatively abundant, that is, up to a Z boson p_T of about 500 GeV. Electrons used to reconstruct the Z boson are required to pass 'medium likelihood identification' quality and 'Loose' isolation requirements and must be reconstructed within $|\eta| < 2.47$ (excluding the transition region $1.36 < |\eta| < 1.52$ between the barrel and endcap electromagnetic calorimeters) with at least 20 GeV of p_T [56,57]. Similarly, 'VeryLoose' quality and 'Loose' isolation requirements are placed on muons, which must be reconstructed within $|\eta| < 2.4$ with $p_T > 20$ GeV [58]. The lepton pair must have opposite charge and be kinematically consistent with the decay of a Z boson, requiring the invariant mass of the lepton pair to satisfy $66 < m_{\ell^+ \ell^-} < 116$ GeV. Large-R jets studied here are calibrated with the simulation calibration and η-intercalibration described in Sects. 4 and 5.1.

The direct balance method used here closely follows the methodology outlined in Ref. [9]. The average momentum balance between the large-R jet and Z boson is

$$R_{\text{DB}} = \left\langle \frac{p_T^{\text{J}}}{p_T^{\text{ref}}} \right\rangle, \tag{3}$$

where p_T^{J} is the large-R jet p_T and $p_T^{\text{ref}} = p_T^Z \left| \cos{(\Delta\phi)} \right|$ is the component of the reference momentum collinear with the jet, with $\Delta\phi$ being the azimuthal angle between the large-R jet and reference Z boson. The average value is determined using a Gaussian fit.

Even with an ideal detector, the momentum balance R_{DB} of Eq. 3 will only equal unity for an ideal $2 \rightarrow 2$ process. In practice, there tends to be more QCD radiation in the hemisphere opposite to the colour-neutral Z boson, and therefore R_{DB} tends to be below unity. The event selection imposes a veto on the p_T of additional sub-leading jets. A minimum requirement is also imposed on the angular separation $\Delta\phi$ of the large-R jet and reference Z boson. Any mismodelling in the jet energy scale may be evaluated using the balance double ratio of R_{DB} in data and simulation $R_{\text{DB}}^{\text{data}}/R_{\text{DB}}^{\text{MC}}$. If the event selection criteria are met and the reference object is well measured and correctly modelled in simulation, any deviation from unity in the double ratio can be attributed to a mismodelling of the jet response in simulation and may be taken as an in situ correction.

Calibrated anti-k_t $R = 0.4$ jets constructed from electromagnetic-scale topo-clusters are used to veto additional radiation. These jets are required to be $\Delta R > 1.4$ from the large-R jet whose response is being probed (J_1), which ensures that there is no overlap. Such small-R jets with $p_T < 60$ GeV must also satisfy a requirement on the jet vertex tagger (JVT) [54], which is designed to reject additional jets produced by pile-up interactions using information from the inner detector. The $2 \rightarrow 2$ topology selection only accepts events in which any small-R jet is reconstructed with a $p_T < \max(0.1 \, p_T^{\text{ref}}, 15 \text{ GeV})$ and the $\Delta\phi$ between the large-R jet and Z boson is greater than 2.8. A summary of the event selection is presented in Table 2. This table also reports variations associated with each criterion, performed by redoing the full analysis for each such variation and taking the difference between the varied and nominal results as the systematic uncertainty.

Measurements of R_{DB} are carried out separately in the electron and muon channels. They are found to be consistent and thus combined to provide a single measurement of the JES. The average momentum balance in Z+jet events after this combination is shown in Fig. 7. The balance is found to be consistently below unity as a function of p_T^{ref}. The ratio of the predicted balance to the measured balance is consistently 1–4% above unity. The uncertainties associated with this measurement are shown in Fig. 8, where modelling systematic and statistical uncertainties are the dominant source of error over the p_T range considered.

5.3 γ+jet balance

The large-R jet energy scale can be measured using the γ+jet final state (Fig. 2b). This method exploits the fact that the energy of photons is measured more precisely than that of jets. As cross-section for this process is larger than that for Z+jets production, this balance technique probes higher large-R jet p_T. The γ+jet method is based on the balance between photons and large-R jets, using the ratio R_{DB} defined in Eq. (3), where the reference momentum

Table 2 Summary of the 2 → 2 topology selection and systematic variations considered for the Z+jet direct balance analysis. The labels J_i refer to the ith leading large-R jet, and j_i to the ith leading small-R jet that fulfils $\Delta R(J_1, j_i) > 1.4$

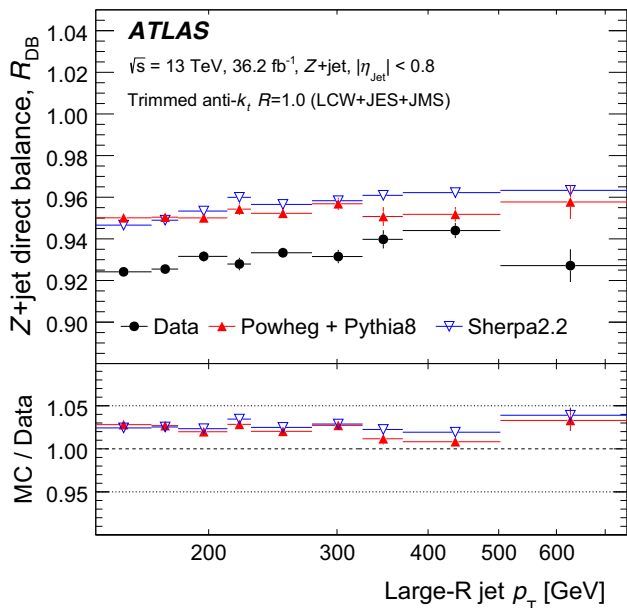| Variable	Nominal selection	Up variation	Down variation
$p_T^{j_1}$	$\max(0.1\, p_T^{ref}, 15\,\text{GeV})$	$\max(0.15\, p_T^{ref}, 20\,\text{GeV})$	$\max(0.05\, p_T^{ref}, 10\,\text{GeV})$
$\Delta\phi(Z, J_1)$	> 2.8	> 2.9	> 2.7
Small-R jet JVT	> 0.59	> 0.91	> 0.11

Fig. 7 The momentum balance R_{DB} as a function of the large-R jet transverse momentum p_T in Z+jet events for the combined e^+e^- and $\mu^+\mu^-$ channels. Only statistical uncertainties are shown. For each p_T^{ref} bin, the measured R_{DB} is plotted against the average jet p_T of the bin. The horizontal error bars give an indication of the width of the associated p_T^{ref} bin

Fig. 8 Breakdown of the uncertainties in the JES measurement with the Z+jet direct balance method as a function of the large-R jet transverse momentum p_T. The sources include the statistical uncertainty, variations of the generator (simulation modelling), variations of the event selection (pile-up (JVT), sub-leading jet veto, $\Delta\phi$), the uncertainties in the energy scale and resolution of electrons (e E-scale and e E-resolution) and muons (μ E-scale and μ E-resolution), and the uncertainty in the pile-up conditions (N_{PV} shift). These uncertainties are also discussed in the context of small-R jets in Ref. [9]. The lines are obtained by smoothing a binned representation of these uncertainties using a sliding Gaussian kernel

$p_T^{ref} = p_T^{\gamma} \left| \cos(\Delta\phi) \right|$ is the component of p_T^{γ} collinear with the jet.

The double ratio of $R_{DB}^{data}/R_{DB}^{MC}$ measures any residual modelling effects in the jet energy scale calibration. If the reference photon is well measured experimentally and the γ+jet events are correctly modelled in simulation, any deviation from unity in the double ratio can be attributed to a mismodelling of the jet response in the Monte Carlo simulation.

Events are selected using the lowest unprescaled single-photon trigger. The offline selection requires the presence of a photon satisfying the 'tight' identification and isolation requirements [59,60] with at least 140 GeV of E_T. This criterion ensures full trigger efficiency. As in the case of Z+jet balance (Sect. 5.2), the presence of significant additional radiation in the event invalidates the assumption of a balanced topology. Events are therefore vetoed if a reconstructed, calibrated $R = 0.4$ jet built from electromagnetic-scale topo-clusters has a p_T which
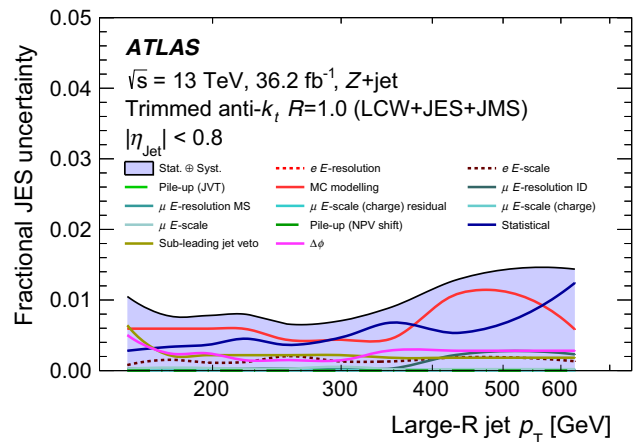
satisfies $p_T > \max(0.1\, p_T^{ref}, 15\,\text{GeV})$. Small-$R$ jets with $p_T < 60$ GeV must also satisfy a JVT requirement. Photons must be separated from reconstructed large-R jets by at least $\Delta\phi(J, \gamma) > 2.8$. The simulation calibration and η-intercalibration described in Sects. 4 and 5.1 are applied to the large-R jets studied here.

A photon purity correction is applied to the mean balance results in data to correct for contamination from misidentified jets or electrons that may skew the nominal p_T balance. The contamination of the photon sample by fakes is derived from data using the double-sideband, or ABCD, method [61,62] in the plane spanned by the photon isolation[2] and the photon

---

[2] The calorimeter isolation variable E_T^{iso} is defined as the sum of the E_T of topological clusters deposited in a cone of size $\Delta R = 0.4$ around the photon candidate, excluding an area of size $\Delta\eta \times \Delta\phi = 0.125 \times 0.175$ centred on the photon cluster and subtracting the expected photon energy deposit outside of the excluded area. Fluctuations in the ambient transverse energy of the event are corrected for; the typical size of this correction is 2 GeV in the central region.
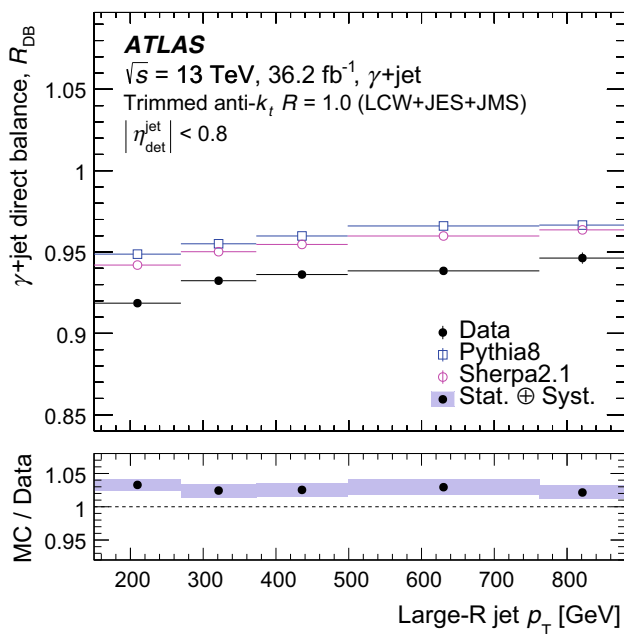
Fig. 9 The momentum balance R_{DB} extracted from γ+jet events in data and simulations as a function of the transverse momentum p_T of the large-R jet. The ratio of the results obtained from the nominal PYTHIA simulation and from data is shown in the bottom panel. The ratio of PYTHIA to SHERPA results, taken as a systematic uncertainty associated with modelling, is included in the shaded band in the ratio panel, which also includes statistical and systematic uncertainties from other sources. For each p_T^{ref} bin, the measured R_{DB} is plotted against the average jet p_T of the bin. The horizontal error bars give an indication of the width of the associated p_T^{ref} bin

Fig. 10 The momentum balance R_{DB} extracted from γ+jet balance distributions in data and simulation as a function of the large-R jet detector pseudorapidity η_{det}. The ratio of the results obtained from the nominal PYTHIA simulation to the results from data is shown in the bottom panel. The ratio of PYTHIA to SHERPA results, taken as a systematic uncertainty associated with modelling, is included in the shaded band in the ratio panel, which also includes statistical and systematic uncertainties from other sources

identification measure.[3] The purity correction results in a shift of the relative R_{DB} value between data and simulation of about 2%.

In Fig. 9 the result is shown as a function of the reference p_T for large-R jets in the region $|\eta| < 0.8$. The ratio of the predicted response in the simulation to the measured response is shown in the inset below the main panel. As already observed in Sect. 5.2, the ratio of simulation to data is above unity over the whole p_T range. These results are included in the in situ calibration that corrects the jet energy response in data.

The uniformity of the large-R jet response across the detector geometry is shown in Fig. 10, as a validation of the η-intercalibration procedure (Sect. 5.1). The relative response across the detector is constant and well behaved.

There are three main categories of systematic uncertainties in the R_{DB} measurement: those related to the modelling of additional QCD radiation which affects the balance, uncertainties associated with the photons [63,64], and effects due

to the presence of pile-up jets. The effects of extra radiation on the balance are assessed by varying the topological selections and the overlap removal as described in Table 3. Repeating the analysis separately using $\Delta\phi(J, j) > 1.2$ and $\Delta\phi(J, j) > 1.6$ produces a negligible systematic shift relative to the nominal result. The effects of the photon measurement are assessed by varying the energy scale and resolution of the photon calibration, as well as by varying the measured photon purity in the purity correction. The effects of pile-up jets on the calibration are estimated by varying the JVT selection threshold for the small-R jets. Lastly, the analysis is repeated with SHERPA 2.1 MC samples, in place of the nominal PYTHIA 8 samples, to assess the modelling uncertainty. As shown in Fig. 11, the overall combined systematic and statistical uncertainty is approximately 1% for the p_T range from 150 to 880 GeV. The photon energy scale uncertainty is the dominant source over the entire p_T range.

5.4 Multijet balance

The Z+jet and γ+jet techniques provide precise constraints on the jet energy scale for jets with p_T up to 1 TeV. The energy scale of higher-p_T large-R jets is measured using multijet events. A schematic representation of the event topology used in this method is shown in Fig. 2c. The multijet balance

---

[3] The photon identification decision is based on a set of shower shape variables computed from energy depositions in the first and second layers of the electromagnetic calorimeter and from leakage in the hadronic calorimeter.
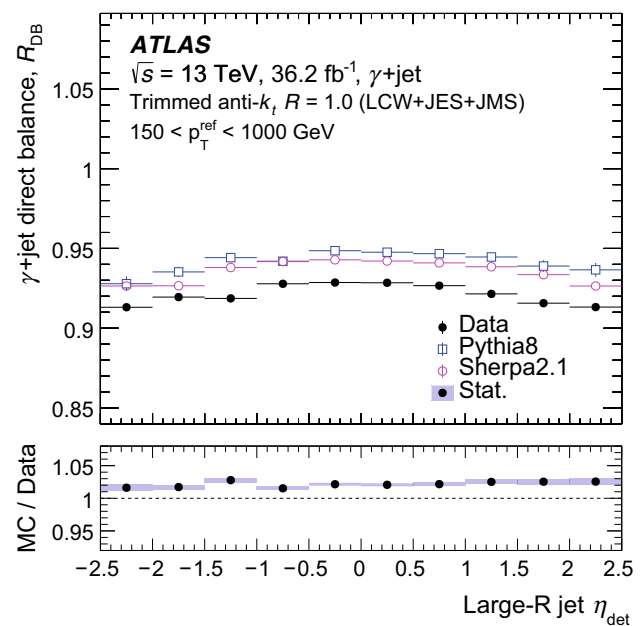
Table 3 Summary of the selection and systematic variations considered for the γ+jet direct balance analysis. The labels J_1 refers to the leading large-R jet and j_1 to the leading small-R jet that fulfils $\Delta R(J_1, j) > 1.4$

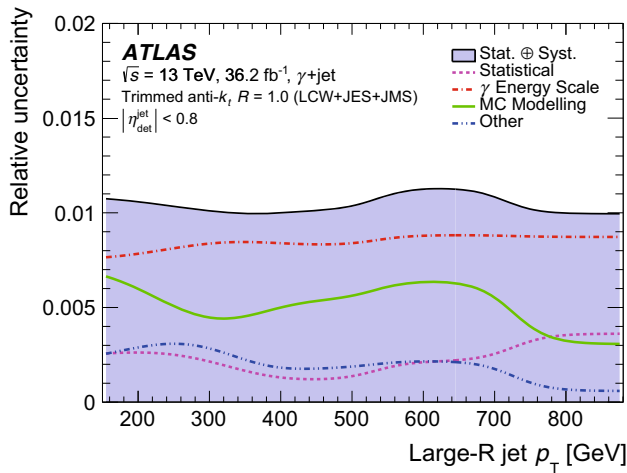| Variable	Nominal selection	Up variation	Down variation
$p_T^{j_1}$	$\max(0.1\, p_T^{\text{ref}}, 15\text{ GeV})$	$\max(0.15\, p_T^{\text{ref}}, 20\text{ GeV})$	$\max(0.05\, p_T^{\text{ref}}, 10\text{ GeV})$
$\Delta\phi(J_1, \gamma)$	> 2.8	> 2.9	> 2.7
Small-R jet JVT	> 0.59	> 0.91	> 0.11

Fig. 11 Systematic uncertainties in the in situ measurement of the jet energy scale obtained with the γ+jet method as a function of the large-R jet transverse momentum p_T. The lines shown are obtained by smoothing a binned representation of these uncertainties using a sliding Gaussian kernel

(MJB) method takes advantage of events where an energetic large-R jet is balanced against a system that consists of multiple lower-p_T jets.

For the calibration of large-R jets the reference p_T^{recoil} is obtained as the four-vector sum of calibrated small-R anti-k_t jets. The transverse momentum balance is

$$R_{\text{MJB}} = \left\langle \frac{p_T^J}{p_T^{\text{recoil}}} \right\rangle,$$

where p_T^J is the transverse momentum of the leading large-R jet and p_T^{recoil} is the magnitude of the vectorial sum of the transverse momenta of the recoil system of small-R jets. The average value of the ratio is taken to be the mean value of a Gaussian fit. The value of R_{MJB} is measured in data and

determined in simulation in several bins of p_T^{recoil}. The data-to-simulation double ratio $R_{\text{MJB}}^{\text{data}}/R_{\text{MJB}}^{\text{MC}}$ allows estimation of the response for high-p_T jets.

Events are selected using single small-R jet triggers. Bins of p_T^{recoil} are defined to correspond to a given fully efficient single small-R jet trigger. The triggers used for 200 GeV < p_T^{recoil} < 550 GeV are prescaled, whereas an unprescaled jet trigger is used for p_T^{recoil} > 550 GeV.

The event selection is summarized in Table 4. For small-R jets with $p_T < 60$ GeV within $|\eta| < 2.4$, the JVT selection is applied to suppress pile-up jets. The large-R probe jet is required to have $|\eta_{\text{det}}| < 0.8$, while the small-$R$ jets that constitute the recoil system are required to have $|\eta_{\text{det}}| < 2.8$ and $p_T > 25$ GeV. To select events with multijet recoil systems, the leading jet in the recoil system (j_1) is allowed to have no more than 80% of the total transverse momentum of the recoil system. This selection ensures that the recoil system consists of several jets with lower p_T than the large-R jet, which are each well-calibrated by small-R jet in situ techniques [9]. The angle α in the azimuthal plane between the leading large-R jet and the vector defining the recoil system is required to satisfy $|\alpha - \pi| < 0.3$. The ΔR distance β between the leading large-R jet and the nearest small-R jet from the recoil system is required to be greater than 1.5. The simulation calibration and η-intercalibration described in Sects. 4 and 5.1 are applied to the large-R jets studied using this technique.

Figure 12 shows the distribution of R_{MJB} as a function of the large-R jet p_T. The balance in data decreases from approximately 1.01 at $p_T = 300$ GeV to about 0.99 for jets with $p_T = 2$ TeV. The simulation shows a similar downward trend. The response in simulations is 2% higher than in data, consistent with the findings of the other methods where they overlap.

Table 4 Summary of the event selection and systematic variations considered for the multijet direct balance analysis. The label j_i refers to the ith leading small-R jet

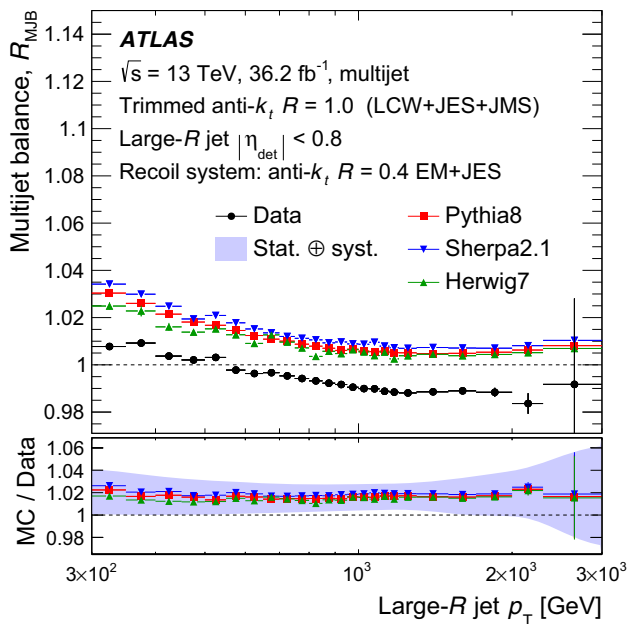| Variable	Nominal selection	Up variation	Down variation
Separation angle (α)	$|\alpha - \pi| < 0.3$	$|\alpha - \pi| < 0.4$	$|\alpha - \pi| < 0.2$
ΔR separation (β)	>1.5	>1.9	>1.1
$p_T^{j_1}/p_T^{\text{recoil}}$	< 0.8	< 0.9	< 0.7
Recoil system minimum p_T	25 GeV	30 GeV	20 GeV

Fig. 12 Mean transverse momentum balance R_{MJB} for leading-p_T large-R jets ($|\eta| < 0.8$) balanced against a system of at least two small-R jets ($p_T \geq 25$ GeV, $|\eta| < 2.8$) as a function of the large-R jet transverse momentum p_T. The measured balance is compared with the prediction of Monte Carlo simulations based on the event generators PYTHIA 8, SHERPA 2.1, and HERWIG 7. Below, the ratio of response measurements in data and simulation is presented. The shaded band indicates the total uncertainty of the measurement, described in detail in the text. For each p_T^{ref} bin, the measured R_{DB} is plotted against the average jet p_T of the bin. The horizontal error bars gives an indication of the width of the associated p_T^{ref} bin

Fig. 13 The fractional uncertainty in R_{MJB} as a function of the large-R jet transverse momentum p_T. The lines shown are obtained by smoothing a binned representation of these uncertainties using a sliding Gaussian kernel

The total uncertainty in the R_{MJB} measurement is approximately $\pm 2\%$ or lower for $p_T < 2$ TeV. The uncertainty in the energy scale of the jets of the recoil in situ procedure is propagated through the large-R MJB procedure. Uncertainties associated with high-p_T jets in the recoil system which lie beyond the region covered by the $R = 0.4$ in situ analyses are derived from measurements of the calorimeter response to isolated single charged particles, which are also propagated through this large-R jet analysis to provide coverage at the highest values of jet p_T (> 1 TeV) [65]. No assumption is made about the flavour of the recoil jets (originating from a gluon, a light quark, or a heavy-flavour quark). This lack of knowledge is a source of systematic uncertainty. The uncertainty in the multijet-balance observable due to the jet flavour response is evaluated using a correlated propagation of the small-R jet flavour response uncertainties, i.e. all jets are shifted simultaneously.

In addition to the jet calibration and uncertainties in the reference scale, the event selection criteria and the modelling in the event generators directly affect the p_T balance used to obtain the multijet-balance results. The impact of the event selection criteria is investigated by shifting each event selection criterion up and down by a specified amount and observ-
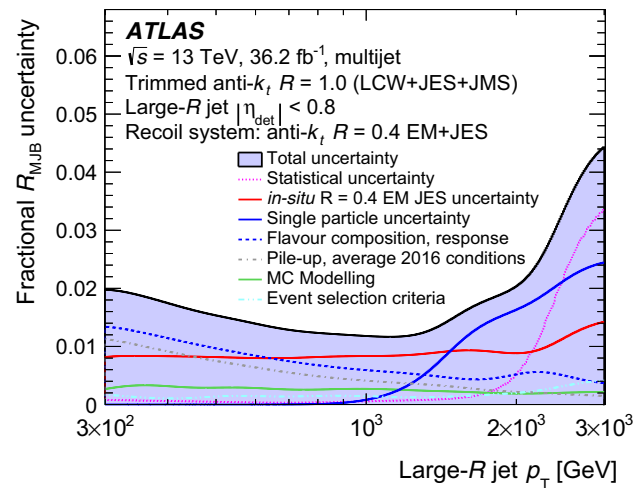
ing the change in the multijet-balance variable. Using an approach to systematic uncertainties similar to that in the small-R in situ analysis, the transverse momentum threshold for recoil jets is shifted by ± 5 GeV, the p_T^{j1}/p_T^{recoil} is shifted by ± 0.1, the angle α is shifted by ± 0.1, and β is shifted by ± 0.4. The uncertainty due to modelling of multijet events in simulations is estimated from the largest difference between the multijet-balance results obtained from the nominal PYTHIA 8 simulation and those obtained from SHERPA v2.1 and HERWIG 7. Figure 13 shows the breakdown of the fractional uncertainties in the jet energy scale derived from this method. Various uncertainties propagated from the reference jet system dominate the measurement across the entire p_T range.

6 In situ jet mass calibration

In this section, two methods to derive an in situ calibration for the large-R jet mass are presented. The first method, known as the R_{trk} method, relies on the tracker to provide an independent measurement of the jet mass scale and its associated uncertainty. The second method, known as forward folding, fits the mass peaks and jet mass response of the W boson and top quark to measure the relative energy and mass scales and resolutions between data and simulations. Both measurements are performed after applying the in situ calibration for the energy scale, which also affects the jet mass scale. The results in this section are combined into a global jet mass calibration, detailed in Sect. 8.

6.1 Calorimeter-to-tracker response ratios

The calorimeter-to-tracker response double-ratio method (or R_{trk} method) is built around the fact that the ATLAS detector provides two independent measurements of the properties of the same jet from the calorimeter and the tracker [3]. Jets formed from inner detector tracks only take into account the hits from their charged-particle constituents. Calibrated jets formed from energy depositions within the calorimeter provide a measure of the properties from the full shower. The average calorimeter-to-track jet response

$$R_{trk} = \left\langle \frac{p_T^{calo}}{p_T^{track}} \right\rangle$$

is proportional to the average calorimeter-to-truth jet response. Therefore, a comparison of the double ratio of R_{trk} in simulations and data provides a way to validate the modelling of large-R jet properties in situ. The ratio of R_{trk} values determined in data and simulations should be equal to unity for well-modelled observables. Any deviation from this expectation can be taken as a scale uncertainty in the measurement. This method is versatile and allows the determination of uncertainties for several variables, such as the p_T, mass, and substructure information of large-R jets. Moreover, the dijets process provides a very large sample, such that the analysis can be performed in a large number of p_T and mass or m/p_T regions.

Figure 14 shows R_{trk} as a function of the large-R jet p_T in dijet events for data and several simulation samples. The maximum spread between the two generators and three tracking variations that assume three different types of mismodelling (resolution [66], efficiency within dense environments [67], and alignment [68]) is about 8%. A steady increase in the calorimeter-to-track jet response R_{trk} with increasing large-R jet p_T is observed, going well beyond the expected ratio of the total and charged transverse momenta of a jet, caused by inefficiencies in the tracker response at high jet p_T.

Figure 15 shows a breakdown of the uncertainties in the large-R jet p_T derived from this method for the transverse momentum for large-R jets with values of $m/p_T \approx 0.2$. The main source of uncertainty across the entire p_T range originates from differences between data and the nominal Monte Carlo generator considered in this study. As this uncertainty was expected to be large, the R_{trk} method is neither included in the in situ JES combination nor used as a source of systematic uncertainty for the JES of large-R jets. Rather, the R_{trk} p_T results are used as an independent cross-check to validate the JES calibration techniques.
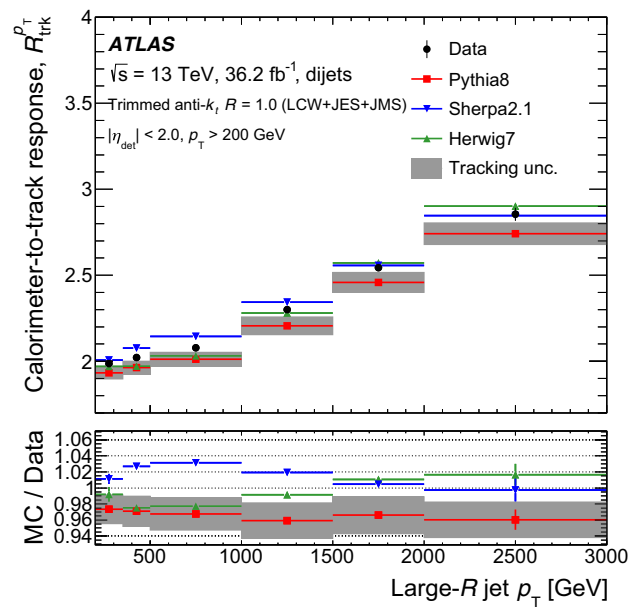

Fig. 14 Measurement of $R_{trk}^{p_T}$ as a function of the large-R jet transverse momentum p_T for large-R jets with $m/p_T = 0.2$. The large-R jet p_T is corrected using the simulation calibration, η-intercalibration, and a combination of in situ direct balance techniques. Data are compared with three generators and with three tracking variations for the default generator PYTHIA 8 (shown as a band around these points). The double ratio of $R_{trk}^{p_T}$ measured in simulations and data is shown in the lower panel

Fig. 15 The total uncertainty in the relative jet energy scale in data and simulations associated with the R_{trk} method is plotted as a function of jet transverse momentum p_T. The large-R jet p_T is corrected using the simulation calibration, η-intercalibration, and a combination of in situ direct balance techniques. The contributions from several sources are indicated. The baseline uncertainty represents the deviation of the double ratio from unity for the baseline simulations. The lines shown are obtained by smoothing a binned representation of these uncertainties using a sliding Gaussian kernel

Fig. 16 Measurement of R_{trk}^m as a function of the large-R jet transverse momentum p_T for large-R jets with $m/p_T = 0.2$. The large-R jet p_T is corrected using the simulation calibration, η-intercalibration, and a combination of in situ direct balance techniques. Data are compared with three generators and with three tracking variations for the default generator PYTHIA 8 (shown as a band around these points). The double ratio of R_{trk}^m measured in simulations and data is shown in the lower panel
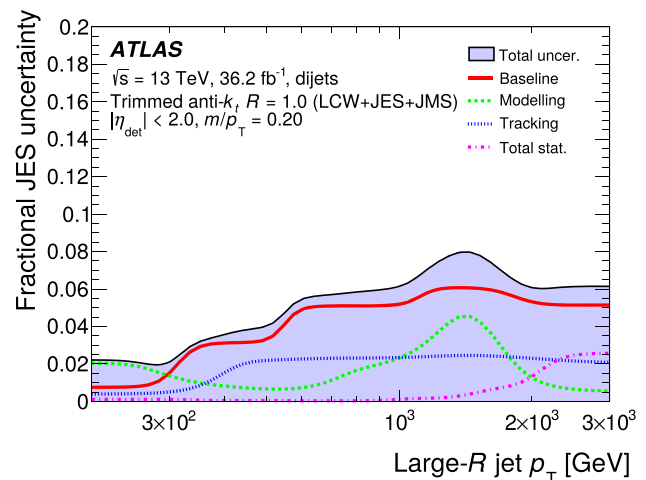

Fig. 17 The total uncertainty in the relative jet mass scale between data and simulation associated with the R_{trk} method is plotted as a function of jet transverse momentum p_T for large-R jets with $m/p_T = 0.2$. The large-R jet p_T is corrected using the simulation calibration, η-intercalibration, and a combination of in situ direct balance techniques. The contributions from several sources are indicated. The baseline uncertainty represents the deviation of the double ratio from unity for the baseline simulations. The lines shown are obtained by smoothing a binned representation of these uncertainties using a sliding Gaussian kernel
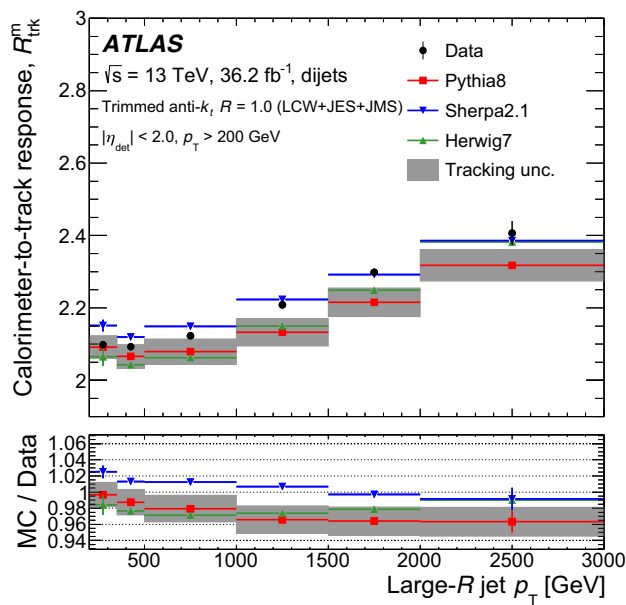
The same method is also applied to the large-R jet calorimeter mass, and is shown in Fig. 16. The largest difference between the considered generators is ~ 2 to 3%. Figure 17 shows the various uncertainties in the large-R jet mass derived from the R_{trk} mass response for large-R jets with $m/p_T = 0.2$. Again, the main source of uncertainty originates from differences between data and the nominal simulation.

The R_{trk} method can also be used to study the topology dependence of the response modelling. The double ratio is constructed in two event samples, with different jet flavours (jets originating from light quarks or gluons and jets containing a hadronic top quark decay). The dijet sample used for Fig. 14 is dominated by gluon jets at low transverse momenta, while at higher momenta the fraction of light-quark jets in the sample increases. The $t\bar{t}$ sample of Sect. 6.2 is enriched in large-R jets that contain a complete high-p_T object's decay (either a top quark or W boson). In Fig. 18 the double ratios of the two samples are compared for jet p_T and jet mass. The jets in the samples correspond to the same pseudorapidity range $|\eta| < 2.0$ and the same p_T and jet mass intervals. In both samples, the double ratio is constructed with the nominal simulation events, which rely on PYTHIA 8 for hadronization. As systematic uncertainties are expected to partially cancel out, only statistical uncertainties are shown.
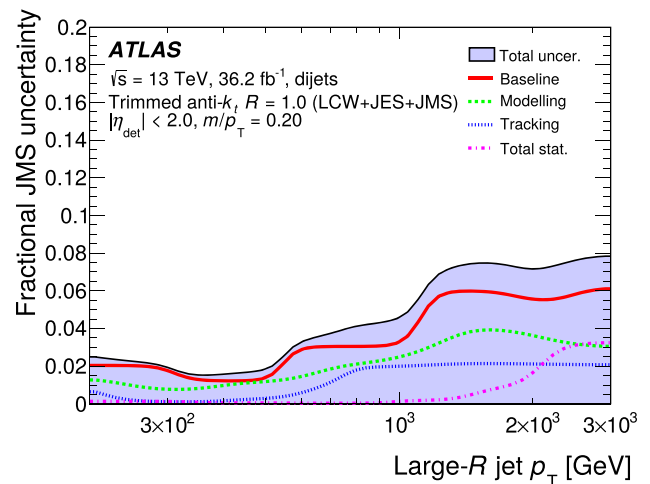
There is a mild tension between the double-ratio results from the two samples. The double ratio in the $t\bar{t}$ sample is systematically somewhat higher than the equivalent result in the dijet sample. The difference is typically 1% or less, except in the first bin of the double ratio for jet mass. This is significant compared to the statistical uncertainties but is small in comparison with the modelling uncertainties of the R_{trk} method. Some properties of these two jet populations differ, such as the distribution of their m/p_T and their flavour composition, and so it is not expected that the modelling uncertainties will cancel out exactly. No additional uncertainty is assigned to account for the topology dependence.

6.2 Forward folding

A high-purity signal sample of large-R jets with high-p_T, hadronically decaying W bosons and top quarks is obtained by selecting $t\bar{t}$ events in the lepton+jets final state, where a hadronically decaying top quark balances one which decays to a leptonically decaying W boson and b-quark. This sample is used to measure the response for jets in signal-like topologies which contain jets consisting of multiple regions of high energy density [69,70]. The jet mass response is determined by fits to the W boson and top quark mass peaks in the large-R jet invariant mass distribution of the hadronically decaying top quark candidate.

The event selection is based on the ATLAS search for $t\bar{t}$ resonances [71] and is summarized in Table 5. It requires a
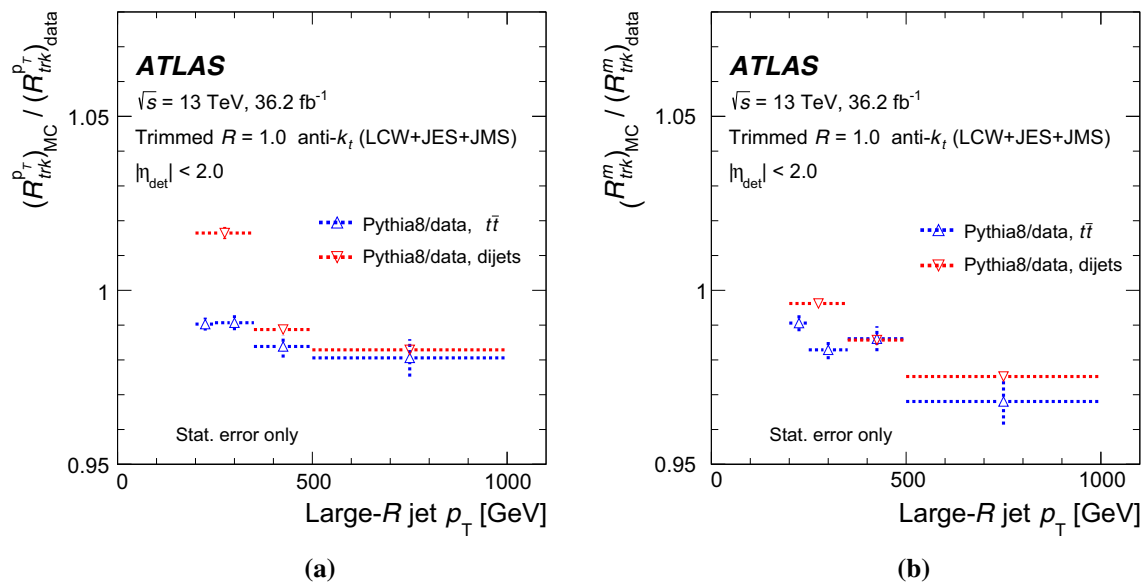
(a)   **(b)**

Fig. 18 The simulation/data ratio of R_{trk} for **a** large-R jet p_T and **b** calorimeter mass as a function of the large-R jet transverse momentum p_T. Two sets of results are derived from a dijet sample, dominated by light-quark and gluon jets, and a $t\bar{t}$ sample, where the large-R jets contain a boosted W boson or top quark. The large-R jet p_T is corrected using the simulation calibration, η-intercalibration, and a combination of in situ direct balance techniques. The jets in both samples correspond to the same pseudorapidity range $|\eta| < 2.0$ and the same p_T and jet mass intervals. The double ratio is constructed with the nominal PYTHIA 8 samples for dijet events and POWHEG +PYTHIA 8 samples for the $t\bar{t}$ sample. The error bars indicate statistical uncertainties

Table 5 Summary of the event selection for the top quark events decaying into lepton+jets, to be used for top and W mass calibration. The p_T bins into which events are divided are also shown

Object	Selection	Description
Muon (μ)	Single-muon triggers	Trigger
	$p_T^{\mu} > 25$ GeV, $|\eta| < 2.5$	Preselection
	`tight` muon ID	Identification
	$\Delta R_{\mu,\text{jet}} > 0.4$	Isolation
E_T^{miss}	$E_T^{\text{miss}} > 20$ GeV, $m_T > 60$ GeV	
Small-R Jets j	$p_T > 25$ GeV	Jet selection
	At least one jet with $\Delta R(j, \mu) < 1.5$	Boosted top decay
	At least one b-tagged jet	Flavour tagging
Large-R Jets	$\Delta R_{\text{j,J}} > 2$	Opposite hemispheres
$p_T \in [200, 250]$ GeV, $[250, 350]$ GeV	$\Delta R_{b,\text{J}} > 1$	Boosted W sample
	$\Delta R_{b,\text{J}} > 1$	b-jet veto
$p_T \in [350, 500]$ GeV, $[500, 1000]$ GeV	$\Delta R_{b,\text{J}} < 1$	Boosted top
	$\Delta R_{b,\text{J}} < 1$	b-jet matched

central high-p_T, isolated muon, and significant missing transverse momentum (E_T^{miss}) [72]. The W boson transverse mass obtained from $m_T^2 = 2p_T^{\text{lep}} E_T^{\text{miss}}(1 - \cos(\Delta\phi))$, where $\Delta\phi$ is the azimuthal angle between the charged lepton and the direction of the missing transverse momentum, must be greater than 60 GeV. A multivariate b-tagging algorithm is used to identify $R = 0.4$ jets which originate from the decays of b-quarks based on information about the impact parameters of inner detector tracks matched to the jet, the presence of displaced secondary vertices, and the reconstructed flight paths of b- and c-hadrons inside the jet; the 70% signal tagging efficiency working point is used here [73].

The large-R jet mass distribution of the highest-p_T large-R jet in the hemisphere opposite to the charged lepton is shown in Fig. 19 for two categories of events, and for both the calorimeter-only and track-assisted jet masses. For large-R jets with intermediate p_T (200 GeV $< p_T <$ 350 GeV), in Fig. 19a, c, the decay products of the hadronic W boson are captured in a single large-R jet. For high-p_T jets with $p_T >$ 350 GeV, in Fig. 19b, d, the complete hadronic top decay is
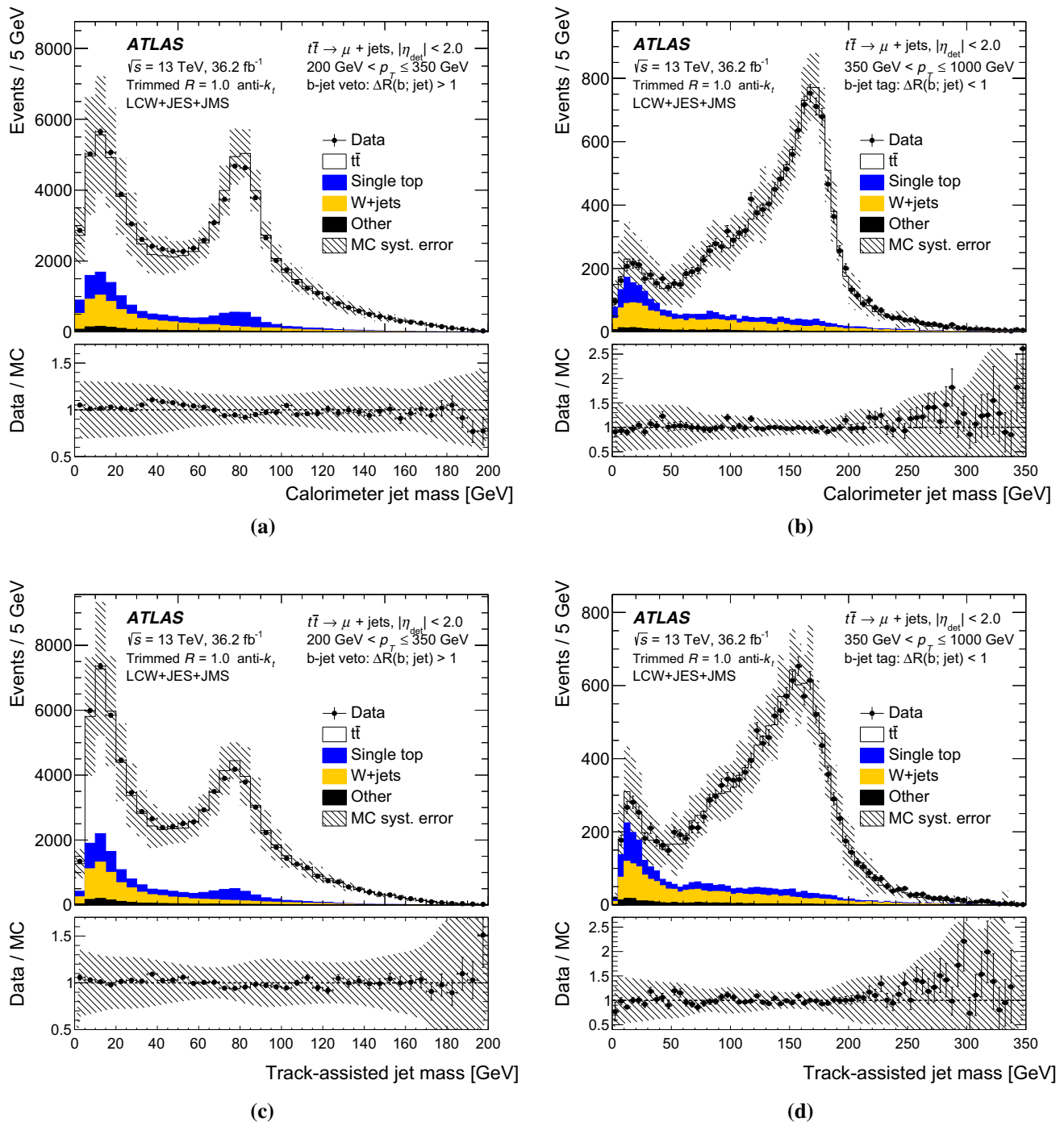
(a)

(b)

(c)

(d)

Fig. 19 The distributions of the jet invariant mass for large-R jets in samples enriched in **a**, **c** boosted W bosons and **b**, **d** boosted top quarks. The distribution of the calorimeter mass is shown in (**a**) and (**b**), and the distribution of the track-assisted mass of the same jets is shown in (**c**) and (**d**). The large-R jet transverse momentum p_T is corrected using the simulation calibration, η-intercalibration, and a combination of in situ direct balance techniques. The template estimated from simulations is rescaled to match the observed yield. The lower panels display the data-to-simulation ratio. The error bars on the data represent the statistical uncertainty. The dashed uncertainty band on the simulation template includes the systematic uncertainties due to signal and detector modelling

captured in the main large-R jet. The high-p_T W boson and top quark topologies are confirmed by, respectively, vetoing or requiring a b-tagged small-R jet that overlaps with the large-R jet.

The track-assisted mass (Eq. (1)) is obtained by scaling the invariant mass of the charged-particle jet by the ratio of the p_T of the calorimeter and charged-particle jets. The resulting jet mass distributions in the W boson and top quark large-R

jet samples are presented in Fig. 19c, d. The selection for this second set of plots is entirely based on the properties of the matched calorimeter jet, such that plots (a) and (c) and plots (b) and (d) are populated by the same jets. The track-assisted mass peaks in (c) and (d) are slightly broader than the calorimeter-based mass peaks in (a) and (b) for large-R jets with a large invariant mass and relatively low p_T.

The position and shape of the mass peaks provide information about the large-R jet mass scale and resolution. Values for the ratio of the response in data and simulations ($s = R^m_{data}/R^m_{MC}$) and the ratio of the resolution in data and simulations ($r = \sigma^m_{data}/\sigma^m_{MC}$) are extracted from the jet mass spectrum. These two parameters are extracted simultaneously in a fit referred to as forward folding [10]. This method produces simulation-based predictions of the jet mass spectrum with variable response and resolution. This is achieved by folding particle-level jets with a response function. The default response function is taken from the nominal simulations. The predicted detector-level jet mass spectrum for arbitrary values of s and r is obtained by modifying the response function by

$$m^{fold} = s\, m^{reco} + \left(m^{reco} - m^{truth}\, R_m\left(m^{truth}, p_T^{truth}\right)\right)\,(r - s),$$

where m^{reco} is the detector-level large-R jet mass and R_m is the large-R jet mass response. The value of R_m is obtained from simulations, as discussed in Sect. 4. Typical values of R_m are in the range 0.8–1.5, depending on jet p_T and mass. The forward-folding procedure does not require the response to be Gaussian. The scale factors s and r also modify the non-Gaussian tails of the response function, if these are present in the simulations.

The prediction from simulation is fit to the data by minimizing the χ^2 built with the predicted and observed distributions. The best-fit values for s and r are taken as the data-to-simulation scale factors for the large-R jet mass response and jet mass resolution. This method has the advantage that the response for the $t\bar{t}$ events and events from other Standard Model processes is varied consistently. It was first applied to 2012 data [10]. Further details of the forward-folding procedure are in Refs. [43,74].

The results of the fits are shown in Fig. 20. The data sample is divided in several p_T bins. The W boson peak is fitted in two intervals: 200 GeV $< p_T <$ 250 GeV and 250 GeV $< p_T <$ 350 GeV. The top quark peak is fitted for p_T between 350 and 500 GeV and between 500 GeV and 1 TeV. The small error bars on the points represent the statistical uncertainty, and the larger error bars represent the total uncertainty. The dominant systematic effect is expected to be due to the modelling of top quark pair production, estimated by repeating the analysis with POWHEG + HERWIG 7, SHERPA, and several variations of the generator settings that regulate the probability of hard initial- and final-state radiation.
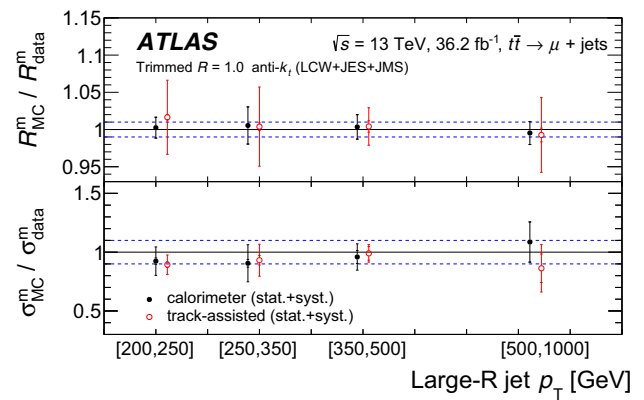

Fig. 20 Summary of the in situ measurements of the large-R jet mass response in $t\bar{t}$ events with a lepton+jets final state as a function of the large-R jet transverse momentum p_T. The large-R jet p_T is corrected using the simulation calibration, η-intercalibration, and a combination of in situ direct balance techniques. The closed circles correspond to the JMS and JMR of trimmed large-R jets reconstructed from calorimeter clusters. The open circles represent the equivalent result for the track-assisted mass. The dashed lines, corresponding to $\pm1\%$ for the JMS and $\pm10\%$ for the JMR, are drawn for reference. The results in the first two p_T bins (200 GeV $< p_T <$ 250 GeV and 250 GeV $< p_T <$ 350 GeV) correspond to a sample of high-p_T W bosons, and the highest two bins (350 GeV $< p_T <$ 500 GeV and 0.5 TeV $< p_T <$ 1 TeV) correspond to high-p_T top quarks. In each subsample, the JMS and JMR are extracted simultaneously in a two-parameter fit to the mass distribution. The statistical and total uncertainties are indicated with the small and large error bars on the data points, respectively

An in situ calibration is also derived for the track-assisted mass in a completely analogous fashion. The JMS and JMR results are shown with open circles in Fig. 20. The statistical and systematic uncertainties are indicated on the data points. The systematic uncertainties are dominated by modelling uncertainties and are expected to be strongly correlated between the two measurements. The in situ scales of the two mass measurements are found to be within 1% for all points and within 0.5% for three out of four. As the track-assisted mass is primarily sensitive to the p_T response of the calorimeter, this level of agreement implies that the p_T and mass scales are closely connected for these high-mass jets with relatively low p_T.

Measurements of the p_T response of high-p_T W bosons or top quarks can be obtained directly by fitting the balance distribution of the two top quark candidates. This provides a cross-check of the direct balance methods discussed previously in Sects. 5.1–5.4 in a topology with a very different radiation pattern. The reference system is formed by the b-jet, the charged lepton, and the neutrino from the semileptonic top quark decay. It is reconstructed by adding the four-vectors of the charged lepton, the leading (and possibly b-tagged) small-R jet in a cone of size $\Delta R = 1.5$ around the charged lepton, and the neutrino [75]. The transverse momentum of the neutrino is inferred by assigning the E_T^{miss} to the neu-
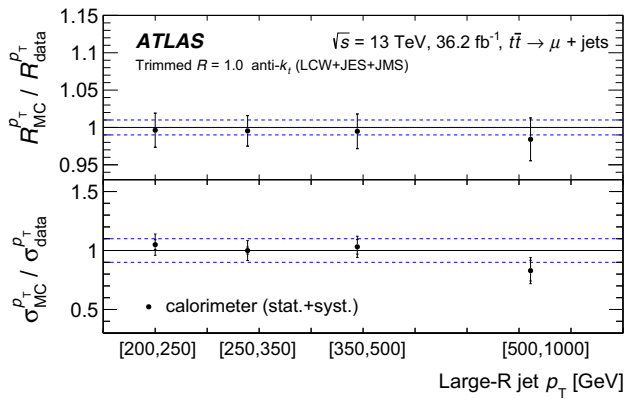
Fig. 21 Summary of the in situ measurements of the large-R jet response in $t\bar{t}$ events with a lepton+jets final state as a function of the large-R jet transverse momentum p_T. The closed circles correspond to the JES and JER of trimmed large-R jets reconstructed from calorimeter clusters. The large-R jet p_T is corrected using the simulation calibration, η-intercalibration, and a combination of in situ direct balance techniques. The error bars represent the total uncertainty. Statistical uncertainties are indicated with the inner error bar (only visible on some of the points). The dashed lines, corresponding to $\pm 1\%$ for the JES and $\pm 10\%$ for the JER, are drawn for reference. The results in the first two p_T bins ($200 < p_T < 250$ GeV and $250 < p_T < 350$ GeV) correspond to a sample of high-p_T W bosons, and the highest two bins correspond to high-p_T top quarks

trino p_T, and its p_z can be reconstructed using a W-mass constraint (but does not affect the balance measurement). The resulting balance distribution of the probe jet p_T and the recoiling semileptonic top quark decay system has a distinctive peak around 1. The peak position is sensitive to the large-R jet energy scale, and its width is sensitive to the resolution. Measurements of the relative jet mass scale and resolution obtained by fitting the balance distribution with the same forward-folding technique are shown in Fig. 21, after the application of the in situ JES calibration derived from light quark and gluon jets (Sect. 5). The results are compatible with unit JES within the precision of the measurement. This provides another confirmation that the Monte Carlo modelling of the response of high-p_T, hadronically decaying W bosons or top quarks is adequate within 2–3%, and that a calibration derived from jets without hard substructure is applicable to topologies with hard substructure.

7 Measurement of the large-R jet p_T resolution

The in situ measurement of the ATLAS jet p_T resolution[4] relies on a measurement that exploits the momentum balance between the leading and sub-leading large-R jets in dijet

---

[4] The relative resolution $\sigma(p_T)/p_T$ is equal to the relative energy resolution $\sigma(E)/E$ to a good approximation, and the term jet energy resolution is used to refer to both quantities.

events. This measurement follows the event selection criteria outlined for the η-intercalibration provided in Sect. 5.1, including the trigger strategy. The simulation calibration and η-intercalibration described in Sects. 4 and 5.1 are applied to the large-R jets studied here, and the large-R jet p_T is also corrected using the combination of the in situ direct balance techniques discussed in Sects. 5.2, 5.3, and 5.4, which is presented in Sect. 8.

The asymmetry distribution of Sect. 5.1 is studied in dijet events in bins of the dijet system p_T^{avg} and the probe large-R jet η_{det}. The width of the asymmetry distribution depends on the resolution of the jet p_T measurement and on the intrinsic particle-level width, which arises due to balance fluctuations and out-of-cone effects. Since the latter effect is uncorrelated with the detector response, the component of the asymmetry width due to the detector resolution can be determined by subtracting in quadrature the asymmetry width of particle-level ('truth-level') jets from that of reconstructed jets, giving

$$\sigma_{\mathcal{A},\mathrm{det}} = \sqrt{\sigma_{\mathcal{A},\mathrm{reco}}^2 - \sigma_{\mathcal{A},\mathrm{truth}}^2}.$$

The jet energy resolution is measured in two η_{det} bins: the central reference region $|\eta_{det}| < 0.8$, denoted "ref", and a forward region $0.8 < |\eta_{det}| < 2.0$, denoted "fwd". If both large-R jets are within the central reference region, they have the same p_T resolution. In this case, the determination of the probe jet is arbitrary, and the assignment proceeds using a random-number generator. Since both jets contribute the same amount to the asymmetry distribution, the relative jet-p_T resolution of the reference region is defined by

$$\left(\frac{\sigma_{p_T}}{p_T}\right)_{\mathrm{ref}} = \frac{\sigma_{\mathcal{A},\mathrm{det}}^{\mathrm{ref}}}{\sqrt{2}}.$$

The resolution of forward jets is extracted from the width of the asymmetry distribution in events where a central reference jet balances a forward probe jet (in the region $0.8 < |\eta_{det}| < 2.0$). The result is corrected for the resolution of central jets by subtracting the asymmetry of central dijet systems, giving

$$\left(\frac{\sigma_{p_T}}{p_T}\right)_{\mathrm{fwd}} = \sqrt{(\sigma_{\mathcal{A},\mathrm{det}}^{\mathrm{fwd}})^2 - \frac{(\sigma_{\mathcal{A},\mathrm{det}}^{\mathrm{ref}})^2}{2}}. \tag{4}$$

Figure 22 shows $\sigma_{\mathcal{A}}$ for reconstructed- and truth-level dijet systems as a function of p_T^{avg} in two η_{det} bins, as well as for data. For each of the event generators, the width of the detector-level asymmetry is shown as a solid line, while the particle-level asymmetry is indicated by a dashed line. For forward jets, the additional correction shown in Eq. (4) is applied to account for the effect of the resolution of the large-R jet within the central reference region.
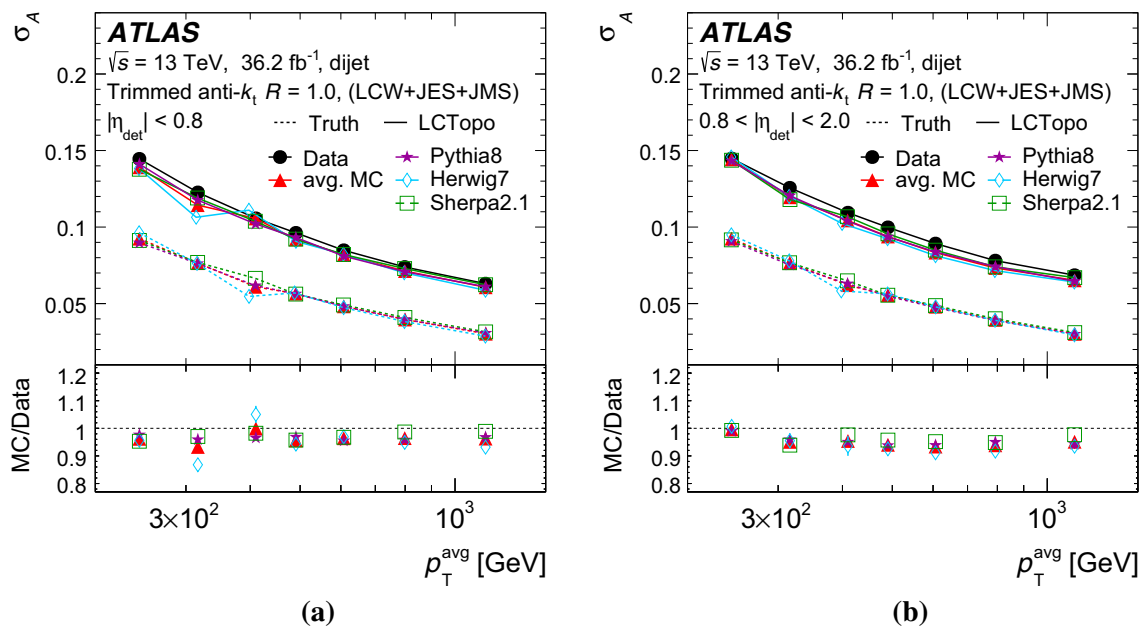
Fig. 22 Width of the dijet asymmetry distribution obtained using reconstructed ($\sigma_{\mathcal{A},\text{reco}}$) and particle-level jets ($\sigma_{\mathcal{A},\text{truth}}$) as a function of the average jet transverse momentum p_T^{avg}. Results are shown **a** for events where both jets have detector pseudorapidity in the range $|\eta_{\text{det}}| < 0.8$ and **b** for events where the probe jet has $0.8 < |\eta_{\text{det}}| < 2.0$, and the reference jet is still within $|\eta_{\text{det}}| < 0.8$. The measurement is compared with the prediction from simulations based on the three gen-

erators PYTHIA 8, HERWIG 7, and SHERPA 2.1. Also an unweighted average of the three is shown. The large-R jet p_T is corrected using the simulation calibration, η-intercalibration, and a combination of in situ direct balance techniques. Statistical errors are usually smaller than the size of the marker. The resolution at the particle level is also shown as a dashed line

Following the correction for the particle-level width, the results of a fit to the asymmetry distribution obtained in data and from several event generators (PYTHIA 8, HERWIG 7, and SHERPA 2.1) are shown in Fig. 23, where the measured relative resolution $\sigma(p_T)/p_T$ is plotted as a function of the average p_T of the two jets, p_T^{avg}. The correction for the particle-level resolution is estimated using the PYTHIA sample. The measured resolution in the central region is in fair agreement with the predicted resolution. The resolution of forward jets in data and simulations is compatible within the observed uncertainties. The choice of event generator has a small effect on the resolution.

In Fig. 23, the relative p_T resolution, $p_T^{\text{reco}}/p_T^{\text{true}}$, as predicted by the simulations is compared with the result of the extraction of the resolution from the asymmetry in simulated events. The difference between the two indicates a bias in the method that is taken as an additional uncertainty (labelled non-closure).

The total uncertainty in the determination of the JER is shown in Fig. 24 as a function of the average p_T and in the two η_{det} regions. A breakdown of the uncertainties into individual sources is presented. The large-R jet energy scale is varied according to its uncertainty, leading to a 10–15% variation in the measured resolution due to its impact on the asymmetry (labelled as 'JES uncertainty'). The non-closure

uncertainty is found to be a nearly constant 10% effect in the central region and to be 5–10% in the forward region. The $\Delta\phi$ requirement is also varied by ± 0.5, which has a small effect primarily for low-p_T jets. The modelling uncertainty is estimated as the variation of the result when using different generators for the particle-level momentum imbalance, where PYTHIA 8 is chosen as a nominal sample and HERWIG 7 and SHERPA 2.1 are chosen as the variations.

8 Combined large-R jet calibration results

The measurements of the trimmed large-R jet response relative to simulation obtained using the different in situ methods presented in Sects. 5 and 6 are combined to determine the relative jet energy and mass scales over a broad range of jet transverse momenta. The combination procedure is described in detail in Ref. [76].

The data-to-simulation response ratios obtained from the γ+jet, Z+jet, and multijet balance methods are combined to produce a jet p_T-dependent calibration curve. The uncertainties in the p_T calibration are obtained by error propagation of the uncertainties associated with the in situ methods. A jet mass calibration is derived analogously using the jet mass response measurements provided by the forward-folding and R_{trk} methods.
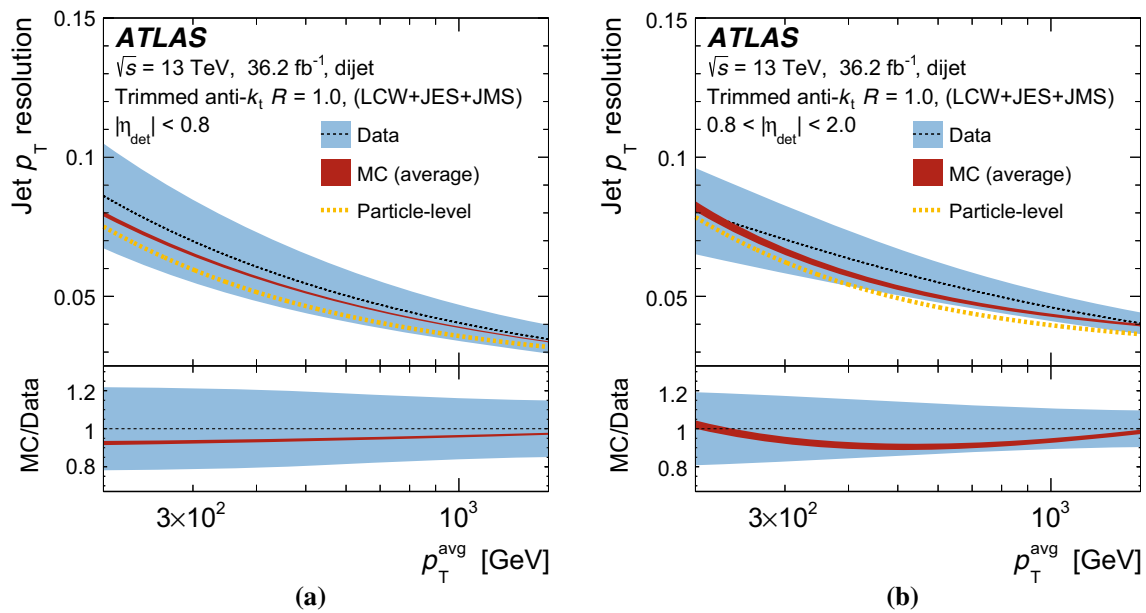
Fig. 23 Comparison of the measured jet p_T resolution with the resolution determined in simulation, averaged between different generators as a function of the average jet p_T and in two bins of detector pseudorapidity η_{det} from **a** $|\eta_{det}| < 0.8$ and from **b** $0.8 < |\eta_{det}| < 2.0$. The large-R jet p_T is corrected using the simulation calibration, η-intercalibration, and a combination of in situ direct balance techniques. The error band, drawn as a light band, represents the statistical and systematic uncertainties added in quadrature. The determination of the relative resolution using the in situ technique for an average of three simulations and their envelope is also shown as a dark band. Inconsistencies between the resolution determined using the in situ technique and of the resolution determined from the response in simulation by matching particle-level jets to reco-level jets (light dotted line) are taken as an additional uncertainty in the measurement. The lines shown are obtained by smoothing a binned representation of these uncertainties using a sliding Gaussian kernel
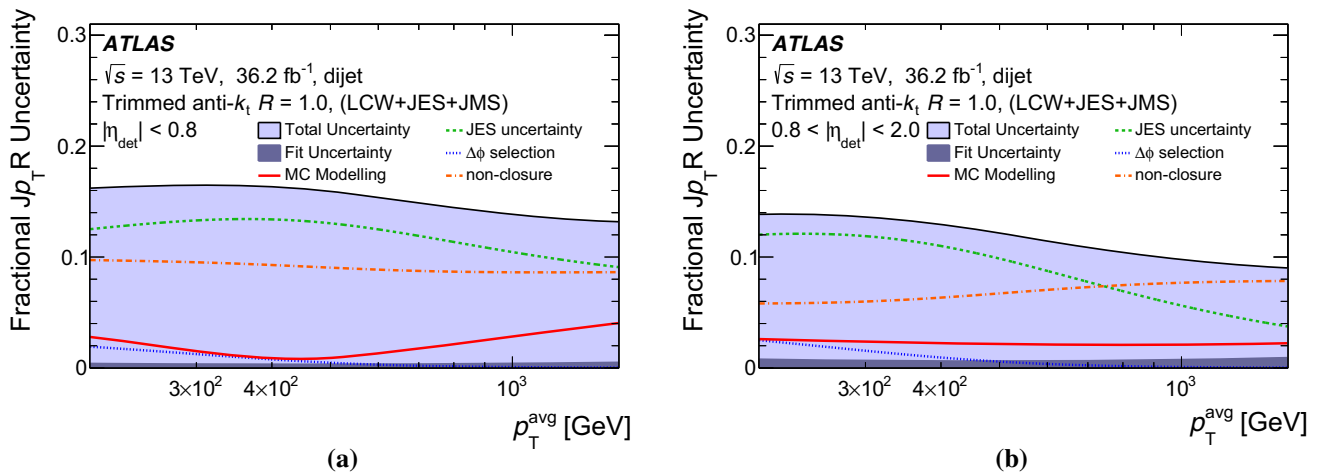

Fig. 24 The relative uncertainty in the ratio of the jet transverse momentum p_T resolution measured in dijet events and in simulations as a function of the average jet p_T in pseudorapidity η bins **a** $|\eta| < 0.8$ and **b** $0.8 < |\eta| < 2.0$. The large-R jet p_T is corrected using the simulation calibration, η-intercalibration, and a combination of in situ direct balance techniques. Contributions from three sources are estimated separately by propagating the uncertainty in the energy scale to the measurement, by varying the $\Delta\phi$ selection, and by varying the event generator. The lines shown are obtained by smoothing a binned representation of these uncertainties using a sliding Gaussian kernel

The measurements of the p_T response are performed in bins of the jet transverse momentum (the p_T^{ref} values are translated to jet p_T) and evaluated inclusively in mass. The jet mass response combination is performed in bins of the jet transverse momentum and in two bins of the jet mass. The combination proceeds in three steps which take into account correlations between uncertainties and possible inconsistencies between the in situ methods:
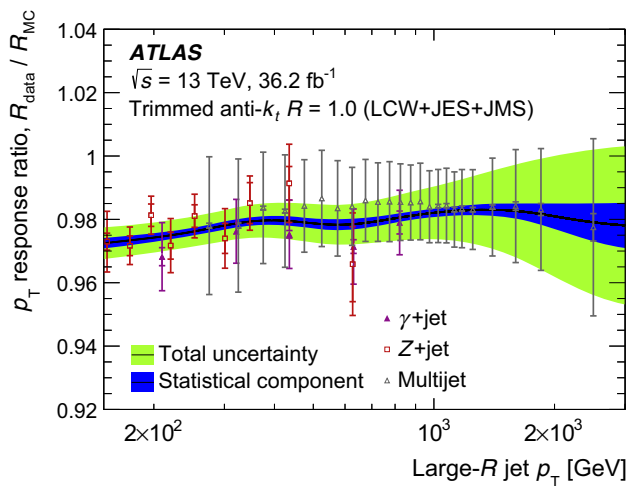
Fig. 25 Data-to-simulation ratio of the average jet p_T response as a function of large-R jet p_T. The combined result (band) is based on three in situ techniques: the Z+jet balance method (open squares), γ+jet balance method (closed triangles), and the multijet balance (open triangles). The errors represent the statistical (inner error bars) and the total uncertainty (statistical and systematic uncertainties added in quadrature, outer error bars). The results apply to trimmed anti-k_t jets with $R = 1.0$. The lines shown are smoothed using a sliding Gaussian kernel
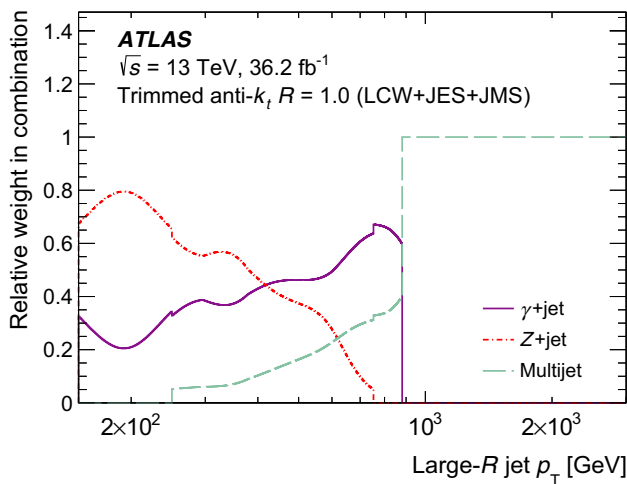

Fig. 26 The weight assigned to different techniques in the combination of in situ measurements of the relative p_T response of large-R jets in data and simulations, as a function of the jet transverse momentum p_T. For each p_T bin, the weight of the Z+jet, γ+jet, and multijet balance methods are shown. The slight discontinuities observed in the weights correspond to the onset of the multijet balance method at $p_T \sim 300$ GeV and to the upper end of the Z+jets method for $p_T \sim 800$ GeV

Fig. 27 The χ^2/N_{dof} of the combination of in situ measurements of the relative jet-p_T response of large-R jets in data and simulations as a function of the jet transverse momentum p_T. The χ^2/N_{dof} indicates the level of tension between the results of the γ+jet and multijet balance methods in each p_T bin. For transverse momenta beyond 1 TeV, only one method is available, and the χ^2/N_{dof} goes to zero

correlations by coherently shifting all correction factors by one standard deviation. The difference between the shifted-correction result and the nominal result provides an estimate of the propagated systematic uncertainty.

- Interpolation: The relative p_T (mass) response is defined in fine p_T bins, separately for each in situ method using interpolating splines based on first- or second-order polynomials.
- Averaging: The actual combination is carried out using a weighted average of the in situ measurements based on a χ^2-minimization. The weights take into account the statistical and systematic uncertainties, as well as correlations and differing bin sizes. The local χ^2 is also useful to define the level of agreement between in situ measurements where they overlap.

The uncertainty sources are treated according to the Hessian formalism: each uncertainty source is fully correlated across kinematic regions (i.e. as a function of p_T and η) but is uncorrelated with other sources. Sources of uncertainty that affect both the small-R and large-R jet in situ calibration are treated as fully correlated. The reduced χ^2 is estimated as $\sqrt{\chi^2/N_{\mathrm{dof}}}$, where N_{dof} is the number of degrees of freedom (in this case, the number of combined measurements contributing to the average in a particular p_T bin). In case of disagreement between different in situ measurements, i.e. when the reduced χ^2 value is larger than 1, the uncertainty sources are rescaled by $\sqrt{\chi^2/N_{\mathrm{dof}}}$.

A smoothing procedure using a variable-size sliding interval with a Gaussian kernel is applied to the response ratio and its associated systematic uncertainties. This smoothing

- Simple Monte Carlo method: Pseudo-experiments are created that represent the ensemble of measurements and contain the full data-treatment chain including interpolation and averaging (described in the following steps). These pseudo-experiments are used to consistently propagate all uncertainties into the evaluation of the average. They are generated taking into account all known
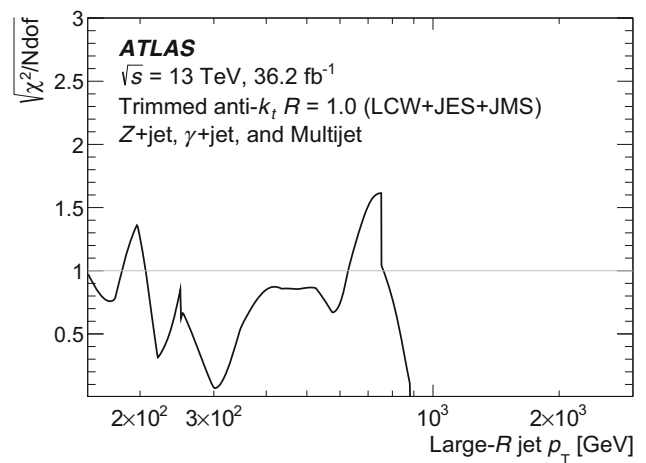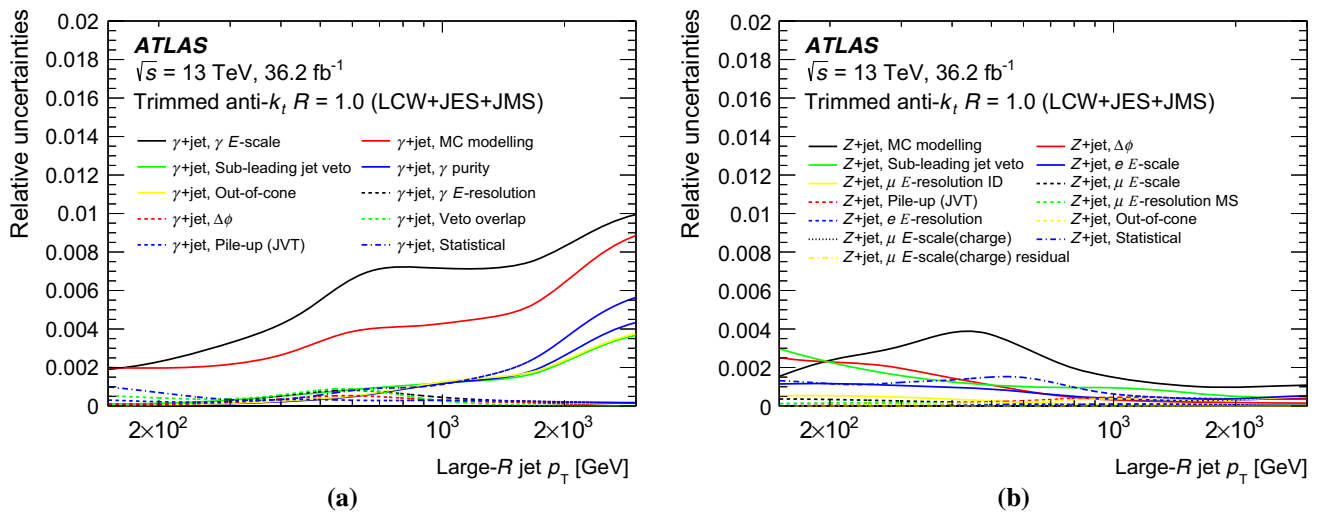
Fig. 28 Breakdown of the combined uncertainty in the large-R jet p_T response as a function of the jet transverse momentum p_T, for the **a** γ+jet and **b** Z+jet analyses. Contributions are shown for each of the nuisance parameters of the γ+jet and Z+jet balance methods. The vertical axis reflects the uncertainty introduced by a given nuisance parameter in combination, incorporating the weight of the method from which it originates. The nuisance parameters related to the γ+jet method (both directly and through their effect on the multijet balance) are shown in the left panel, and those of the Z+jets method are shown in the right panel. The lines shown are smoothed using a sliding Gaussian kernel
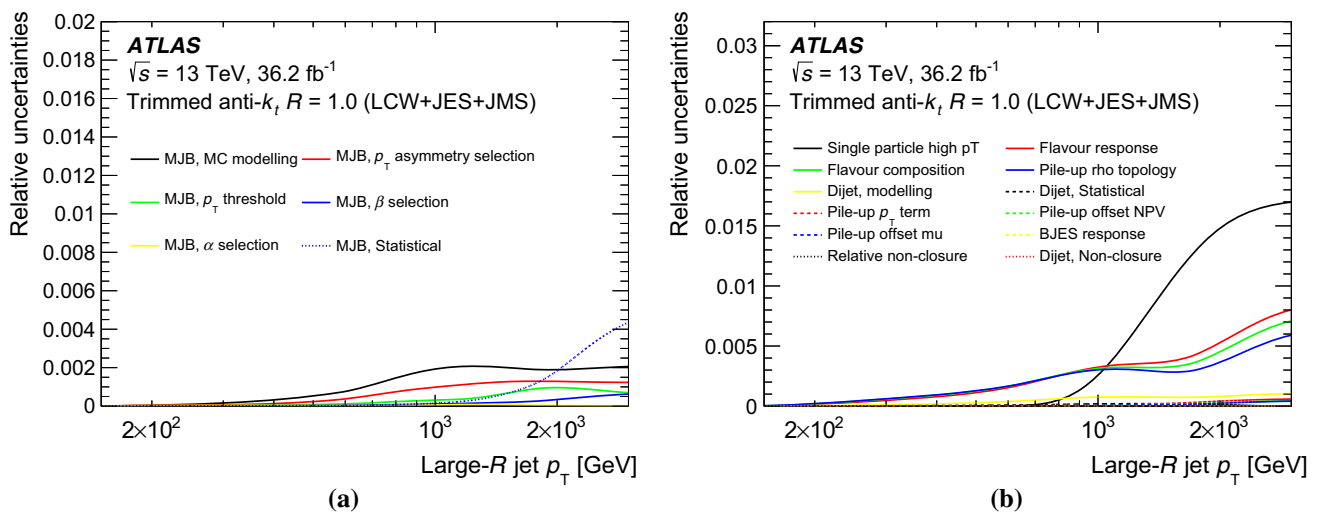

Fig. 29 Breakdown of the combined uncertainty in the large-R jet p_T response as a function of the jet transverse momentum p_T. Contributions are shown for nuisance parameters of the multijet balance method for nuisance parameters **a** originating from the MJB selection and **b** propagated from the small-R jets which constitute the recoil system. The vertical axis reflects the uncertainty introduced by a given nuisance parameter in combination, incorporating the weight of the method from which it originates. Since the multijet balance method relies on the small-R jet p_T, nuisance parameters from all associated uncertainties are propagated. The lines shown are smoothed using a sliding Gaussian kernel

removes spikes due to statistical fluctuations in the measurements, as well as discontinuities at the first and last point in a given measurement.

In Fig. 25, the ratio of the jet p_T response in data and simulations is shown as a function of the jet transverse momentum. Data points are shown for the γ+jet, Z+jet, and multijet balance methods, and the band corresponds to the result of the combination.

The relative weight in the fit of the three methods is shown in Fig. 26. The Z+jet balance makes the largest contribu-

tion up to transverse momenta of approximately 500 GeV. Between 500 GeV and 1 TeV, the γ+jet balance receives the largest weight. At higher p_T, the multijet balance method acquires more weight in the combination. Beyond 1 TeV, it provides the only measurement and extends the jet energy scale beyond 2 TeV.

The local χ^2 per degree of freedom in Fig. 27 quantifies the level of agreement between the three sets of measurements. The results of the three methods agree in the whole p_T range 0.1 TeV < p_T < 1 TeV, where all three provide results.

The combined p_T response in data is approximately 3% lower than in the simulation over most of the p_T range. The deviation from unity in the data/MC ratio is significant, as the total uncertainty approaches 1% in the intermediate p_T region. These observations are consistent with previous in situ measurements of the $R = 0.4$ JES during Run 2 [9] with similar levels of associated uncertainty. At low p_T, the uncertainty reaches about 1% at 200 GeV. Above 1.5 TeV, the uncertainty increases, reaching over 2% at 2.4 TeV.

A breakdown of the total JES uncertainty is presented graphically in Figs. 28 and 29. This includes uncertainties in γ+jet, Z+jet, and multijet balance methods associated with the simulation modelling, reference system construction and calibration, and the event selection. Furthermore, as the large-R multijet balance method uses small-R jets as a reference system, all nuisance parameters from the small-R jet calibration enter as uncertainties in the combination presented here.

The combination of the jet mass response includes results from two methods. Forward folding provides four measurements in the p_T range below 1 TeV. The R_{trk} method takes advantage of a large data sample and can be finely binned in mass and p_T, extending to over 2 TeV. The combined result is shown in Fig. 30 for two jet mass intervals: the plot in the upper panel corresponds to the W boson mass window with $50\,\text{GeV} < m < 120\,\text{GeV}$, and the lower panel corresponds to the top quark mass window with $120\,\text{GeV} < m < 300\,\text{GeV}$.

The in situ jet mass calibration factor is defined from the combined mass response shown in Figure 30 as $c_m = R_{MC}^m / R_{data}^m$. It is applied as a scale factor to the jet mass but does not affect the jet momentum vector. The full calibration applied to large-R jets in data impacts the reconstructed jet energy, mass, pseudorapidity, and p_T according to

$$E_{reco} = c_s \sqrt{E_0^2 + c_{JMS}\, m_0 \left(c_m^2 - 1\right)},$$

$$m_{reco} = c_s\, c_{JMS}\, c_m\, m_0,$$

$$\eta_{reco} = \eta_0 + \Delta\eta,$$

$$p_T^{reco} = c_s \sqrt{\left(E_0^2 - c_{JMS}^2\, m_0^2\right)} \cosh\left(\eta + \Delta\eta\right),$$

where $c_s = c_{JES}\, c_{abs}\, c_{rel}$ is the product of several calibration factors. The factor c_{JES} corresponds to the simulation-based JES calibration, c_{rel} to the relative in situ correction obtained from the η-intercalibration, and c_{abs} to the absolute in situ correction from the balance methods. All c-factors and the factor $\Delta\eta$ are smooth functions of the large-R jet kinematics. The terms E_0, m_0, η_0 and $\vec{p}_0$ refer to the jet properties prior to any calibration, as returned by the trimming algorithm.

The measured JMS correction is consistent with unity within the precision of the combined measurements. This suggests that the application of an in situ JES correction is sufficient to correct the JMS of these trimmed large-R jets in
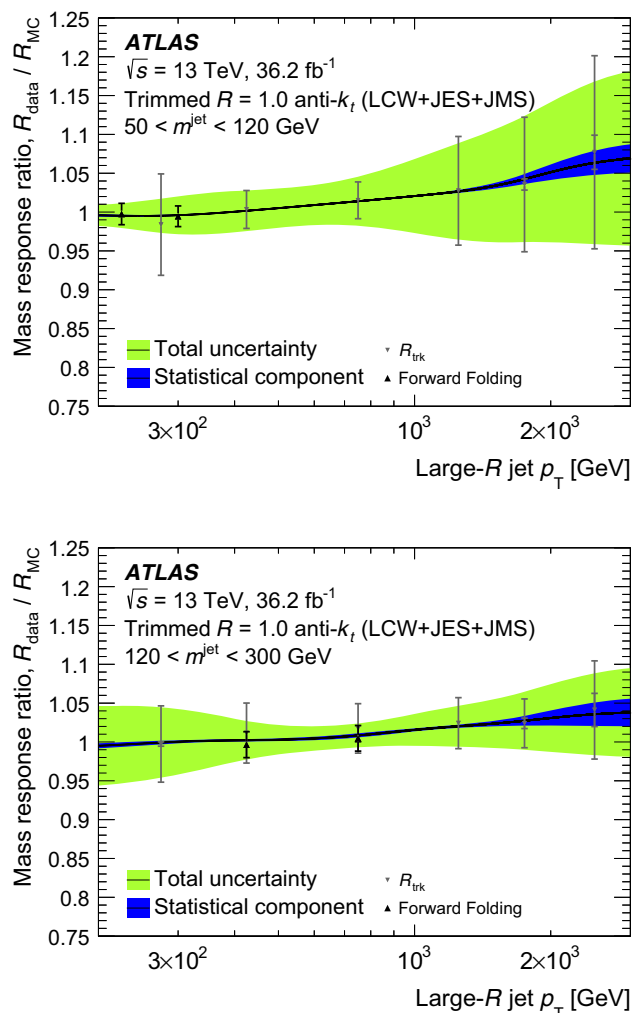
Fig. 30 Data-to-simulation ratio of the average jet mass response as a function of the large-R jet p_T. Corrections using a combination of two in situ methods, the R_{trk} and forward-folding approaches, are applied. The fit is performed for large-R jet mass in the W mass range 50–120 GeV (upper), and the top mass range 120–300 GeV (lower). The error bars represent the statistical and systematic uncertainties added in quadrature. The results apply to anti-k_t jets with $R = 1.0$ calibrated with the LC+JES+JMS scheme. The lines shown are smoothed using a sliding Gaussian kernel

the mass and p_T ranges considered here. The level of precision with which the JMS is measured depends on the kinematic region in question. For large-R jets in the high-mass bin with p_T between 400 GeV and 1 TeV, the uncertainties are 2–5%. In other kinematic regions the uncertainty is larger, approaching 10% at high p_T in both mass bins.

The contributions of several sources to the uncertainty in the combined jet mass scale are presented in Figs. 31 and 32. In both the R_{trk} and forward-folding techniques, the leading systematic uncertainties are associated with uncertainties in the event generators across most of the p_T range and for the two mass intervals considered.

(a)

(b)

Fig. 31 Breakdown of the combined JMS uncertainty shown in Fig. 30 as a function of jet transverse momentum p_T for the jet mass bin 50–120 GeV. Contributions are shown for each of the nuisance parameters of the **a** R_{trk} and **b** forward-folding methods. The vertical axis reflects the uncertainty introduced by a given nuisance parameter in combination, incorporating the 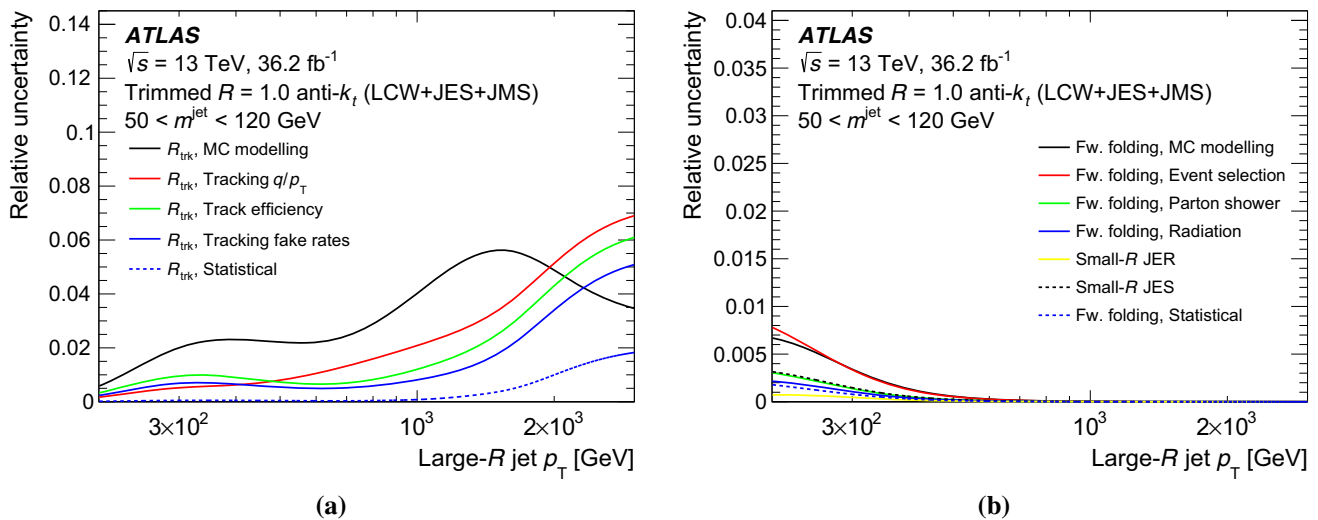weight of the method from which it originates. This weight is dominated at high p_T by the R_{trk} method. The lines shown are smoothed using a sliding Gaussian kernel

(a)

(b)
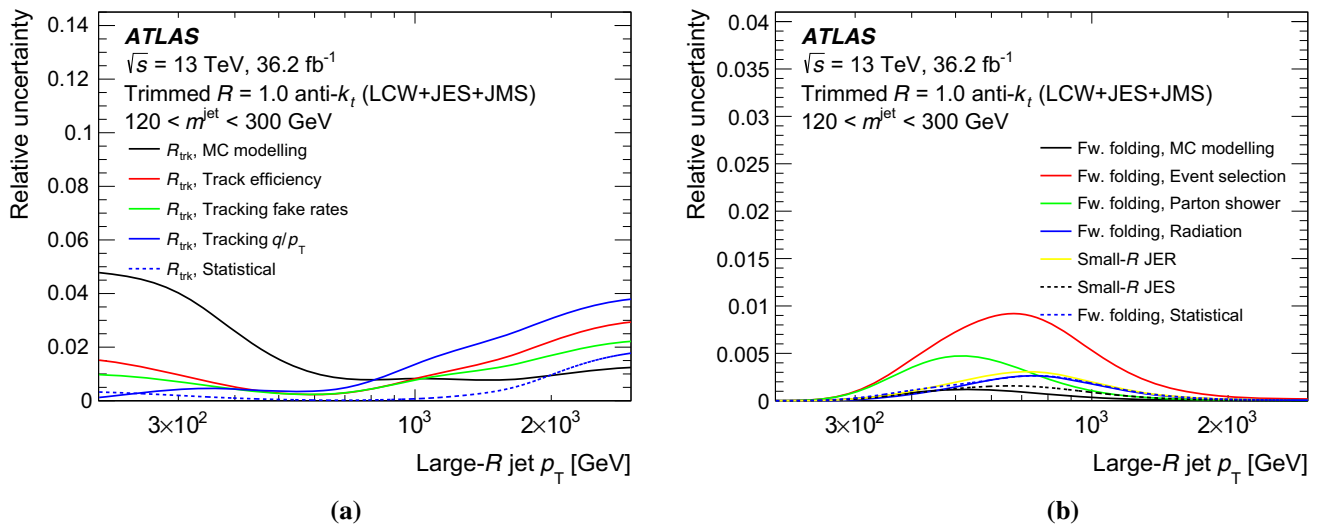
Fig. 32 Breakdown of the combined JMS uncertainty shown in Fig. 30 as a function of jet transverse momentum p_T for the jet mass bin 120–300 GeV. Contributions are shown for each of the nuisance parameters of the **a** R_{trk} and **b** forward-folding methods. The vertical axis reflects the uncertainty introduced by a given nuisance parameter in combination, incorporating the weight of the method from which it originates. This weight is dominated at high p_T by the R_{trk} method. The lines shown are smoothed using a sliding Gaussian kernel

9 Conclusion

Several in situ calibration methods are used to measure the response of the ATLAS detector to trimmed large-R jets using 36.2 fb^{-1} of $\sqrt{s} = 13$ TeV proton–proton collision data provided by the LHC and collected by the ATLAS experiment during 2015 and 2016. These methods exploit the transverse momentum balance in events where a jet recoils against a reference system with a precisely known energy scale, the independence of measurements performed with different sub-detectors, or the position and width of known mass peaks. With this ensemble of techniques, dedicated jet energy scale and jet mass scale calibrations are derived for large-R jets. The results of several techniques applied to a variety of final states are consistent within the uncertainties, indicating that after calibration, the simulations model the flavour dependence of the jet p_T and mass response to within a few percent.

The results of all methods are combined taking into account correlations between uncertainties and possible discrepancies between the results of different in situ methods. The combined measurement of the ratio of the energy scales in data and simulations are used to derive an in situ correction to the response, which determines the large-R jet energy and mass scales. The residual uncertainty in the ratio of the energy scales in data and simulations is 1–2% for transverse momenta from 150 GeV to 2 TeV. The precision of the jet mass scale varies from 2 to 10% over the same p_T range. The results of the simulations for jet p_T and mass resolution are also validated in situ and found to agree with the measured resolution within 10–15%. The in situ JES calibration, derived from light quark and gluon jets, is found to fully correct the energy and mass scales of high p_T W bosons and top quarks to within the precision of the present measurement (1–3%).

Large-R jets are a vital ingredient of the ATLAS physics programme. This new in situ calibration leads to significantly reduced uncertainties in the reconstructed large-R jet p_T and mass, thus increasing the sensitivity of searches and the precision of Standard Model measurements using large-R jets.

Data Availability Statement This manuscript has no associated data or the data will not be deposited. [Authors' comment: "All ATLAS scientific output is published in journals, and preliminary results are made available in Conference Notes. All are openly available, without restriction on use by external parties beyond copyright law and the standard conditions agreed by CERN. Data associated with journal publications are also made available: tables and data from plots (e.g. cross section values, likelihood profiles, selection efficiencies, cross section limits, ...) are stored in appropriate repositories such as HEPDATA (http://hepdata.cedar.ac.uk/). ATLAS also strives to make additional material related to the paper available that allows a reinterpretation of the data in the context of new theoretical models. For example, an extended encapsulation of the analysis is often provided for measurements in the framework of RIVET (http://rivet.hepforge.org/)." This information is taken from the ATLAS Data Access Policy, which is a public document that can be downloaded from http://opendata.cern.ch/record/413 [opendata.cern.ch].]

References

1. A.J. Larkoski, I. Moult, B. Nachman, jet substructure at the large hadron collider: a review of recent advances in theory and machine learning (2017). arXiv:1709.04464 [hep-ph]
2. L. Asquith et al., Jet substructure at the large hadron collider: experimental review (2018). arXiv:1803.06991 [hep-ex]
3. ATLAS Collaboration, Performance of jet substructure techniques for large-R jets in proton–proton collisions at $\sqrt{s} = 7$ TeV using the ATLAS detector. JHEP **09**, 076 (2013). arXiv:1306.4945 [hep-ex]
4. ATLAS Collaboration, Performance of top-quark and W-boson tagging with ATLAS in Run 2 of the LHC (2018). arXiv:1808.07858 [hep-ex]
5. ATLAS Collaboration, Topological cell clustering in the ATLAS calorimeters and its performance in LHC Run 1. Eur. Phys. J. C **77**, 490 (2017). arXiv:1603.02934 [hep-ex]
6. M. Cacciari, G.P. Salam, G. Soyez, The anti-k_t jet clustering algorithm. JHEP **04**, 063 (2008). arXiv:0802.1189 [hep-ph]
7. D. Krohn, J. Thaler, L.T. Wang, Jet trimming. JHEP **02**, 084 (2010). arXiv:0912.1342 [hep-ph]
8. ATLAS Collaboration, Jet mass and substructure of inclusive jets in $\sqrt{s} = 7$ TeV pp collisions with the ATLAS experiment. JHEP **05**, 128 (2012). arXiv:1203.4606 [hep-ex]
9. ATLAS Collaboration, Jet energy scale measurements and their systematic uncertainties in proton–proton collisions at $\sqrt{s} = 13$ TeV with the ATLAS detector. Phys. Rev. D **96**, 072,002 (2017). arXiv:1703.09665 [hep-ex]
10. ATLAS Collaboration, Measurement of large radius jet mass reconstruction performance at $\sqrt{s} = 8$ TeV using the ATLAS detector. ATLAS-CONF-2016-008 (2016). https://cds.cern.ch/record/2139642
11. ATLAS Collaboration, Performance of the ATLAS trigger system in 2015. Eur. Phys. J. C **77**, 317 (2017). arXiv:1611.09661 [hep-ex]
12. ATLAS Collaboration, The ATLAS experiment at the CERN large hadron collider. JINST **3**, S08003 (2008)
13. ATLAS Collaboration, The ATLAS simulation infrastructure. Eur. Phys. J. C **70**, 823 (2010). arXiv:1005.4568 [physics.ins-det]
14. S. Agostinelli et al., GEANT4—a simulation toolkit. Nucl. Instrum. Methods A **506**, 250–303 (2003)

15. T. Sjöstrand et al., An introduction to PYTHIA 8.2. Comput. Phys. Commun. **191**, 159–177 (2015). arXiv:1410.3012 [hep-ph]

16. S. Alioli, P. Nason, C. Oleari, E. Re, A general framework for implementing NLO calculations in shower Monte Carlo programs: the POWHEG BOX. JHEP **06**, 043 (2010). arXiv:1002.2581 [hep-ph]

17. S. Frixione, P. Nason, C. Oleari, Matching NLO QCD computations with parton shower simulations: the POWHEG method. JHEP **11**, 070 (2007). arXiv:0709.2092 [hep-ph]

18. P. Nason, A new method for combining NLO QCD with shower Monte Carlo algorithms. JHEP **11**, 040 (2004). arXiv:hep-ph/0409146

19. ATLAS Collaboration, ATLAS Pythia 8 tunes to 7 TeV data. ATL-PHYS-PUB-2014-021 (2014). https://cds.cern.ch/record/1966419

20. R.D. Ball et al., Parton distributions for the LHC Run II. JHEP **04**, 040 (2015). arXiv:1410.8849 [hep-ph]

21. M. Bahr et al., Herwig++ physics and manual. Eur. Phys. J. C **58**, 639 (2008). arXiv:0803.0883 [hep-ph]

22. T. Gleisberg et al., Event generation with SHERPA 1.1. JHEP **02**, 007 (2009). arXiv:0811.4622 [hep-ph]

23. S. Gieseke, C. Röhr, A. Siódmok, Colour reconnections in Herwig++. Eur. Phys. J. C **72**, 2225 (2012). arXiv:1206.0041 [hep-ph]

24. J. Pumplin et al., New generation of parton distributions with uncertainties from global QCD analysis. JHEP **07**, 012 (2002). arXiv:hep-ph/0201195

25. S. Catani, F. Krauss, R. Kuhn, B.R. Webber, QCD matrix elements + parton showers. JHEP **11**, 063 (2001). arXiv:hep-ph/0109231

26. H.L. Lai et al., New parton distributions for collider physics. Phys. Rev. D **82**, 074024 (2010). arXiv:1007.2241 [hep-ph]

27. ATLAS Collaboration, Measurement of the Z/γ^* boson transverse momentum distribution in pp collisions at $\sqrt{s} = 7$ TeV with the ATLAS detector. JHEP **09**, 145 (2014). arXiv:1406.3660 [hep-ex]

28. D.J. Lange, The EvtGen particle decay simulation package. Nucl. Instrum. Methods A **462**, 152 (2001)

29. N. Davidson, T. Przedzinski, Z. Was, PHOTOS interface in C++: technical and physics documentation (2010). arXiv:1011.0937 [hep-ph]

30. T. Gleisberg, S. Höche, Comix, a new matrix element generator. JHEP **12**, 039 (2008). arXiv:0808.3674 [hep-ph]

31. F. Cascioli, P. Maierhofer, S. Pozzorini, Scattering amplitudes with open loops. Phys. Rev. Lett. **108**, 111601 (2012). arXiv:1111.5206 [hep-ph]

32. S. Schumann, F. Krauss, A parton shower algorithm based on Catani–Seymour dipole factorisation. JHEP **03**, 038 (2008). arXiv:0709.1027 [hep-ph]

33. S. Höche, F. Krauss, M. Schönherr, F. Siegert, QCD matrix elements + parton showers: the NLO case. JHEP **04**, 027 (2013). arXiv:1207.5030 [hep-ph]

34. S. Frixione, P. Nason, G. Ridolfi, A positive-weight next-to-leading-order Monte Carlo for heavy flavour hadroproduction. JHEP **09**, 126 (2007). arXiv:0707.3088 [hep-ph]

35. ATLAS Collaboration, Summary of ATLAS Pythia 8 tunes. ATL-PHYS-PUB-2012-003 (2012). https://cds.cern.ch/record/1474107

36. A.D. Martin, W.J. Stirling, R.S. Thorne, G. Watt, Parton distributions for the LHC. Eur. Phys. J. C **63**, 189 (2009). arXiv:0901.0002 [hep-ph]

37. M. Cacciari, G.P. Salam, G. Soyez, FastJet user manual. Eur. Phys. J. C **72**, 1896 (2012). arXiv:1111.6097 [hep-ph]

38. M. Cacciari, G.P. Salam, Dispelling the N^3 myth for the k_t jet-finder. Phys. Lett. B **641**, 57 (2006). arXiv:hep-ph/0512210

39. S.D. Ellis, D.E. Soper, Successive combination jet algorithm for hadron collisions. Phys. Rev. D **48**, 3160 (1993). arXiv:hep-ph/9305266

40. ATLAS Collaboration, Monte Carlo calibration and combination of in-situ measurements of jet energy scale, jet energy resolution and jet mass in ATLAS. ATLAS-CONF-2015-037 (2015). https://cds.cern.ch/record/2044941

41. ATLAS Collaboration, Performance of the ATLAS inner detector track and vertex reconstruction in high pile-up LHC environment. ATLAS-CONF-2012-042 (2012). https://cds.cern.ch/record/1435196

42. ATLAS Collaboration, Early inner detector tracking performance in the 2015 data at $\sqrt{s} = 13$ TeV. ATL-PHYS-PUB-2015-051 (2015). https://cds.cern.ch/record/2110140

43. ATLAS Collaboration, Jet mass reconstruction with the ATLAS Detector in early Run 2 data. ATLAS-CONF-2016-035 (2016). https://cds.cern.ch/record/2200211

44. M. Son, C. Spethmann, B. Tweedie, Diboson-jets and the search for resonant Zh production. JHEP **08**, 160 (2012). arXiv:1204.0525 [hep-ph]

45. A. Katz, M. Son, B. Tweedie, Jet substructure and the search for neutral spin-one resonances in electroweak Boson channels. JHEP **03**, 011 (2011). arXiv:1010.5253 [hep-ph]

46. S. Schätzel, M. Spannowsky, Tagging highly boosted top quarks. Phys. Rev. D **89**, 014007 (2014). arXiv:1308.0540 [hep-ph]

47. T. Plehn, M. Spannowsky, M. Takeuchi, D. Zerwas, Stop reconstruction with tagged tops. JHEP **10**, 078 (2010). arXiv:1006.2833 [hep-ph]

48. T. Plehn, G.P. Salam, M. Spannowsky, Fat Jets for a Light Higgs. Phys. Rev. Lett. **104**, 111801 (2010). arXiv:0910.5472 [hep-ph]

49. A.J. Larkoski, F. Maltoni, M. Selvaggi, Tracking down hyper-boosted top quarks. JHEP **06**, 032 (2015). arXiv:1503.03347 [hep-ph]

50. S. Bressler, T. Flacke, Y. Kats, S.J. Lee, G. Perez, Hadronic calorimeter shower size: challenges and opportunities for jet substructure in the superboosted regime. Phys. Lett. B **756**, 137 (2016). arXiv:1506.02656 [hep-ph]

51. B.T. Elder, J. Thaler, Aspects of track-assisted mass (2018). arXiv:1805.11109 [hep-ph]

52. M. Cacciari, G.P. Salam, G. Soyez, The catchment area of jets. JHEP **04**, 005 (2008). arXiv:0802.1188 [hep-ph]

53. ATLAS Collaboration, Jet energy measurement and its systematic uncertainty in proton–proton collisions at $\sqrt{s} = 7$ TeV with the ATLAS detector. Eur. Phys. J. C **75**, 17 (2015). arXiv:1406.0076 [hep-ex]

54. ATLAS Collaboration, Performance of pile-up mitigation techniques for jets in pp collisions at $\sqrt{s} = 8$ TeV using the ATLAS detector. Eur. Phys. J. C **76**, 581 (2016). arXiv:1510.03823 [hep-ex]

55. ATLAS Collaboration, Tagging and suppression of pileup jets with the ATLAS detector. ATLAS-CONF-2014-018 (2014). https://cds.cern.ch/record/1700870

56. ATLAS Collaboration, Electron efficiency measurements with the ATLAS detector using 2012 LHC proton–proton collision data. Eur. Phys. J. C **77**, 195 (2017). arXiv:1612.01456 [hep-ex]

57. ATLAS Collaboration, Electron efficiency measurements with the ATLAS detector using the 2015 LHC proton–proton collision data. ATLAS-CONF-2016-024 (2016). https://cds.cern.ch/record/2157687

58. ATLAS Collaboration, Muon reconstruction performance of the ATLAS detector in proton–proton collision data at $\sqrt{s} = 13$ TeV. Eur. Phys. J. C **76**, 292 (2016). arXiv:1603.05598 [hep-ex]

59. ATLAS Collaboration, Photon identification in 2015 ATLAS data. ATL-PHYS-PUB-2016-014 (2016). https://cds.cern.ch/record/2203125

60. ATLAS Collaboration, Measurement of the photon identification efficiencies with the ATLAS detector using LHC Run-1 data. Eur. Phys. J. C **76**, 666 (2016). arXiv:1606.01813 [hep-ex]

61. ATLAS Collaboration, Measurement of the inclusive isolated prompt photon cross section in pp collisions at $\sqrt{s} = 7$ TeV with the ATLAS detector. Phys. Rev. D **83**, 052005 (2011). arXiv:1012.4389 [hep-ex]

66. ATLAS Collaboration, Track reconstruction performance of the ATLAS inner detector at $\sqrt{s}$ = 13 TeV. ATL-PHYS-PUB-2015-018 (2015). https://cds.cern.ch/record/2037683

67. ATLAS Collaboration, Performance of the ATLAS track reconstruction algorithms in dense environments in LHC Run 2. Eur. Phys. J. C **77**, 673 (2017). arXiv:1704.07983 [hep-ex]

68. ATLAS Collaboration, Studies of radial distortions of the ATLAS inner detector. ATL-PHYS-PUB-2018-003 (2018). https://cds.cern.ch/record/2309785

69. ATLAS Collaboration, Identification of boosted, hadronically decaying W bosons and comparisons with ATLAS data taken at $\sqrt{s}$ = 8 TeV. Eur. Phys. J. C **76**, 154 (2016). arXiv:1510.05821 [hep-ex]

70. ATLAS Collaboration, Identification of high transverse momentum top quarks in pp collisions at $\sqrt{s}$ = 8 TeV with the ATLAS detector. JHEP **06**, 093 (2016). arXiv:1603.03127 [hep-ex]

71. ATLAS Collaboration, Search for heavy particles decaying into top-quark pairs using lepton-plus-jets events in proton–proton collisions at $\sqrt{s}$ = 13 TeV with the ATLAS detector. Eur. Phys. J. C **78**, 565 (2018). arXiv:1804.10823 [hep-ex]

72. ATLAS Collaboration, Performance of missing transverse momentum reconstruction with the ATLAS detector using proton–proton collisions at $\sqrt{s}$ = 13 TeV (2018) arXiv:1802.08168 [hep-ex]

73. ATLAS Collaboration, Measurements of b-jet tagging efficiency with the ATLAS detector using $t\bar{t}$ events at $\sqrt{s}$ = 13 TeV. JHEP **08**, 089 (2018). arXiv:1805.01845 [hep-ex]

74. ATLAS Collaboration, In-situ measurements of the ATLAS large-radius jet response in 13 TeV pp collisions. ATLAS-CONF-2017-063 (2017). https://cds.cern.ch/record/2275655

75. ATLAS Collaboration, A search for $t\bar{t}$ resonances using lepton-plus-jets events in proton–proton collisions at $\sqrt{s}$ = 8 TeV with the ATLAS detector. JHEP **08**, 148 (2015). arXiv:1505.07018 [hep-ex]

76. ATLAS Collaboration, Jet energy measurement with the ATLAS detector in proton–proton collisions at $\sqrt{s}$ = 7 TeV. Eur. Phys. J. C **73**, 2304 (2013). arXiv:1112.6426 [hep-ex]

77. ATLAS Collaboration, ATLAS computing acknowledgements. ATL-GEN-PUB-2016-002. https://cds.cern.ch/record/2202407

ATLAS Collaboration

M. Aaboud[34d], G. Aad[99], B. Abbott[124], O. Abdinov[13,*], B. Abeloos[128], D. K. Abhayasinghe[91], S. H. Abidi[164], O. S. AbouZeid[39], N. L. Abraham[153], H. Abramowicz[158], H. Abreu[157], Y. Abulaiti[6], B. S. Acharya[64a,64b,n], S. Adachi[160], L. Adam[97], L. Adamczyk[81a], J. Adelman[119], M. Adersberger[112], A. Adiguzel[12c,af], T. Adye[141], A. A. Affolder[143], Y. Afik[157], C. Agheorghiesei[27c], J. A. Aguilar-Saavedra[136a,136f], F. Ahmadov[77,ad], G. Aielli[71a,71b], S. Akatsuka[83], T. P. A. Åkesson[94], E. Akilli[52], A. V. Akimov[108], G. L. Alberghi[23a,23b], J. Albert[173], P. Albicocco[49], M. J. Alconada Verzini[86], S. Alderweireldt[117], M. Aleksa[35], I. N. Aleksandrov[77], C. Alexa[27b], T. Alexopoulos[10], M. Alhroob[124], B. Ali[138], G. Alimonti[66a], J. Alison[36], S. P. Alkire[145], C. Allaire[128], B. M. M. Allbrooke[153], B. W. Allen[127], P. P. Allport[21], A. Aloisio[67a,67b], A. Alonso[39], F. Alonso[86], C. Alpigiani[145], A. A. Alshehri[55], M. I. Alstaty[99], B. Alvarez Gonzalez[35], D. Álvarez Piqueras[171], M. G. Alviggi[67a,67b], B. T. Amadio[18], Y. Amaral Coutinho[78b], A. Ambler[101], L. Ambroz[131], C. Amelung[26], D. Amidei[103], S. P. Amor Dos Santos[136a,136c], S. Amoroso[44], C. S. Amrouche[52], C. Anastopoulos[146], L. S. Ancu[52], N. Andari[142], T. Andeen[11], C. F. Anders[59b], J. K. Anders[20], K. J. Anderson[36], A. Andreazza[66a,66b], V. Andrei[59a], C. R. Anelli[173], S. Angelidakis[37], I. Angelozzi[118], A. Angerami[38], A. V. Anisenkov[120a,120b], A. Annovi[69a], C. Antel[59a], M. T. Anthony[146], M. Antonelli[49], D. J. A. Antrim[168], F. Anulli[70a], M. Aoki[79], J. A. Aparisi Pozo[171], L. Aperio Bella[35], G. Arabidze[104], J. P. Araque[136a], V. Araujo Ferraz[78b], R. Araujo Pereira[78b], A. T. H. Arce[47], R. E. Ardell[91], F. A. Arduh[86], J-F. Arguin[107], S. Argyropoulos[75], A. J. Armbruster[35], L. J. Armitage[90], A Armstrong[168], O. Arnaez[164], H. Arnold[118], M. Arratia[31], O. Arslan[24], A. Artamonov[109,*], G. Artoni[131], S. Artz[97], S. Asai[160], N. Asbah[57], E. M. Asimakopoulou[169], L. Asquith[153], K. Assamagan[29], R. Astalos[28a], R. J. Atkin[32a], M. Atkinson[170], N. B. Atlay[148], K. Augsten[138], G. Avolio[35], R. Avramidou[58a], M. K. Ayoub[15a], G. Azuelos[107,aq], A. E. Baas[59a], M. J. Baca[21], H. Bachacou[142], K. Bachas[65a,65b], M. Backes[131], P. Bagnaia[70a,70b], M. Bahmani[82], H. Bahrasemani[149], A. J. Bailey[171], J. T. Baines[141], M. Bajic[39], C. Bakalis[10], O. K. Baker[180], P. J. Bakker[118], D. Bakshi Gupta[93], S. Balaji[154], E. M. Baldin[120a,120b], P. Balek[177], F. Balli[142], W. K. Balunas[133], J. Balz[97], E. Banas[82], A. Bandyopadhyay[24], S. Banerjee[178,j], A. A. E. Bannoura[179], L. Barak[158], W. M. Barbe[37], E. L. Barberio[102], D. Barberis[53a,53b], M. Barbero[99], T. Barillari[113], M-S. Barisits[35], J. Barkeloo[127], T. Barklow[150], R. Barnea[157], S. L. Barnes[58c], B. M. Barnett[141], R. M. Barnett[18], Z. Barnovska-Blenessy[58a], A. Baroncelli[72a], G. Barone[26], A. J. Barr[131], L. Barranco Navarro[171], F. Barreiro[96], J. Barreiro Guimarães da Costa[15a], R. Bartoldus[150], A. E. Barton[87], P. Bartos[28a], A. Basalaev[134], A. Bassalat[128], R. L. Bates[55], S. J. Batista[164], S. Batlamous[34e], J. R. Batley[31], M. Battaglia[143], M. Bauce[70a,70b], F. Bauer[142], K. T. Bauer[168], H. S. Bawa[150,l], J. B. Beacham[122], T. Beau[132], P. H. Beauchemin[167], P. Bechtle[24], H. C. Beck[51], H. P. Beck[20,p], K. Becker[50], M. Becker[97], C. Becot[44], A. Beddall[12d], A. J. Beddall[12a], V. A. Bednyakov[77], M. Bedognetti[118], C. P. Bee[152], T. A. Beermann[35], M. Begalli[78b], M. Begel[29], A. Behera[152], J. K. Behr[44], A. S. Bell[92], G. Bella[158], L. Bellagamba[23b], A. Bellerive[33], M. Bellomo[157], P. Bellos[9], K. Belotskiy[110], N. L. Belyaev[110], O. Benary[158,*], D. Benchekroun[34a], M. Bender[112], N. Benekos[10], Y. Benhammou[158], E. Benhar Noccioli[180], J. Benitez[75], D. P. Benjamin[47], M. Benoit[52], J. R. Bensinger[26], S. Bentvelsen[118],

L. Beresford[131],   M. Beretta[49],   D. Berge[44],   E. Bergeaas Kuutmann[169],   N. Berger[5],   L. J. Bergsten[26],   J. Beringer[18],
S. Berlendis[7],   N. R. Bernard[100],   G. Bernardi[132],   C. Bernius[150],   F. U. Bernlochner[24],   T. Berry[91],   P. Berta[97],   C. Bertella[15a],
G. Bertoli[43a,43b],   I. A. Bertram[87],   G. J. Besjes[39],   O. Bessidskaia Bylund[179],   M. Bessner[44],   N. Besson[142],   A. Bethani[98],
S. Bethke[113],   A. Betti[24],   A. J. Bevan[90],   J. Beyer[113],   R. Bi[135],   R. M. B. Bianchi[135],   O. Biebel[112],   D. Biedermann[19],
R. Bielski[35],   K. Bierwagen[97],   N. V. Biesuz[69a,69b],   M. Biglietti[72a],   T. R. V. Billoud[107],   M. Bindi[51],   A. Bingul[12d],
C. Bini[70a,70b],   S. Biondi[23a,23b],   M. Birman[177],   T. Bisanz[51],   J. P. Biswal[158],   C. Bittrich[46],   D. M. Bjergaard[47],   J. E. Black[150],
K. M. Black[25],   T. Blazek[28a],   I. Bloch[44],   C. Blocker[26],   A. Blue[55],   U. Blumenschein[90],   Dr. Blunier[144a],   G. J. Bobbink[118],
V. S. Bobrovnikov[120a,120b],   S. S. Bocchetta[94],   A. Bocci[47],   D. Boerner[179],   D. Bogavac[112],   A. G. Bogdanchikov[120a,120b],
C. Bohm[43a],   V. Boisvert[91],   P. Bokan[169,w],   T. Bold[81a],   A. S. Boldyrev[111],   A. E. Bolz[59b],   M. Bomben[132],   M. Bona[90],
J. S. Bonilla[127],   M. Boonekamp[142],   A. Borisov[140],   G. Borissov[87],   J. Bortfeldt[35],   D. Bortoletto[131],   V. Bortolotto[71a,71b],
D. Boscherini[23b],   M. Bosman[14],   J. D. Bossio Sola[30],   K. Bouaouda[34a],   J. Boudreau[135],   E. V. Bouhova-Thacker[87],
D. Boumediene[37],   C. Bourdarios[128],   S. K. Boutle[55],   A. Boveia[122],   J. Boyd[35],   D. Boye[32b],   I. R. Boyko[77],   A. J. Bozson[91],
J. Bracinik[21],   N. Brahimi[99],   A. Brandt[8],   G. Brandt[179],   O. Brandt[59a],   F. Braren[44],   U. Bratzler[161],   B. Brau[100],
J. E. Brau[127],   W. D. Breaden Madden[55],   K. Brendlinger[44],   L. Brenner[44],   R. Brenner[169],   S. Bressler[177],   B. Brickwedde[97],
D. L. Briglin[21],   D. Britton[55],   D. Britzger[59b],   I. Brock[24],   R. Brock[104],   G. Brooijmans[38],   T. Brooks[91],   W. K. Brooks[144b],
E. Brost[119],   J. H Broughton[21],   P. A. Bruckman de Renstrom[82],   D. Bruncko[28b],   A. Bruni[23b],   G. Bruni[23b],   L. S. Bruni[118],
S. Bruno[71a,71b],   B.H. Brunt[31],   M. Bruschi[23b],   N. Bruscino[135],   P. Bryant[36],   L. Bryngemark[44],   T. Buanes[17],   Q. Buat[35],
P. Buchholz[148],   A. G. Buckley[55],   I. A. Budagov[77],   F. Buehrer[50],   M. K. Bugge[130],   O. Bulekov[110],   D. Bullock[8],
T. J. Burch[119],   S. Burdin[88],   C. D. Burgard[118],   A. M. Burger[5],   B. Burghgrave[119],   K. Burka[82],   S. Burke[141],   I. Burmeister[45],
J. T. P. Burr[131],   V. Büscher[97],   E. Buschmann[51],   P. Bussey[55],   J. M. Butler[25],   C. M. Buttar[55],   J. M. Butterworth[92],   P. Butti[35],
W. Buttinger[35],   A. Buzatu[155],   A. R. Buzykaev[120a,120b],   G. Cabras[23a,23b],   S. Cabrera Urbán[171],   D. Caforio[138],   H. Cai[170],
V. M. M. Cairo[2],   O. Cakir[4a],   N. Calace[52],   P. Calafiura[18],   A. Calandri[99],   G. Calderini[132],   P. Calfayan[63],   G. Callea[40a,40b],
L. P. Caloba[78b],   S. Calvente Lopez[96],   D. Calvet[37],   S. Calvet[37],   T. P. Calvet[152],   M. Calvetti[69a,69b],   R. Camacho Toro[132],
S. Camarda[35],   P. Camarri[71a,71b],   D. Cameron[130],   R. Caminal Armadans[100],   C. Camincher[35],   S. Campana[35],
M. Campanelli[92],   A. Camplani[39],   A. Campoverde[148],   V. Canale[67a,67b],   M. Cano Bret[58c],   J. Cantero[125],   T. Cao[158],
Y. Cao[170],   M. D. M. Capeans Garrido[35],   I. Caprini[27b],   M. Caprini[27b],   M. Capua[40a,40b],   R. M. Carbone[38],   R. Cardarelli[71a],
F. C. Cardillo[146],   I. Carli[139],   T. Carli[35],   G. Carlino[67a],   B. T. Carlson[135],   L. Carminati[66a,66b],   R. M. D. Carney[43a,43b],
S. Caron[117],   E. Carquin[144b],   S. Carrá[66a,66b],   G. D. Carrillo-Montoya[35],   D. Casadei[32b],   M. P. Casado[14,f],   A. F. Casha[164],
D. W. Casper[168],   R. Castelijn[118],   F. L. Castillo[171],   V. Castillo Gimenez[171],   N. F. Castro[136a,136e],   A. Catinaccio[35],
J. R. Catmore[130],   A. Cattai[35],   J. Caudron[24],   V. Cavaliere[29],   E. Cavallaro[14],   D. Cavalli[66a],   M. Cavalli-Sforza[14],
V. Cavasinni[69a,69b],   E. Celebi[12b],   F. Ceradini[72a,72b],   L. Cerda Alberich[171],   A. S. Cerqueira[78a],   A. Cerri[153],   L. Cerrito[71a,71b],
F. Cerutti[18],   A. Cervelli[23a,23b],   S. A. Cetin[12b],   A. Chafaq[34a],   D Chakraborty[119],   S. K. Chan[57],   W. S. Chan[118],
Y. L. Chan[61a],   J. D. Chapman[31],   B. Chargeishvili[156b],   D. G. Charlton[21],   C. C. Chau[33],   C. A. Chavez Barajas[153],
S. Che[122],   A. Chegwidden[104],   S. Chekanov[6],   S. V. Chekulaev[165a],   G. A. Chelkov[77,ap],   M. A. Chelstowska[35],
C. Chen[58a],   C. H. Chen[76],   H. Chen[29],   J. Chen[58a],   J. Chen[38],   S. Chen[133],   S. J. Chen[15c],   X. Chen[15b,ao],   Y. Chen[80],
Y-H. Chen[44],   H. C. Cheng[103],   H. J. Cheng[15d],   A. Cheplakov[77],   E. Cheremushkina[140],   R. Cherkaoui El Moursli[34e],
E. Cheu[7],   K. Cheung[62],   L. Chevalier[142],   V. Chiarella[49],   G. Chiarelli[69a],   G. Chiodini[65a],   A. S. Chisholm[35,21],
A. Chitan[27b],   I. Chiu[160],   Y. H. Chiu[173],   M. V. Chizhov[77],   K. Choi[63],   A. R. Chomont[128],   S. Chouridou[159],   Y. S. Chow[118],
V. Christodoulou[92],   M. C. Chu[61a],   J. Chudoba[137],   A. J. Chuinard[101],   J. J. Chwastowski[82],   L. Chytka[126],   D. Cinca[45],
V. Cindro[89],   I. A. Cioară[24],   A. Ciocio[18],   F. Cirotto[67a,67b],   Z. H. Citron[177],   M. Citterio[66a],   A. Clark[52],   M. R. Clark[38],
P. J. Clark[48],   C. Clement[43a,43b],   Y. Coadou[99],   M. Cobal[64a,64c],   A. Coccaro[53a,53b],   J. Cochran[76],   H. Cohen[158],
A. E. C. Coimbra[177],   L. Colasurdo[117],   B. Cole[38],   A. P. Colijn[118],   J. Collot[56],   P. Conde Muiño[136a,136b],   E. Coniavitis[50],
S. H. Connell[32b],   I. A. Connelly[98],   S. Constantinescu[27b],   F. Conventi[67a,ar],   A. M. Cooper-Sarkar[131],   F. Cormier[172],
K. J. R. Cormier[164],   L. D. Corpe[92],   M. Corradi[70a,70b],   E. E. Corrigan[94],   F. Corriveau[101,ab],   A. Cortes-Gonzalez[35],
M. J. Costa[171],   F. Costanza[5],   D. Costanzo[146],   G. Cottin[31],   G. Cowan[91],   B. E. Cox[98],   J. Crane[98],   K. Cranmer[121],
S. J. Crawley[55],   R. A. Creager[133],   G. Cree[33],   S. Crépé-Renaudin[56],   F. Crescioli[132],   M. Cristinziani[24],   V. Croft[121],
G. Crosetti[40a,40b],   A. Cueto[96],   T. Cuhadar Donszelmann[146],   A. R. Cukierman[150],   S. Czekierda[82],   P. Czodrowski[35],
M. J. Da Cunha Sargedas De Sousa[58b,136b],   C. Da Via[98],   W. Dabrowski[81a],   T. Dado[28a,w],   S. Dahbi[34e],   T. Dai[103],
F. Dallaire[107],   C. Dallapiccola[100],   M. Dam[39],   G. D'amen[23a,23b],   J. Damp[97],   J. R. Dandoy[133],   M. F. Daneri[30],
N. P. Dang[178,j],   N. D Dann[98],   M. Danninger[172],   V. Dao[35],   G. Darbo[53b],   S. Darmora[8],   O. Dartsi[5],   A. Dattagupta[127],
T. Daubney[44],   S. D'Auria[55],   W. Davey[24],   C. David[44],   T. Davidek[139],   D. R. Davis[47],   E. Dawe[102],   I. Dawson[146],   K. De[8],
R. De Asmundis[67a],   A. De Benedetti[124],   M. De Beurs[118],   S. De Castro[23a,23b],   S. De Cecco[70a,70b],   N. De Groot[117],
P. de Jong[118],   H. De la Torre[104],   F. De Lorenzi[76],   A. De Maria[51,r],   D. De Pedis[70a],   A. De Salvo[70a],   U. De Sanctis[71a,71b],

M. De Santis[71a,71b], A. De Santo[153], K. De Vasconcelos Corga[99], J. B. De Vivie De Regie[128], C. Debenedetti[143], D. V. Dedovich[77], N. Dehghanian[3], M. Del Gaudio[40a,40b], J. Del Peso[96], Y. Delabat Diaz[44], D. Delgove[128], F. Deliot[142], C. M. Delitzsch[7], M. Della Pietra[67a,67b], D. Della Volpe[52], A. Dell'Acqua[35], L. Dell'Asta[25], M. Delmastro[5], C. Delporte[128], P. A. Delsart[56], D. A. DeMarco[164], S. Demers[180], M. Demichev[77], S. P. Denisov[140], D. Denysiuk[118], L. D'Eramo[132], D. Derendarz[82], J. E. Derkaoui[34d], F. Derue[132], P. Dervan[88], K. Desch[24], C. Deterre[44], K. Dette[164], M. R. Devesa[30], P. O. Deviveiros[35], A. Dewhurst[141], S. Dhaliwal[26], F. A. Di Bello[52], A. Di Ciaccio[71a,71b], L. Di Ciaccio[5], W. K. Di Clemente[133], C. Di Donato[67a,67b], A. Di Girolamo[35], G. Di Gregorio[69a,69b], B. Di Micco[72a,72b], R. Di Nardo[100], K. F. Di Petrillo[57], R. Di Sipio[164], D. Di Valentino[33], C. Diaconu[99], M. Diamond[164], F. A. Dias[39], T. Dias Do Vale[136a], M. A. Diaz[144a], J. Dickinson[18], E. B. Diehl[103], J. Dietrich[19], S. Díez Cornell[44], A. Dimitrievska[18], J. Dingfelder[24], F. Dittus[35], F. Djama[99], T. Djobava[156b], J. I. Djuvsland[59a], M. A. B. Do Vale[78c], M. Dobre[27b], D. Dodsworth[26], C. Doglioni[94], J. Dolejsi[139], Z. Dolezal[139], M. Donadelli[78d], J. Donini[37], A. D'onofrio[90], M. D'Onofrio[88], J. Dopke[141], A. Doria[67a], M. T. Dova[86], A. T. Doyle[55], E. Drechsler[51], E. Dreyer[149], T. Dreyer[51], Y. Du[58b], F. Dubinin[108], M. Dubovsky[28a], A. Dubreuil[52], E. Duchovni[177], G. Duckeck[112], A. Ducourthial[132], O. A. Ducu[107,v], D. Duda[113], A. Dudarev[35], A. C. Dudder[97], E. M. Duffield[18], L. Duflot[128], M. Dührssen[35], C. Dülsen[179], M. Dumancic[177], A. E. Dumitriu[27b,d], A. K. Duncan[55], M. Dunford[59a], A. Duperrin[99], H. Duran Yildiz[4a], M. Düren[54], A. Durglishvili[156b], D. Duschinger[46], B. Dutta[44], D. Duvnjak[1], S. Dysch[98], B. S. Dziedzic[82], C. Eckardt[44], K. M. Ecker[113], R. C. Edgar[103], T. Eifert[35], G. Eigen[17], K. Einsweiler[18], T. Ekelof[169], M. El Kacimi[34c], R. El Kosseifi[99], V. Ellajosyula[99], M. Ellert[169], F. Ellinghaus[179], A. A. Elliot[90], N. Ellis[35], J. Elmsheuser[29], M. Elsing[35], D. Emeliyanov[141], Y. Enari[160], J. S. Ennis[175], M. B. Epland[47], J. Erdmann[45], A. Ereditato[20], S. Errede[170], M. Escalier[128], C. Escobar[171], O. Estrada Pastor[171], A. I. Etienvre[142], E. Etzion[158], H. Evans[63], A. Ezhilov[134], M. Ezzi[34e], F. Fabbri[55], L. Fabbri[23a,23b], V. Fabiani[117], G. Facini[92], R. M. Faisca Rodrigues Pereira[136a], R. M. Fakhrutdinov[140], S. Falciano[70a], P. J. Falke[5], S. Falke[5], J. Faltova[139], Y. Fang[15a], M. Fanti[66a,66b], A. Farbin[8], A. Farilla[72a], E. M. Farina[68a,68b], T. Farooque[104], S. Farrell[18], S. M. Farrington[175], P. Farthouat[35], F. Fassi[34e], P. Fassnacht[35], D. Fassouliotis[9], M. Faucci Giannelli[48], A. Favareto[53a,53b], W. J. Fawcett[31], L. Fayard[128], O. L. Fedin[134,o], W. Fedorko[172], M. Feickert[41], S. Feigl[130], L. Feligioni[99], C. Feng[58b], E. J. Feng[35], M. Feng[47], M. J. Fenton[55], A. B. Fenyuk[140], L. Feremenga[8], J. Ferrando[44], A. Ferrari[169], P. Ferrari[118], R. Ferrari[68a], D. E. Ferreira de Lima[59b], A. Ferrer[171], D. Ferrere[52], C. Ferretti[103], F. Fiedler[97], A. Filipčič[89], F. Filthaut[117], K. D. Finelli[25], M. C. N. Fiolhais[136a,136c,a], L. Fiorini[171], C. Fischer[14], W. C. Fisher[104], N. Flaschel[44], I. Fleck[148], P. Fleischmann[103], R. R. M. Fletcher[133], T. Flick[179], B. M. Flierl[112], L. M. Flores[133], L. R. Flores Castillo[61a], F. M. Follega[73a,73b], N. Fomin[17], G. T. Forcolin[73a,73b], A. Formica[142], F. A. Förster[14], A. C. Forti[98], A. G. Foster[21], D. Fournier[128], H. Fox[87], S. Fracchia[146], P. Francavilla[69a,69b], M. Franchini[23a,23b], S. Franchino[59a], D. Francis[35], L. Franconi[143], M. Franklin[57], M. Frate[168], M. Fraternali[68a,68b], A. N. Fray[90], D. Freeborn[92], S. M. Fressard-Batraneanu[35], B. Freund[107], W. S. Freund[78b], E. M. Freundlich[45], D. C. Frizzell[124], D. Froidevaux[35], J. A. Frost[131], C. Fukunaga[161], E. Fullana Torregrosa[171], T. Fusayasu[114], J. Fuster[171], O. Gabizon[157], A. Gabrielli[23a,23b], A. Gabrielli[18], G. P. Gach[81a], S. Gadatsch[52], P. Gadow[113], G. Gagliardi[53a,53b], L. G. Gagnon[107], C. Galea[27b], B. Galhardo[136a,136c], E. J. Gallas[131], B. J. Gallop[141], P. Gallus[138], G. Galster[39], R. Gamboa Goni[90], K. K. Gan[122], S. Ganguly[177], J. Gao[58a], Y. Gao[88], Y. S. Gao[150,l], C. García[171], J. E. García Navarro[171], J. A. García Pascual[15a], M. Garcia-Sciveres[18], R. W. Gardner[36], N. Garelli[150], V. Garonne[130], K. Gasnikova[44], A. Gaudiello[53a,53b], G. Gaudio[68a], I. L. Gavrilenko[108], A. Gavrilyuk[109], C. Gay[172], G. Gaycken[24], E. N. Gazis[10], C. N. P. Gee[141], J. Geisen[51], M. Geisen[97], M. P. Geisler[59a], K. Gellerstedt[43a,43b], C. Gemme[53b], M. H. Genest[56], C. Geng[103], S. Gentile[70a,70b], S. George[91], D. Gerbaudo[14], G. Gessner[45], S. Ghasemi[148], M. Ghasemi Bostanabad[173], M. Ghneimat[24], B. Giacobbe[23b], S. Giagu[70a,70b], N. Giangiacomi[23a,23b], P. Giannetti[69a], A. Giannini[67a,67b], S. M. Gibson[91], M. Gignac[143], D. Gillberg[33], G. Gilles[179], D. M. Gingrich[3,aq], M. P. Giordani[64a,64c], F. M. Giorgi[23b], P. F. Giraud[142], P. Giromini[57], G. Giugliarelli[64a,64c], D. Giugni[66a], F. Giuli[131], M. Giulini[59b], S. Gkaitatzis[159], I. Gkialas[9,i], E. L. Gkougkousis[14], P. Gkountoumis[10], L. K. Gladilin[111], C. Glasman[96], J. Glatzer[14], P. C. F. Glaysher[44], A. Glazov[44], M. Goblirsch-Kolb[26], J. Godlewski[82], S. Goldfarb[102], T. Golling[52], D. Golubkov[140], A. Gomes[136a,136b,136d], R. Goncalves Gama[78a], R. Gonçalo[136a], G. Gonella[50], L. Gonella[21], A. Gongadze[77], F. Gonnella[21], J. L. Gonski[57], S. González de la Hoz[171], S. Gonzalez-Sevilla[52], L. Goossens[35], P. A. Gorbounov[109], H. A. Gordon[29], B. Gorini[35], E. Gorini[65a,65b], A. Gorišek[89], A. T. Goshaw[47], C. Gössling[45], M. I. Gostkin[77], C. A. Gottardo[24], C. R. Goudet[128], D. Goujdami[34c], A. G. Goussiou[145], N. Govender[32b,b], C. Goy[5], E. Gozani[157], I. Grabowska-Bold[81a], P. O. J. Gradin[169], E. C. Graham[88], J. Gramling[168], E. Gramstad[130], S. Grancagnolo[19], V. Gratchev[134], P. M. Gravila[27f], F. G. Gravili[65a,65b], C. Gray[55], H. M. Gray[18], Z. D. Greenwood[93,ah], C. Grefe[24], K. Gregersen[94], I. M. Gregor[44], P. Grenier[150], K. Grevtsov[44], N. A. Grieser[124], J. Griffiths[8], A. A. Grillo[143], K. Grimm[150], S. Grinstein[14,x], Ph. Gris[37], J.-F. Grivaz[128], S. Groh[97], E. Gross[177], J. Grosse-Knetter[51], G. C. Grossi[93], Z. J. Grout[92], C. Grud[103], A. Grummer[116], L. Guan[103], W. Guan[178], J. Guenther[35], A. Guerguichon[128], F. Guescini[165a], D. Guest[168], R. Gugel[50], B. Gui[122],

T. Guillemin[5], S. Guindon[35], U. Gul[55], C. Gumpert[35], J. Guo[58c], W. Guo[103], Y. Guo[58a,q], Z. Guo[99], R. Gupta[41], S. Gurbuz[12c], G. Gustavino[124], B. J. Gutelman[157], P. Gutierrez[124], C. Gutschow[92], C. Guyot[142], M. P. Guzik[81a], C. Gwenlan[131], C. B. Gwilliam[88], A. Haas[121], C. Haber[18], H. K. Hadavand[8], N. Haddad[34e], A. Hadef[58a], S. Hageböck[24], M. Hagihara[166], H. Hakobyan[181,*], M. Haleem[174], J. Haley[125], G. Halladjian[104], G. D. Hallewell[99], K. Hamacher[179], P. Hamal[126], K. Hamano[173], A. Hamilton[32a], G. N. Hamity[146], K. Han[58a,ag], L. Han[58a], S. Han[15d], K. Hanagaki[79,t], M. Hance[143], D. M. Handl[112], B. Haney[134], R. Hankache[132], P. Hanke[59a], E. Hansen[94], J. B. Hansen[39], J. D. Hansen[39], M. C. Hansen[24], P. H. Hansen[39], K. Hara[166], A. S. Hard[178], T. Harenberg[179], S. Harkusha[105], P. F. Harrison[175], N. M. Hartmann[112], Y. Hasegawa[147], A. Hasib[48], S. Hassani[142], S. Haug[20], R. Hauser[104], L. Hauswald[46], L. B. Havener[38], M. Havranek[138], C. M. Hawkes[21], R. J. Hawkings[35], D. Hayden[104], C. Hayes[152], C. P. Hays[131], J. M. Hays[90], H. S. Hayward[88], S. J. Haywood[141], M. P. Heath[48], V. Hedberg[94], L. Heelan[8], S. Heer[24], K. K. Heidegger[50], J. Heilman[33], S. Heim[44], T. Heim[18], B. Heinemann[44,al], J. J. Heinrich[112], L. Heinrich[121], C. Heinz[54], J. Hejbal[137], L. Helary[35], A. Held[172], S. Hellesund[130], S. Hellman[43a,43b], C. Helsens[35], R. C. W. Henderson[87], Y. Heng[178], S. Henkelmann[172], A. M. Henriques Correia[35], G. H. Herbert[19], H. Herde[26], V. Herget[174], Y. Hernández Jiménez[32c], H. Herr[97], M. G. Herrmann[112], G. Herten[50], R. Hertenberger[112], L. Hervas[35], T. C. Herwig[133], G. G. Hesketh[92], N. P. Hessey[165a], J. W. Hetherly[41], S. Higashino[79], E. Higón-Rodriguez[171], K. Hildebrand[36], E. Hill[173], J. C. Hill[31], K. K. Hill[29], K. H. Hiller[44], S. J. Hillier[21], M. Hils[46], I. Hinchliffe[18], M. Hirose[129], D. Hirschbuehl[179], B. Hiti[89], O. Hladik[137], D. R. Hlaluku[32c], X. Hoad[48], J. Hobbs[152], N. Hod[165a], M. C. Hodgkinson[146], A. Hoecker[35], M. R. Hoeferkamp[116], F. Hoenig[112], D. Hohn[24], D. Hohov[128], T. R. Holmes[36], M. Holzbock[112], M. Homann[45], S. Honda[166], T. Honda[79], T. M. Hong[135], A. Hönle[113], B. H. Hooberman[170], W. H. Hopkins[127], Y. Horii[115], P. Horn[46], A. J. Horton[149], L. A. Horyn[36], J-Y. Hostachy[56], A. Hostiuc[145], S. Hou[155], A. Hoummada[34a], J. Howarth[98], J. Hoya[86], M. Hrabovsky[126], I. Hristova[19], J. Hrivnac[128], A. Hrynevich[106], T. Hryn'ova[5], P. J. Hsu[62], S.-C. Hsu[145], Q. Hu[29], S. Hu[58c], Y. Huang[15a], Z. Hubacek[138], F. Hubaut[99], M. Huebner[24], F. Huegging[24], T. B. Huffman[131], E. W. Hughes[38], M. Huhtinen[35], R. F. H. Hunter[33], P. Huo[152], A. M. Hupe[33], N. Huseynov[77,ad], J. Huston[104], J. Huth[57], R. Hyneman[103], G. Iacobucci[52], G. Iakovidis[29], I. Ibragimov[148], L. Iconomidou-Fayard[128], Z. Idrissi[34e], P. Iengo[35], R. Ignazzi[39], O. Igonkina[118,z], R. Iguchi[160], T. Iizawa[52], Y. Ikegami[79], M. Ikeno[79], D. Iliadis[159], N. Ilic[150], F. Iltzsche[46], G. Introzzi[68a,68b], M. Iodice[72a], K. Iordanidou[38], V. Ippolito[70a,70b], M. F. Isacson[169], N. Ishijima[129], M. Ishino[160], M. Ishitsuka[162], W. Islam[125], C. Issever[131], S. Istin[157], F. Ito[166], J. M. Iturbe Ponce[61a], R. Iuppa[73a,73b], A. Ivina[177], H. Iwasaki[79], J. M. Izen[42], V. Izzo[67a], P. Jacka[137], P. Jackson[1], R. M. Jacobs[24], V. Jain[2], G. Jäkel[179], K. B. Jakobi[97], K. Jakobs[50], S. Jakobsen[74], T. Jakoubek[137], D. O. Jamin[125], D. K. Jana[93], R. Jansky[52], J. Janssen[24], M. Janus[51], P. A. Janus[81a], G. Jarlskog[94], N. Javadov[77,ad], T. Javůrek[35], M. Javurkova[50], F. Jeanneau[142], L. Jeanty[18], J. Jejelava[156a,ae], A. Jelinskas[175], P. Jenni[50,c], J. Jeong[44], N. Jeong[44], S. Jézéquel[5], H. Ji[178], J. Jia[152], H. Jiang[76], Y. Jiang[58a], Z. Jiang[150], S. Jiggins[50], F. A. Jimenez Morales[37], J. Jimenez Pena[171], S. Jin[15c], A. Jinaru[27b], O. Jinnouchi[162], H. Jivan[32c], P. Johansson[146], K. A. Johns[7], C. A. Johnson[63], W. J. Johnson[145], K. Jon-And[43a,43b], R. W. L. Jones[87], S. D. Jones[153], S. Jones[7], T. J. Jones[88], J. Jongmanns[59a], P. M. Jorge[136a,136b], J. Jovicevic[165a], X. Ju[18], J. J. Junggeburth[113], A. Juste Rozas[14,x], A. Kaczmarska[82], M. Kado[128], H. Kagan[122], M. Kagan[150], T. Kaji[176], E. Kajomovitz[157], C. W. Kalderon[94], A. Kaluza[97], S. Kama[41], A. Kamenshchikov[140], L. Kanjir[89], Y. Kano[160], V. A. Kantserov[110], J. Kanzaki[79], B. Kaplan[121], L. S. Kaplan[178], D. Kar[32c], M. J. Kareem[165b], E. Karentzos[10], S. N. Karpov[77], Z. M. Karpova[77], V. Kartvelishvili[87], A. N. Karyukhin[140], L. Kashif[178], R. D. Kass[122], A. Kastanas[43a,43b], Y. Kataoka[160], C. Kato[58c,58d], J. Katzy[44], K. Kawade[80], K. Kawagoe[85], T. Kawamoto[160], G. Kawamura[51], E. F. Kay[88], V. F. Kazanin[120a,120b], R. Keeler[173], R. Kehoe[41], J. S. Keller[33], E. Kellermann[94], J. J. Kempster[21], J. Kendrick[21], O. Kepka[137], S. Kersten[179], B. P. Kerševan[89], R. A. Keyes[101], M. Khader[170], F. Khalil-Zada[13], A. Khanov[125], A. G. Kharlamov[120a,120b], T. Kharlamova[120a,120b], E. E. Khoda[172], A. Khodinov[163], T. J. Khoo[52], E. Khramov[77], J. Khubua[156b], S. Kido[80], M. Kiehn[52], C. R. Kilby[91], Y. K. Kim[36], N. Kimura[64a,64c], O. M. Kind[19], B. T. King[88], D. Kirchmeier[46], J. Kirk[141], A. E. Kiryunin[113], T. Kishimoto[160], D. Kisielewska[81a], V. Kitali[44], O. Kivernyk[5], E. Kladiva[28b], T. Klapdor-Kleingrothaus[50], M. H. Klein[103], M. Klein[88], U. Klein[88], K. Kleinknecht[97], P. Klimek[119], A. Klimentov[29], T. Klingl[24], T. Klioutchnikova[35], F. F. Klitzner[112], P. Kluit[118], S. Kluth[113], E. Kneringer[74], E. B. F. G. Knoops[99], A. Knue[50], A. Kobayashi[160], D. Kobayashi[85], T. Kobayashi[160], M. Kobel[46], M. Kocian[150], P. Kodys[139], P. T. Koenig[24], T. Koffas[33], E. Koffeman[118], N. M. Köhler[113], T. Koi[150], M. Kolb[59b], I. Koletsou[5], T. Kondo[79], N. Kondrashova[58c], K. Köneke[50], A. C. König[117], T. Kono[79], R. Konoplich[121,ai], V. Konstantinides[92], N. Konstantinidis[92], B. Konya[94], R. Kopeliansky[63], S. Koperny[81a], K. Korcyl[82], K. Kordas[159], G. Koren[158], A. Korn[92], I. Korolkov[14], E. V. Korolkova[146], N. Korotkova[111], O. Kortner[113], S. Kortner[113], T. Kosek[139], V. V. Kostyukhin[24], A. Kotwal[47], A. Koulouris[10], A. Kourkoumeli-Charalampidi[68a,68b], C. Kourkoumelis[9], E. Kourlitis[146], V. Kouskoura[29], A. B. Kowalewska[82], R. Kowalewski[173], T. Z. Kowalski[81a], C. Kozakai[160], W. Kozanecki[142], A. S. Kozhin[140], V. A. Kramarenko[111], G. Kramberger[89], D. Krasnopevtsev[58a], M. W. Krasny[132], A. Krasznahorkay[35],

D. Krauss[113], J. A. Kremer[81a], J. Kretzschmar[88], P. Krieger[164], K. Krizka[18], K. Kroeninger[45], H. Kroha[113], J. Kroll[137], J. Kroll[133], J. Krstic[16], U. Kruchonak[77], H. Krüger[24], N. Krumnack[76], M. C. Kruse[47], T. Kubota[102], S. Kuday[4b], J. T. Kuechler[179], S. Kuehn[35], A. Kugel[59a], F. Kuger[174], T. Kuhl[44], V. Kukhtin[77], R. Kukla[99], Y. Kulchitsky[105], S. Kuleshov[144b], Y. P. Kulinich[170], M. Kuna[56], T. Kunigo[83], A. Kupco[137], T. Kupfer[45], O. Kuprash[158], H. Kurashige[80], L. L. Kurchaninov[165a], Y. A. Kurochkin[105], M. G. Kurth[15d], E. S. Kuwertz[35], M. Kuze[162], J. Kvita[126], T. Kwan[101], A. La Rosa[113], J. L. La Rosa Navarro[78d], L. La Rotonda[40a,40b], F. La Ruffa[40a,40b], C. Lacasta[171], F. Lacava[70a,70b], J. Lacey[44], D. P. J. Lack[98], H. Lacker[19], D. Lacour[132], E. Ladygin[77], R. Lafaye[5], B. Laforge[132], T. Lagouri[32c], S. Lai[51], S. Lammers[63], W. Lampl[7], E. Lançon[29], U. Landgraf[50], M. P. J. Landon[90], M. C. Lanfermann[52], V. S. Lang[44], J. C. Lange[14], R. J. Langenberg[35], A. J. Lankford[168], F. Lanni[29], K. Lantzsch[24], A. Lanza[68a], A. Lapertosa[53a,53b], S. Laplace[132], J. F. Laporte[142], T. Lari[66a], F. Lasagni Manghi[23a,23b], M. Lassnig[35], T. S. Lau[61a], A. Laudrain[128], M. Lavorgna[67a,67b], A. T. Law[143], M. Lazzaroni[66a,66b], B. Le[102], O. Le Dortz[132], E. Le Guirriec[99], E. P. Le Quilleuc[142], M. LeBlanc[7], T. LeCompte[6], F. Ledroit-Guillon[56], C. A. Lee[29], G. R. Lee[144a], L. Lee[57], S. C. Lee[155], B. Lefebvre[101], M. Lefebvre[173], F. Legger[112], C. Leggett[18], K. Lehmann[149], N. Lehmann[179], G. Lehmann Miotto[35], W. A. Leight[44], A. Leisos[159,u], M. A. L. Leite[78d], R. Leitner[139], D. Lellouch[177], B. Lemmer[51], K. J. C. Leney[92], T. Lenz[24], B. Lenzi[35], R. Leone[7], S. Leone[69a], C. Leonidopoulos[48], G. Lerner[153], C. Leroy[107], R. Les[164], A. A. J. Lesage[142], C. G. Lester[31], M. Levchenko[134], J. Levêque[5], D. Levin[103], L. J. Levinson[177], D. Lewis[90], B. Li[103], C-Q. Li[58a], H. Li[58b], L. Li[58c], M. Li[15a], Q. Li[15d], Q. Y. Li[58a], S. Li[58c,58d], X. Li[58c], Y. Li[148], Z. Liang[15a], B. Liberti[71a], A. Liblong[164], K. Lie[61c], S. Liem[118], A. Limosani[154], C. Y. Lin[31], K. Lin[104], T. H. Lin[97], R. A. Linck[63], J. H. Lindon[21], B. E. Lindquist[152], A. L. Lionti[52], E. Lipeles[133], A. Lipniacka[17], M. Lisovyi[59b], T. M. Liss[170,an], A. Lister[172], A. M. Litke[143], J. D. Little[8], B. Liu[76], B. L Liu[6], H. B. Liu[29], H. Liu[103], J. B. Liu[58a], J. K. K. Liu[131], K. Liu[132], M. Liu[58a], P. Liu[18], Y. Liu[15a], Y. L. Liu[58a], Y. W. Liu[58a], M. Livan[68a,68b], A. Lleres[56], J. Llorente Merino[15a], S. L. Lloyd[90], C. Y. Lo[61b], F. Lo Sterzo[41], E. M. Lobodzinska[44], P. Loch[7], A. Loesle[50], T. Lohse[19], K. Lohwasser[146], M. Lokajicek[137], B. A. Long[25], J. D. Long[170], R. E. Long[87], L. Longo[65a,65b], K. A. Looper[122], J. A. Lopez[144b], I. Lopez Paz[14], A. Lopez Solis[146], J. Lorenz[112], N. Lorenzo Martinez[5], M. Losada[22], P. J. Lösel[112], X. Lou[44], X. Lou[15a], A. Lounis[128], J. Love[6], P. A. Love[87], J. J. Lozano Bahilo[171], H. Lu[61a], M. Lu[58a], N. Lu[103], Y. J. Lu[62], H. J. Lubatti[145], C. Luci[70a,70b], A. Lucotte[56], C. Luedtke[50], F. Luehring[63], I. Luise[132], L. Luminari[70a], B. Lund-Jensen[151], M. S. Lutz[100], P. M. Luzi[132], D. Lynn[29], R. Lysak[137], E. Lytken[94], F. Lyu[15a], V. Lyubushkin[77], H. Ma[29], L. L. Ma[58b], Y. Ma[58b], G. Maccarrone[49], A. Macchiolo[113], C. M. Macdonald[146], J. Machado Miguens[133,136b], D. Madaffari[171], R. Madar[37], W. F. Mader[46], A. Madsen[44], N. Madysa[46], J. Maeda[80], K. Maekawa[160], S. Maeland[17], T. Maeno[29], A. S. Maevskiy[111], V. Magerl[50], C. Maidantchik[78b], T. Maier[112], A. Maio[136a,136b,136d], O. Majersky[28a], S. Majewski[127], Y. Makida[79], N. Makovec[128], B. Malaescu[132], Pa. Malecki[82], V. P. Maleev[134], F. Malek[56], U. Mallik[75], D. Malon[6], C. Malone[31], S. Maltezos[10], S. Malyukov[35], J. Mamuzic[171], G. Mancini[49], I. Mandić[89], J. Maneira[136a], L. Manhaes de Andrade Filho[78a], J. Manjarres Ramos[46], K. H. Mankinen[94], A. Mann[112], A. Manousos[74], B. Mansoulie[142], J. D. Mansour[15a], M. Mantoani[51], S. Manzoni[66a,66b], A. Marantis[159], G. Marceca[30], L. March[52], L. Marchese[131], G. Marchiori[132], M. Marcisovsky[137], C. A. Marin Tobon[35], M. Marjanovic[37], D. E. Marley[103], F. Marroquim[78b], Z. Marshall[18], M. U. F Martensson[169], S. Marti-Garcia[171], C. B. Martin[122], T. A. Martin[175], V. J. Martin[48], B. Martin dit Latour[17], M. Martinez[14,x], V. I. Martinez Outschoorn[100], S. Martin-Haugh[141], V. S. Martoiu[27b], A. C. Martyniuk[92], A. Marzin[35], L. Masetti[97], T. Mashimo[160], R. Mashinistov[108], J. Masik[98], A. L. Maslennikov[120a,120b], L. H. Mason[102], L. Massa[71a,71b], P. Massarotti[67a,67b], P. Mastrandrea[5], A. Mastroberardino[40a,40b], T. Masubuchi[160], P. Mättig[179], J. Maurer[27b], B. Maček[89], S. J. Maxfield[88], D. A. Maximov[120a,120b], R. Mazini[155], I. Maznas[159], S. M. Mazza[143], N. C. Mc Fadden[116], G. Mc Goldrick[164], S. P. Mc Kee[103], A. McCarn[103], T. G. McCarthy[113], L. I. McClymont[92], E. F. McDonald[102], J. A. Mcfayden[35], G. Mchedlidze[51], M. A. McKay[41], K. D. McLean[173], S. J. McMahon[141], P. C. McNamara[102], C. J. McNicol[175], R. A. McPherson[173,ab], J. E. Mdhluli[32c], Z. A. Meadows[100], S. Meehan[145], T. Megy[50], S. Mehlhase[112], A. Mehta[88], T. Meideck[56], B. Meirose[42], D. Melini[171,g], B. R. Mellado Garcia[32c], J. D. Mellenthin[51], M. Melo[28a], F. Meloni[44], A. Melzer[24], S. B. Menary[98], E. D. Mendes Gouveia[136a], L. Meng[88], X. T. Meng[103], A. Mengarelli[23a,23b], S. Menke[113], E. Meoni[40a,40b], S. Mergelmeyer[19], S. A. M. Merkt[135], C. Merlassino[20], P. Mermod[52], L. Merola[67a,67b], C. Meroni[66a], F. S. Merritt[36], A. Messina[70a,70b], J. Metcalfe[6], A. S. Mete[168], C. Meyer[133], J. Meyer[157], J-P. Meyer[142], H. Meyer Zu Theenhausen[59a], F. Miano[153], R. P. Middleton[141], L. Mijović[48], G. Mikenberg[177], M. Mikestikova[137], M. Mikuž[89], M. Milesi[102], A. Milic[164], D. A. Millar[90], D. W. Miller[36], A. Milov[177], D. A. Milstead[43a,43b], A. A. Minaenko[140], M. Miñano Moya[171], I. A. Minashvili[156b], A. I. Mincer[121], B. Mindur[81a], M. Mineev[77], Y. Minegishi[160], Y. Ming[178], L. M. Mir[14], A. Mirto[65a,65b], K. P. Mistry[133], T. Mitani[176], J. Mitrevski[112], V. A. Mitsou[171], A. Miucci[20], P. S. Miyagawa[146], A. Mizukami[79], J. U. Mjörnmark[94], T. Mkrtchyan[181], M. Mlynarikova[139], T. Moa[43a,43b], K. Mochizuki[107], P. Mogg[50], S. Mohapatra[38], S. Molander[43a,43b], R. Moles-Valls[24], M. C. Mondragon[104], K. Mönig[44], J. Monk[39], E. Monnier[99], A. Montalbano[149], J. Montejo Berlingen[35], F. Monticelli[86],

S. Monzani[66a], N. Morange[128], D. Moreno[22], M. Moreno Llácer[35], P. Morettini[53b], M. Morgenstern[118], S. Morgenstern[46], D. Mori[149], M. Morii[57], M. Morinaga[176], V. Morisbak[130], A. K. Morley[35], G. Mornacchi[35], A. P. Morris[92], J. D. Morris[90], L. Morvaj[152], P. Moschovakos[10], M. Mosidze[156b], H. J. Moss[146], J. Moss[150,m], K. Motohashi[162], R. Mount[150], E. Mountricha[35], E. J. W. Moyse[100], S. Muanza[99], F. Mueller[113], J. Mueller[135], R. S. P. Mueller[112], D. Muenstermann[87], G. A. Mullier[94], F. J. Munoz Sanchez[98], P. Murin[28b], W. J. Murray[175,141], A. Murrone[66a,66b], M. Muškinja[89], C. Mwewa[32a], A. G. Myagkov[140,aj], J. Myers[127], M. Myska[138], B. P. Nachman[18], O. Nackenhorst[45], K. Nagai[131], K. Nagano[79], Y. Nagasaka[60], M. Nagel[50], E. Nagy[99], A. M. Nairz[35], Y. Nakahama[115], K. Nakamura[79], T. Nakamura[160], I. Nakano[123], H. Nanjo[129], F. Napolitano[59a], R. F. Naranjo Garcia[44], R. Narayan[11], D. I. Narrias Villar[59a], I. Naryshkin[134], T. Naumann[44], G. Navarro[22], R. Nayyar[7], H. A. Neal[103], P. Y. Nechaeva[108], T. J. Neep[142], A. Negri[68a,68b], M. Negrini[23b], S. Nektarijevic[117], C. Nellist[51], M. E. Nelson[131], S. Nemecek[137], P. Nemethy[121], M. Nessi[35,e], M. S. Neubauer[170], M. Neumann[179], P. R. Newman[21], T. Y. Ng[61c], Y. S. Ng[19], H. D. N. Nguyen[99], T. Nguyen Manh[107], E. Nibigira[37], R. B. Nickerson[131], R. Nicolaidou[142], D. S. Nielsen[39], J. Nielsen[143], N. Nikiforou[11], V. Nikolaenko[140,aj], I. Nikolic-Audit[132], K. Nikolopoulos[21], P. Nilsson[29], Y. Ninomiya[79], A. Nisati[70a], N. Nishu[58c], R. Nisius[113], I. Nitsche[45], T. Nitta[176], T. Nobe[160], Y. Noguchi[83], M. Nomachi[129], I. Nomidis[132], M. A. Nomura[29], T. Nooney[90], M. Nordberg[35], N. Norjoharuddeen[131], T. Novak[89], O. Novgorodova[46], R. Novotny[138], L. Nozka[126], K. Ntekas[168], E. Nurse[92], F. Nuti[102], F. G. Oakham[33,aq], H. Oberlack[113], T. Obermann[24], J. Ocariz[132], A. Ochi[80], I. Ochoa[38], J. P. Ochoa-Ricoux[144a], K. O'Connor[26], S. Oda[85], S. Odaka[79], S. Oerdek[51], A. Oh[98], S. H. Oh[47], C. C. Ohm[151], H. Oide[53a,53b], M. L. Ojeda[164], H. Okawa[166], Y. Okazaki[83], Y. Okumura[160], T. Okuyama[79], A. Olariu[27b], L. F. Oleiro Seabra[136a], S. A. Olivares Pino[144a], D. Oliveira Damazio[29], J. L. Oliver[1], M. J. R. Olsson[36], A. Olszewski[82], J. Olszowska[82], D. C. O'Neil[149], A. Onofre[136a,136e], K. Onogi[115], P. U. E. Onyisi[11], H. Oppen[130], M. J. Oreglia[36], G. E. Orellana[86], Y. Oren[158], D. Orestano[72a,72b], E. C. Orgill[98], N. Orlando[61b], A. A. O'Rourke[44], R. S. Orr[164], B. Osculati[53a,53b,*], V. O'Shea[55], R. Ospanov[58a], G. Otero y Garzon[30], H. Otono[85], M. Ouchrif[34d], F. Ould-Saada[130], A. Ouraou[142], Q. Ouyang[15a], M. Owen[55], R. E. Owen[21], V. E. Ozcan[12c], N. Ozturk[8], J. Pacalt[126], H. A. Pacey[31], K. Pachal[149], A. Pacheco Pages[14], L. Pacheco Rodriguez[142], C. Padilla Aranda[14], S. Pagan Griso[18], M. Paganini[180], G. Palacino[63], S. Palazzo[40a,40b], S. Palestini[35], M. Palka[81b], D. Pallin[37], I. Panagoulias[10], C. E. Pandini[35], J. G. Panduro Vazquez[91], P. Pani[35], G. Panizzo[64a,64c], L. Paolozzi[52], T. D. Papadopoulou[10], K. Papageorgiou[9,i], A. Paramonov[6], D. Paredes Hernandez[61b], S. R. Paredes Saenz[131], B. Parida[163], A. J. Parker[87], K. A. Parker[44], M. A. Parker[31], F. Parodi[53a,53b], J. A. Parsons[38], U. Parzefall[50], V. R. Pascuzzi[164], J. M. P. Pasner[143], E. Pasqualucci[70a], S. Passaggio[53b], F. Pastore[91], P. Pasuwan[43a,43b], S. Pataraia[97], J. R. Pater[98], A. Pathak[178,j], T. Pauly[35], B. Pearson[113], M. Pedersen[130], L. Pedraza Diaz[117], R. Pedro[136a,136b], S. V. Peleganchuk[120a,120b], O. Penc[137], C. Peng[15d], H. Peng[58a], B. S. Peralva[78a], M. M. Perego[142], A. P. Pereira Peixoto[136a], D. V. Perepelitsa[29], F. Peri[19], L. Perini[66a,66b], H. Pernegger[35], S. Perrella[67a,67b], V. D. Peshekhonov[77,*], K. Peters[44], R. F. Y. Peters[98], B. A. Petersen[35], T. C. Petersen[39], E. Petit[56], A. Petridis[1], C. Petridou[159], P. Petroff[128], M. Petrov[131], F. Petrucci[72a,72b], M. Pettee[180], N. E. Pettersson[100], A. Peyaud[142], R. Pezoa[144b], T. Pham[102], F. H. Phillips[104], P. W. Phillips[141], M. W. Phipps[170], G. Piacquadio[152], E. Pianori[18], A. Picazio[100], M. A. Pickering[131], R. H. Pickles[98], R. Piegaia[30], J. E. Pilcher[36], A. D. Pilkington[98], M. Pinamonti[71a,71b], J. L. Pinfold[3], M. Pitt[177], L. Pizzimento[71a,71b], M-A. Pleier[29], V. Pleskot[139], E. Plotnikova[77], D. Pluth[76], P. Podberezko[120a,120b], R. Poettgen[94], R. Poggi[52], L. Poggioli[128], I. Pogrebnyak[104], D. Pohl[24], I. Pokharel[51], G. Polesello[68a], A. Poley[18], A. Policicchio[70a,70b], R. Polifka[35], A. Polini[23b], C. S. Pollard[44], V. Polychronakos[29], D. Ponomarenko[110], L. Pontecorvo[70a], G. A. Popeneciu[27d], D. M. Portillo Quintero[132], S. Pospisil[138], K. Potamianos[44], I. N. Potrap[77], C. J. Potter[31], H. Potti[11], T. Poulsen[94], J. Poveda[35], T. D. Powell[146], M. E. Pozo Astigarraga[35], P. Pralavorio[99], S. Prell[76], D. Price[98], M. Primavera[65a], S. Prince[101], N. Proklova[110], K. Prokofiev[61c], F. Prokoshin[144b], S. Protopopescu[29], J. Proudfoot[6], M. Przybycien[81a], A. Puri[170], P. Puzo[128], J. Qian[103], Y. Qin[98], A. Quadt[51], M. Queitsch-Maitland[44], A. Qureshi[1], P. Rados[102], F. Ragusa[66a,66b], G. Rahal[95], J. A. Raine[52], S. Rajagopalan[29], A. Ramirez Morales[90], T. Rashid[128], S. Raspopov[5], M. G. Ratti[66a,66b], D. M. Rauch[44], F. Rauscher[112], S. Rave[97], B. Ravina[146], I. Ravinovich[177], J. H. Rawling[98], M. Raymond[35], A. L. Read[130], N. P. Readioff[56], M. Reale[65a,65b], D. M. Rebuzzi[68a,68b], A. Redelbach[174], G. Redlinger[29], R. Reece[143], R. G. Reed[32c], K. Reeves[42], L. Rehnisch[19], J. Reichert[133], D. Reikher[158], A. Reiss[97], C. Rembser[35], H. Ren[15d], M. Rescigno[70a], S. Resconi[66a], E. D. Resseguie[133], S. Rettie[172], E. Reynolds[21], O. L. Rezanova[120a,120b], P. Reznicek[139], E. Ricci[73a,73b], R. Richter[113], S. Richter[44], E. Richter-Was[81b], O. Ricken[24], M. Ridel[132], P. Rieck[113], C. J. Riegel[179], O. Rifki[44], M. Rijssenbeek[152], A. Rimoldi[68a,68b], M. Rimoldi[20], L. Rinaldi[23b], G. Ripellino[151], B. Ristić[87], E. Ritsch[35], I. Riu[14], J. C. Rivera Vergara[144a], F. Rizatdinova[125], E. Rizvi[90], C. Rizzi[14], R. T. Roberts[98], S. H. Robertson[101,ab], D. Robinson[31], J. E. M. Robinson[44], A. Robson[55], E. Rocco[97], C. Roda[69a,69b], Y. Rodina[99], S. Rodriguez Bosca[171], A. Rodriguez Perez[14], D. Rodriguez Rodriguez[171], A. M. Rodríguez Vera[165b], S. Roe[35], C. S. Rogan[57], O. Røhne[130], R. Röhrig[113], C. P. A. Roland[63], J. Roloff[57], A. Romaniouk[110], M. Romano[23a,23b], N. Rompotis[88], M. Ronzani[121], L. Roos[132],

S. Rosati[70a], K. Rosbach[50], P. Rose[143], N-A. Rosien[51], B. J. Rosser[133], E. Rossi[44], E. Rossi[72a,72b], E. Rossi[67a,67b], L. P. Rossi[53b], L. Rossini[66a,66b], J. H. N. Rosten[31], R. Rosten[14], M. Rotaru[27b], J. Rothberg[145], D. Rousseau[128], D. Roy[32c], A. Rozanov[99], Y. Rozen[157], X. Ruan[32c], F. Rubbo[150], F. Rühr[50], A. Ruiz-Martinez[171], Z. Rurikova[50], N. A. Rusakovich[77], H. L. Russell[101], J. P. Rutherfoord[7], E. M. Rüttinger[44,k], Y. F. Ryabov[134], M. Rybar[170], G. Rybkin[128], S. Ryu[6], A. Ryzhov[140], G. F. Rzehorz[51], P. Sabatini[51], G. Sabato[118], S. Sacerdoti[128], H. F-W. Sadrozinski[143], R. Sadykov[77], F. Safai Tehrani[70a], P. Saha[119], M. Sahinsoy[59a], A. Sahu[179], M. Saimpert[44], M. Saito[160], T. Saito[160], H. Sakamoto[160], A. Sakharov[121,ai], D. Salamani[52], G. Salamanna[72a,72b], J. E. Salazar Loyola[144b], P. H. Sales De Bruin[169], D. Salihagic[113], A. Salnikov[150], J. Salt[171], D. Salvatore[40a,40b], F. Salvatore[153], A. Salvucci[61a,61b,61c], A. Salzburger[35], J. Samarati[35], D. Sammel[50], D. Sampsonidis[159], D. Sampsonidou[159], J. Sánchez[171], A. Sanchez Pineda[64a,64c], H. Sandaker[130], C. O. Sander[44], M. Sandhoff[179], C. Sandoval[22], D. P. C. Sankey[141], M. Sannino[53a,53b], Y. Sano[115], A. Sansoni[49], C. Santoni[37], H. Santos[136a], I. Santoyo Castillo[153], A. Santra[171], A. Sapronov[77], J. G. Saraiva[136a,136d], O. Sasaki[79], K. Sato[166], E. Sauvan[5], P. Savard[164,aq], N. Savic[113], R. Sawada[160], C. Sawyer[141], L. Sawyer[93,ah], C. Sbarra[23b], A. Sbrizzi[23a,23b], T. Scanlon[92], J. Schaarschmidt[145], P. Schacht[113], B. M. Schachtner[112], D. Schaefer[36], L. Schaefer[133], J. Schaeffer[97], S. Schaepe[35], U. Schäfer[97], A. C. Schaffer[128], D. Schaile[112], R. D. Schamberger[152], N. Scharmberg[98], V. A. Schegelsky[134], D. Scheirich[139], F. Schenck[19], M. Schernau[168], C. Schiavi[53a,53b], S. Schier[143], L. K. Schildgen[24], Z. M. Schillaci[26], E. J. Schioppa[35], M. Schioppa[40a,40b], K. E. Schleicher[50], S. Schlenker[35], K. R. Schmidt-Sommerfeld[113], K. Schmieden[35], C. Schmitt[97], S. Schmitt[44], S. Schmitz[97], J. C. Schmoeckel[44], U. Schnoor[50], L. Schoeffel[142], A. Schoening[59b], E. Schopf[131], M. Schott[97], J. F. P. Schouwenberg[117], J. Schovancova[35], S. Schramm[52], A. Schulte[97], H-C. Schultz-Coulon[59a], M. Schumacher[50], B. A. Schumm[143], Ph. Schune[142], A. Schwartzman[150], T. A. Schwarz[103], Ph. Schwemling[142], R. Schwienhorst[104], A. Sciandra[24], G. Sciolla[26], M. Scornajenghi[40a,40b], F. Scuri[69a], F. Scutti[102], L. M. Scyboz[113], J. Searcy[103], C. D. Sebastiani[70a,70b], P. Seema[19], S. C. Seidel[116], A. Seiden[143], T. Seiss[36], J. M. Seixas[78b], G. Sekhniaidze[67a], K. Sekhon[103], S. J. Sekula[41], N. Semprini-Cesari[23a,23b], S. Sen[47], S. Senkin[37], C. Serfon[130], L. Serin[128], L. Serkin[64a,64b], M. Sessa[58a], H. Severini[124], F. Sforza[167], A. Sfyrla[52], E. Shabalina[51], J. D. Shahinian[143], N. W. Shaikh[43a,43b], L. Y. Shan[15a], R. Shang[170], J. T. Shank[25], M. Shapiro[18], A. S. Sharma[1], A. Sharma[131], P. B. Shatalov[109], K. Shaw[153], S. M. Shaw[98], A. Shcherbakova[134], Y. Shen[124], N. Sherafati[33], A. D. Sherman[25], P. Sherwood[92], L. Shi[155,am], S. Shimizu[79], C. O. Shimmin[180], M. Shimojima[114], I. P. J. Shipsey[131], S. Shirabe[85], M. Shiyakova[77], J. Shlomi[177], A. Shmeleva[108], D. Shoaleh Saadi[107], M. J. Shochet[36], S. Shojaii[102], D. R. Shope[124], S. Shrestha[122], E. Shulga[110], P. Sicho[137], A. M. Sickles[170], P. E. Sidebo[151], E. Sideras Haddad[32c], O. Sidiropoulou[35], A. Sidoti[23a,23b], F. Siegert[46], Dj. Sijacki[16], J. Silva[136a], M. Silva Jr.[178], M. V. Silva Oliveira[78a], S. B. Silverstein[43a], S. Simion[128], E. Simioni[97], M. Simon[97], R. Simoniello[97], P. Sinervo[164], N. B. Sinev[127], M. Sioli[23a,23b], G. Siragusa[174], I. Siral[103], S. Yu. Sivoklokov[111], J. Sjölin[43a,43b], P. Skubic[124], M. Slater[21], T. Slavicek[138], M. Slawinska[82], K. Sliwa[167], R. Slovak[139], V. Smakhtin[177], B. H. Smart[5], J. Smiesko[28a], N. Smirnov[110], S. Yu. Smirnov[110], Y. Smirnov[110], L. N. Smirnova[111], O. Smirnova[94], J. W. Smith[51], M. N. K. Smith[38], M. Smizanska[87], K. Smolek[138], A. Smykiewicz[82], A. A. Snesarev[108], I. M. Snyder[127], S. Snyder[29], R. Sobie[173,ab], A. M. Soffa[168], A. Soffer[158], A. Søgaard[48], D. A. Soh[155], G. Sokhrannyi[89], C. A. Solans Sanchez[35], M. Solar[138], E. Yu. Soldatov[110], U. Soldevila[171], A. A. Solodkov[140], A. Soloshenko[77], O. V. Solovyanov[140], V. Solovyev[134], P. Sommer[146], H. Son[167], W. Song[141], W. Y. Song[165b], A. Sopczak[138], F. Sopkova[28b], C. L. Sotiropoulou[69a,69b], S. Sottocornola[68a,68b], R. Soualah[64a,64c,h], A. M. Soukharev[120a,120b], D. South[44], B. C. Sowden[91], S. Spagnolo[65a,65b], M. Spalla[113], M. Spangenberg[175], F. Spanò[91], D. Sperlich[19], F. Spettel[113], T. M. Spieker[59a], R. Spighi[23b], G. Spigo[35], L. A. Spiller[102], D. P. Spiteri[55], M. Spousta[139], A. Stabile[66a,66b], R. Stamen[59a], S. Stamm[19], E. Stanecka[82], R. W. Stanek[6], C. Stanescu[72a], B. Stanislaus[131], M. M. Stanitzki[44], B. Stapf[118], S. Stapnes[130], E. A. Starchenko[140], G. H. Stark[36], J. Stark[56], S. H Stark[39], P. Staroba[137], P. Starovoitov[59a], S. Stärz[35], R. Staszewski[82], M. Stegler[44], P. Steinberg[29], B. Stelzer[149], H. J. Stelzer[35], O. Stelzer-Chilton[165a], H. Stenzel[54], T. J. Stevenson[90], G. A. Stewart[55], M. C. Stockton[127], G. Stoicea[27b], P. Stolte[51], S. Stonjek[113], A. Straessner[46], J. Strandberg[151], S. Strandberg[43a,43b], M. Strauss[124], P. Strizenec[28b], R. Ströhmer[174], D. M. Strom[127], R. Stroynowski[41], A. Strubig[48], S. A. Stucci[29], B. Stugu[17], J. Stupak[124], N. A. Styles[44], D. Su[150], J. Su[135], S. Suchek[59a], Y. Sugaya[129], M. Suk[138], V. V. Sulin[108], M. J. Sullivan[88], D. M. S. Sultan[52], S. Sultansoy[4c], T. Sumida[83], S. Sun[103], X. Sun[3], K. Suruliz[153], C. J. E. Suster[154], M. R. Sutton[153], S. Suzuki[79], M. Svatos[137], M. Swiatlowski[36], S. P. Swift[2], A. Sydorenko[97], I. Sykora[28a], T. Sykora[139], D. Ta[97], K. Tackmann[44,y], J. Taenzer[158], A. Taffard[168], R. Tafirout[165a], E. Tahirovic[90], N. Taiblum[158], H. Takai[29], R. Takashima[84], E. H. Takasugi[113], K. Takeda[80], T. Takeshita[147], Y. Takubo[79], M. Talby[99], A. A. Talyshev[120a,120b], J. Tanaka[160], M. Tanaka[162], R. Tanaka[128], B. B. Tannenwald[122], S. Tapia Araya[144b], S. Tapprogge[97], A. Tarek Abouelfadl Mohamed[132], S. Tarem[157], G. Tarna[27b,d], G. F. Tartarelli[66a], P. Tas[139], M. Tasevsky[137], T. Tashiro[83], E. Tassi[40a,40b], A. Tavares Delgado[136a,136b], Y. Tayalati[34e], A. C. Taylor[116], A. J. Taylor[48], G. N. Taylor[102], P. T. E. Taylor[102], W. Taylor[165b], A. S. Tee[87], P. Teixeira-Dias[91], H. Ten Kate[35],

P. K. Teng[155], J. J. Teoh[118], S. Terada[79], K. Terashi[160], J. Terron[96], S. Terzo[14], M. Testa[49], R. J. Teuscher[164,ab], S. J. Thais[180], T. Theveneaux-Pelzer[44], F. Thiele[39], D. W. Thomas[91], J. P. Thomas[21], A. S. Thompson[55], P. D. Thompson[21], L. A. Thomsen[180], E. Thomson[133], Y. Tian[38], R. E. Ticse Torres[51], V. O. Tikhomirov[108,ak], Yu. A. Tikhonov[120a,120b], S. Timoshenko[110], P. Tipton[180], S. Tisserant[99], K. Todome[162], S. Todorova-Nova[5], S. Todt[46], J. Tojo[85], S. Tokár[28a], K. Tokushuku[79], E. Tolley[122], K. G. Tomiwa[32c], M. Tomoto[115], L. Tompkins[150], K. Toms[116], B. Tong[57], P. Tornambe[50], E. Torrence[127], H. Torres[46], E. Torró Pastor[145], C. Tosciri[131], J. Toth[99,aa], F. Touchard[99], D. R. Tovey[146], C. J. Treado[121], T. Trefzger[174], F. Tresoldi[153], A. Tricoli[29], I. M. Trigger[165a], S. Trincaz-Duvoid[132], M. F. Tripiana[14], W. Trischuk[164], B. Trocmé[56], A. Trofymov[128], C. Troncon[66a], M. Trovatelli[173], F. Trovato[153], L. Truong[32b], M. Trzebinski[82], A. Trzupek[82], F. Tsai[44], J. C-L. Tseng[131], P. V. Tsiareshka[105], A. Tsirigotis[159], N. Tsirintanis[9], V. Tsiskaridze[152], E. G. Tskhadadze[156a], I. I. Tsukerman[109], V. Tsulaia[18], S. Tsuno[79], D. Tsybychev[152,163], Y. Tu[61b], A. Tudorache[27b], V. Tudorache[27b], T. T. Tulbure[27a], A. N. Tuna[57], S. Turchikhin[77], D. Turgeman[177], I. Turk Cakir[4b,s], R. Turra[66a], P. M. Tuts[38], E. Tzovara[97], G. Ucchielli[23a,23b], I. Ueda[79], M. Ughetto[43a,43b], F. Ukegawa[166], G. Unal[35], A. Undrus[29], G. Unel[168], F. C. Ungaro[102], Y. Unno[79], K. Uno[160], J. Urban[28b], P. Urquijo[102], P. Urrejola[97], G. Usai[8], J. Usui[79], L. Vacavant[99], V. Vacek[138], B. Vachon[101], K. O. H. Vadla[130], A. Vaidya[92], C. Valderanis[112], E. Valdes Santurio[43a,43b], M. Valente[52], S. Valentinetti[23a,23b], A. Valero[171], L. Valéry[44], R. A. Vallance[21], A. Vallier[5], J. A. Valls Ferrer[171], T. R. Van Daalen[14], H. Van der Graaf[118], P. Van Gemmeren[6], J. Van Nieuwkoop[149], I. Van Vulpen[118], M. Vanadia[71a,71b], W. Vandelli[35], A. Vaniachine[163], P. Vankov[118], R. Vari[70a], E. W. Varnes[7], C. Varni[53a,53b], T. Varol[41], D. Varouchas[128], K. E. Varvell[154], G. A. Vasquez[144b], J. G. Vasquez[180], F. Vazeille[37], D. Vazquez Furelos[14], T. Vazquez Schroeder[101], J. Veatch[51], V. Vecchio[72a,72b], L. M. Veloce[164], F. Veloso[136a,136c], S. Veneziano[70a], A. Ventura[65a,65b], M. Venturi[173], N. Venturi[35], V. Vercesi[68a], M. Verducci[72a,72b], C. M. Vergel Infante[76], C. Vergis[24], W. Verkerke[118], A. T. Vermeulen[118], J. C. Vermeulen[118], M. C. Vetterli[149,aq], N. Viaux Maira[144b], M. Vicente Barreto Pinto[52], I. Vichou[170,*], T. Vickey[146], O. E. Vickey Boeriu[146], G. H. A. Viehhauser[131], S. Viel[18], L. Vigani[131], M. Villa[23a,23b], M. Villaplana Perez[66a,66b], E. Vilucchi[49], M. G. Vincter[33], V. B. Vinogradov[77], A. Vishwakarma[44], C. Vittori[23a,23b], I. Vivarelli[153], S. Vlachos[10], M. Vogel[179], P. Vokac[138], G. Volpi[14], S. E. Von Buddenbrock[32c], E. von Toerne[24], V. Vorobel[139], K. Vorobev[110], M. Vos[171], J. H. Vossebeld[88], N. Vranjes[16], M. Vranjes Milosavljevic[16], V. Vrba[138], M. Vreeswijk[118], T. Šfiligoj[89], R. Vuillermet[35], I. Vukotic[36], T. Ženiš[28a], L. Živković[16], P. Wagner[24], W. Wagner[179], J. Wagner-Kuhr[112], H. Wahlberg[86], S. Wahrmund[46], K. Wakamiya[80], V. M. Walbrecht[113], J. Walder[87], R. Walker[112], S. D. Walker[91], W. Walkowiak[148], V. Wallangen[43a,43b], A. M. Wang[57], C. Wang[58b,d], F. Wang[178], H. Wang[18], H. Wang[3], J. Wang[154], J. Wang[59b], P. Wang[41], Q. Wang[124], R.-J. Wang[132], R. Wang[58a], R. Wang[6], S. M. Wang[155], T. Wang[58a], W. Wang[15c,ac], W. X. Wang[58a,ac], Y. Wang[58a], Z. Wang[58c], C. Wanotayaroj[44], A. Warburton[101], C. P. Ward[31], D. R. Wardrope[92], A. Washbrook[48], P. M. Watkins[21], A. T. Watson[21], M. F. Watson[21], G. Watts[145], S. Watts[98], B. M. Waugh[92], A. F. Webb[11], S. Webb[97], C. Weber[180], M. S. Weber[20], S. A. Weber[33], S. M. Weber[59a], A. R. Weidberg[131], B. Weinert[63], J. Weingarten[51], M. Weirich[97], C. Weiser[50], P. S. Wells[35], T. Wenaus[29], T. Wengler[35], S. Wenig[35], N. Wermes[24], M. D. Werner[76], P. Werner[35], M. Wessels[59a], T. D. Weston[20], K. Whalen[127], N. L. Whallon[145], A. M. Wharton[87], A. S. White[103], A. White[8], M. J. White[1], R. White[144b], D. Whiteson[168], B. W. Whitmore[87], F. J. Wickens[141], W. Wiedenmann[178], M. Wielers[141], C. Wiglesworth[39], L. A. M. Wiik-Fuchs[50], F. Wilk[98], H. G. Wilkens[35], L. J. Wilkins[91], H. H. Williams[133], S. Williams[31], C. Willis[104], S. Willocq[100], J. A. Wilson[21], I. Wingerter-Seez[5], E. Winkels[153], F. Winklmeier[127], O. J. Winston[153], B. T. Winter[24], M. Wittgen[150], M. Wobisch[93], A. Wolf[97], T. M. H. Wolf[118], R. Wolff[99], M. W. Wolter[82], H. Wolters[136a,136c], V. W. S. Wong[172], N. L. Woods[143], S. D. Worm[21], B. K. Wosiek[82], K. W. Woźniak[82], K. Wraight[55], M. Wu[36], S. L. Wu[178], X. Wu[52], Y. Wu[58a], T. R. Wyatt[98], B. M. Wynne[48], S. Xella[39], Z. Xi[103], L. Xia[175], D. Xu[15a], H. Xu[58a], L. Xu[29], T. Xu[142], W. Xu[103], B. Yabsley[154], S. Yacoob[32a], K. Yajima[129], D. P. Yallup[92], D. Yamaguchi[162], Y. Yamaguchi[162], A. Yamamoto[79], T. Yamanaka[160], F. Yamane[80], M. Yamatani[160], T. Yamazaki[160], Y. Yamazaki[80], Z. Yan[25], H. J. Yang[58c,58d], H. T. Yang[18], S. Yang[75], Y. Yang[160], Z. Yang[17], W-M. Yao[18], Y. C. Yap[44], Y. Yasu[79], E. Yatsenko[58c,58d], J. Ye[41], S. Ye[29], I. Yeletskikh[77], E. Yigitbasi[25], E. Yildirim[97], K. Yorita[176], K. Yoshihara[133], C. J. S. Young[35], C. Young[150], J. Yu[8], J. Yu[76], X. Yue[59a], S. P. Y. Yuen[24], B. Zabinski[82], G. Zacharis[10], E. Zaffaroni[52], R. Zaidan[14], A. M. Zaitsev[140,aj], T. Zakareishvili[156b], N. Zakharchuk[33], J. Zalieckas[17], S. Zambito[57], D. Zanzi[35], D. R. Zaripovas[55], S. V. Zeißner[45], C. Zeitnitz[179], G. Zemaityte[131], J. C. Zeng[170], Q. Zeng[150], O. Zenin[140], D. Zerwas[128], M. Zgubič[131], D. F. Zhang[58b], D. Zhang[103], F. Zhang[178], G. Zhang[58a], H. Zhang[15c], J. Zhang[6], L. Zhang[15c], L. Zhang[58a], M. Zhang[170], P. Zhang[15c], R. Zhang[58a], R. Zhang[24], X. Zhang[58b], Y. Zhang[15d], Z. Zhang[128], X. Zhao[41], Y. Zhao[58b,128,ag], Z. Zhao[58a], A. Zhemchugov[77], Z. Zheng[103], D. Zhong[170], B. Zhou[103], C. Zhou[178], L. Zhou[41], M. S. Zhou[15d], M. Zhou[152], N. Zhou[58c], Y. Zhou[7], C. G. Zhu[58b], H. L. Zhu[58a], H. Zhu[15a], J. Zhu[103], Y. Zhu[58a], X. Zhuang[15a], K. Zhukov[108], V. Zhulanov[120a,120b], A. Zibell[174], D. Zieminska[63], N. I. Zimine[77], S. Zimmermann[50], Z. Zinonos[113], M. Zinser[97], M. Ziolkowski[148], G. Zobernig[178], A. Zoccoli[23a,23b], K. Zoch[51], T. G. Zorbas[146], R. Zou[36], M. Zur Nedden[19], L. Zwalinski[35]

1 Department of Physics, University of Adelaide, Adelaide, Australia

2 Physics Department, SUNY Albany, Albany, NY, USA

3 Department of Physics, University of Alberta, Edmonton, AB, Canada

4 [a]Department of Physics, Ankara University, Ankara, Turkey; [b]Istanbul Aydin University, Istanbul, Turkey; [c]Division of Physics, TOBB University of Economics and Technology, Ankara, Turkey

5 LAPP, Université Grenoble Alpes, Université Savoie Mont Blanc, CNRS/IN2P3, Annecy, France

6 High Energy Physics Division, Argonne National Laboratory, Argonne, IL, USA

7 Department of Physics, University of Arizona, Tucson, AZ, USA

8 Department of Physics, University of Texas at Arlington, Arlington, TX, USA

9 Physics Department, National and Kapodistrian University of Athens, Athens, Greece

10 Physics Department, National Technical University of Athens, Zografou, Greece

11 Department of Physics, University of Texas at Austin, Austin, TX, USA

12 [a]Faculty of Engineering and Natural Sciences, Bahcesehir University, Istanbul, Turkey; [b]Faculty of Engineering and Natural Sciences, Istanbul Bilgi University, Istanbul, Turkey; [c]Department of Physics, Bogazici University, Istanbul, Turkey; [d]Department of Physics Engineering, Gaziantep University, Gaziantep, Turkey

13 Institute of Physics, Azerbaijan Academy of Sciences, Baku, Azerbaijan

14 Institut de Física d'Altes Energies (IFAE), Barcelona Institute of Science and Technology, Barcelona, Spain

15 [a]Institute of High Energy Physics, Chinese Academy of Sciences, Beijing, China; [b]Physics Department, Tsinghua University, Beijing, China; [c]Department of Physics, Nanjing University, Nanjing, China; [d]University of Chinese Academy of Science (UCAS), Beijing, China

16 Institute of Physics, University of Belgrade, Belgrade, Serbia

17 Department for Physics and Technology, University of Bergen, Bergen, Norway

18 Physics Division, Lawrence Berkeley National Laboratory and University of California, Berkeley, CA, USA

19 Institut für Physik, Humboldt Universität zu Berlin, Berlin, Germany

20 Albert Einstein Center for Fundamental Physics and Laboratory for High Energy Physics, University of Bern, Bern, Switzerland

21 School of Physics and Astronomy, University of Birmingham, Birmingham, UK

22 Centro de Investigaciónes, Universidad Antonio Nariño, Bogotá, Colombia

23 [a]Dipartimento di Fisica e Astronomia, Università di Bologna, Bologna, Italy; [b]INFN Sezione di Bologna, Bologna, Italy

24 Physikalisches Institut, Universität Bonn, Bonn, Germany

25 Department of Physics, Boston University, Boston, MA, USA

26 Department of Physics, Brandeis University, Waltham, MA, USA

27 [a]Transilvania University of Brasov, Brasov, Romania; [b]Horia Hulubei National Institute of Physics and Nuclear Engineering, Bucharest, Romania; [c]Department of Physics, Alexandru Ioan Cuza University of Iasi, Iasi, Romania; [d]Physics Department, National Institute for Research and Development of Isotopic and Molecular Technologies, Cluj-Napoca, Romania; [e]University Politehnica Bucharest, Bucharest, Romania; [f]West University in Timisoara, Timisoara, Romania

28 [a]Faculty of Mathematics, Physics and Informatics, Comenius University, Bratislava, Slovakia; [b]Department of Subnuclear Physics, Institute of Experimental Physics of the Slovak Academy of Sciences, Kosice, Slovak Republic

29 Physics Department, Brookhaven National Laboratory, Upton, NY, USA

30 Departamento de Física, Universidad de Buenos Aires, Buenos Aires, Argentina

31 Cavendish Laboratory, University of Cambridge, Cambridge, UK

32 [a]Department of Physics, University of Cape Town, Cape Town, South Africa; [b]Department of Mechanical Engineering Science, University of Johannesburg, Johannesburg, South Africa; [c]School of Physics, University of the Witwatersrand, Johannesburg, South Africa

33 Department of Physics, Carleton University, Ottawa, ON, Canada

34 [a]Faculté des Sciences Ain Chock, Réseau Universitaire de Physique des Hautes Energies-Université Hassan II, Casablanca, Morocco; [b]Centre National de l'Energie des Sciences Techniques Nucleaires (CNESTEN), Rabat, Morocco; [c]Faculté des Sciences Semlalia, Université Cadi Ayyad, LPHEA-Marrakech, Marrakech, Morocco; [d]Faculté des Sciences, Université Mohamed Premier and LPTPM, Oujda, Morocco; [e]Faculté des sciences, Université Mohammed V, Rabat, Morocco

35 CERN, Geneva, Switzerland

[36] Enrico Fermi Institute, University of Chicago, Chicago, IL, USA

[37] LPC, Université Clermont Auvergne, CNRS/IN2P3, Clermont-Ferrand, France

[38] Nevis Laboratory, Columbia University, Irvington, NY, USA

[39] Niels Bohr Institute, University of Copenhagen, Copenhagen, Denmark

[40] [a]Dipartimento di Fisica, Università della Calabria, Rende, Italy; [b]INFN Gruppo Collegato di Cosenza, Laboratori Nazionali di Frascati, Frascati, Italy

[41] Physics Department, Southern Methodist University, Dallas, TX, USA

[42] Physics Department, University of Texas at Dallas, Richardson, TX, USA

[43] [a]Department of Physics, Stockholm University, Stockholm, Sweden; [b]Oskar Klein Centre, Stockholm, Sweden

[44] Deutsches Elektronen-Synchrotron DESY, Hamburg and Zeuthen, Germany

[45] Lehrstuhl für Experimentelle Physik IV, Technische Universität Dortmund, Dortmund, Germany

[46] Institut für Kern- und Teilchenphysik, Technische Universität Dresden, Dresden, Germany

[47] Department of Physics, Duke University, Durham, NC, USA

[48] SUPA-School of Physics and Astronomy, University of Edinburgh, Edinburgh, UK

[49] INFN e Laboratori Nazionali di Frascati, Frascati, Italy

[50] Physikalisches Institut, Albert-Ludwigs-Universität Freiburg, Freiburg, Germany

[51] II. Physikalisches Institut, Georg-August-Universität Göttingen, Göttingen, Germany

[52] Département de Physique Nucléaire et Corpusculaire, Université de Genève, Geneva, Switzerland

[53] [a]Dipartimento di Fisica, Università di Genova, Genoa, Italy; [b]INFN Sezione di Genova, Genoa, Italy

[54] II. Physikalisches Institut, Justus-Liebig-Universität Giessen, Giessen, Germany

[55] SUPA-School of Physics and Astronomy, University of Glasgow, Glasgow, UK

[56] LPSC, Université Grenoble Alpes, CNRS/IN2P3, Grenoble INP, Grenoble, France

[57] Laboratory for Particle Physics and Cosmology, Harvard University, Cambridge, MA, USA

[58] [a]Department of Modern Physics and State Key Laboratory of Particle Detection and Electronics, University of Science and Technology of China, Hefei, China; [b]Institute of Frontier and Interdisciplinary Science and Key Laboratory of Particle Physics and Particle Irradiation (MOE), Shandong University, Qingdao, China; [c]School of Physics and Astronomy, Shanghai Jiao Tong University, KLPPAC-MoE, SKLPPC, Shanghai, China; [d]Tsung-Dao Lee Institute, Shanghai, China

[59] [a]Kirchhoff-Institut für Physik, Ruprecht-Karls-Universität Heidelberg, Heidelberg, Germany; [b]Physikalisches Institut, Ruprecht-Karls-Universität Heidelberg, Heidelberg, Germany

[60] Faculty of Applied Information Science, Hiroshima Institute of Technology, Hiroshima, Japan

[61] [a]Department of Physics, Chinese University of Hong Kong, Shatin, NT, Hong Kong; [b]Department of Physics, University of Hong Kong, Hong Kong, China; [c]Department of Physics and Institute for Advanced Study, Hong Kong University of Science and Technology, Clear Water Bay, Kowloon, Hong Kong, China

[62] Department of Physics, National Tsing Hua University, Hsinchu, Taiwan

[63] Department of Physics, Indiana University, Bloomington, IN, USA

[64] [a]INFN Gruppo Collegato di Udine, Sezione di Trieste, Udine, Italy; [b]ICTP, Trieste, Italy; [c]Dipartimento di Chimica, Fisica e Ambiente, Università di Udine, Udine, Italy

[65] [a]INFN Sezione di Lecce, Lecce, Italy; [b]Dipartimento di Matematica e Fisica, Università del Salento, Lecce, Italy

[66] [a]INFN Sezione di Milano, Milan, Italy; [b]Dipartimento di Fisica, Università di Milano, Milan, Italy

[67] [a]INFN Sezione di Napoli, Naples, Italy; [b]Dipartimento di Fisica, Università di Napoli, Naples, Italy

[68] [a]INFN Sezione di Pavia, Pavia, Italy; [b]Dipartimento di Fisica, Università di Pavia, Pavia, Italy

[69] [a]INFN Sezione di Pisa, Pisa, Italy; [b]Dipartimento di Fisica E. Fermi, Università di Pisa, Pisa, Italy

[70] [a]INFN Sezione di Roma, Rome, Italy; [b]Dipartimento di Fisica, Sapienza Università di Roma, Rome, Italy

[71] [a]INFN Sezione di Roma Tor Vergata, Rome, Italy; [b]Dipartimento di Fisica, Università di Roma Tor Vergata, Rome, Italy

[72] [a]INFN Sezione di Roma Tre, Rome, Italy; [b]Dipartimento di Matematica e Fisica, Università Roma Tre, Rome, Italy

[73] [a]INFN-TIFPA, Povo, Italy; [b]Università degli Studi di Trento, Trento, Italy

[74] Institut für Astro- und Teilchenphysik, Leopold-Franzens-Universität, Innsbruck, Austria

[75] University of Iowa, Iowa City, IA, USA

[76] Department of Physics and Astronomy, Iowa State University, Ames, IA, USA

[77] Joint Institute for Nuclear Research, Dubna, Russia

[78] [a]Departamento de Engenharia Elétrica, Universidade Federal de Juiz de Fora (UFJF), Juiz de Fora,

Brazil; [b]Universidade Federal do Rio De Janeiro COPPE/EE/IF, Rio de Janeiro, Brazil; [c]Universidade Federal de São João del Rei (UFSJ), São João del Rei, Brazil; [d]Instituto de Física, Universidade de São Paulo, São Paulo, Brazil

[79] KEK, High Energy Accelerator Research Organization, Tsukuba, Japan

[80] Graduate School of Science, Kobe University, Kobe, Japan

[81] [a]Faculty of Physics and Applied Computer Science, AGH University of Science and Technology, Kraków, Poland; [b]Marian Smoluchowski Institute of Physics, Jagiellonian University, Kraków, Poland

[82] Institute of Nuclear Physics Polish Academy of Sciences, Kraków, Poland

[83] Faculty of Science, Kyoto University, Kyoto, Japan

[84] Kyoto University of Education, Kyoto, Japan

[85] Research Center for Advanced Particle Physics and Department of Physics, Kyushu University, Fukuoka, Japan

[86] Instituto de Física La Plata, Universidad Nacional de La Plata and CONICET, La Plata, Argentina

[87] Physics Department, Lancaster University, Lancaster, UK

[88] Oliver Lodge Laboratory, University of Liverpool, Liverpool, UK

[89] Department of Experimental Particle Physics, Jožef Stefan Institute and Department of Physics, University of Ljubljana, Ljubljana, Slovenia

[90] School of Physics and Astronomy, Queen Mary University of London, London, UK

[91] Department of Physics, Royal Holloway University of London, Egham, UK

[92] Department of Physics and Astronomy, University College London, London, UK

[93] Louisiana Tech University, Ruston, LA, USA

[94] Fysiska institutionen, Lunds universitet, Lund, Sweden

[95] Centre de Calcul de l'Institut National de Physique Nucléaire et de Physique des Particules (IN2P3), Villeurbanne, France

[96] Departamento de Física Teorica C-15 and CIAFF, Universidad Autónoma de Madrid, Madrid, Spain

[97] Institut für Physik, Universität Mainz, Mainz, Germany

[98] School of Physics and Astronomy, University of Manchester, Manchester, UK

[99] CPPM, Aix-Marseille Université, CNRS/IN2P3, Marseille, France

[100] Department of Physics, University of Massachusetts, Amherst, MA, USA

[101] Department of Physics, McGill University, Montreal, QC, Canada

[102] School of Physics, University of Melbourne, Parkville, VIC, Australia

[103] Department of Physics, University of Michigan, Ann Arbor, MI, USA

[104] Department of Physics and Astronomy, Michigan State University, East Lansing, MI, USA

[105] B.I. Stepanov Institute of Physics, National Academy of Sciences of Belarus, Minsk, Belarus

[106] Research Institute for Nuclear Problems of Byelorussian State University, Minsk, Belarus

[107] Group of Particle Physics, University of Montreal, Montreal, QC, Canada

[108] P.N. Lebedev Physical Institute of the Russian Academy of Sciences, Moscow, Russia

[109] Institute for Theoretical and Experimental Physics (ITEP), Moscow, Russia

[110] National Research Nuclear University MEPhI, Moscow, Russia

[111] D.V. Skobeltsyn Institute of Nuclear Physics, M.V. Lomonosov Moscow State University, Moscow, Russia

[112] Fakultät für Physik, Ludwig-Maximilians-Universität München, Munich, Germany

[113] Max-Planck-Institut für Physik (Werner-Heisenberg-Institut), Munich, Germany

[114] Nagasaki Institute of Applied Science, Nagasaki, Japan

[115] Graduate School of Science and Kobayashi-Maskawa Institute, Nagoya University, Nagoya, Japan

[116] Department of Physics and Astronomy, University of New Mexico, Albuquerque, NM, USA

[117] Institute for Mathematics, Astrophysics and Particle Physics, Radboud University Nijmegen/Nikhef, Nijmegen, The Netherlands

[118] Nikhef National Institute for Subatomic Physics, University of Amsterdam, Amsterdam, The Netherlands

[119] Department of Physics, Northern Illinois University, De Kalb, IL, USA

[120] [a]Budker Institute of Nuclear Physics, SB RAS, Novosibirsk, Russia; [b]Novosibirsk State University, Novosibirsk, Russia

[121] Department of Physics, New York University, New York, NY, USA

[122] Ohio State University, Columbus, OH, USA

[123] Faculty of Science, Okayama University, Okayama, Japan

[124] Homer L. Dodge Department of Physics and Astronomy, University of Oklahoma, Norman, OK, USA

[125] Department of Physics, Oklahoma State University, Stillwater, OK, USA

[126] Palacký University, RCPTM, Joint Laboratory of Optics, Olomouc, Czech Republic

[127] Center for High Energy Physics, University of Oregon, Eugene, OR, USA

[128] LAL, Université Paris-Sud, CNRS/IN2P3, Université Paris-Saclay, Orsay, France

[129] Graduate School of Science, Osaka University, Osaka, Japan

[130] Department of Physics, University of Oslo, Oslo, Norway

[131] Department of Physics, Oxford University, Oxford, UK

[132] LPNHE, Sorbonne Université, Paris Diderot Sorbonne Paris Cité, CNRS/IN2P3, Paris, France

[133] Department of Physics, University of Pennsylvania, Philadelphia, PA, USA

[134] Konstantinov Nuclear Physics Institute of National Research Centre "Kurchatov Institute", PNPI, St. Petersburg, Russia

[135] Department of Physics and Astronomy, University of Pittsburgh, Pittsburgh, PA, USA

[136] [a]Laboratório de Instrumentação e Física Experimental de Partículas-LIP, Lisbon, Portugal; [b]Departamento de Física, Faculdade de Ciências, Universidade de Lisboa, Lisbon, Portugal; [c]Departamento de Física, Universidade de Coimbra, Coimbra, Portugal; [d]Centro de Física Nuclear da Universidade de Lisboa, Lisbon, Portugal; [e]Departamento de Física, Universidade do Minho, Braga, Portugal; [f]Departamento de Física Teorica y del Cosmos, Universidad de Granada, Granada, Spain; [g]Dep Física and CEFITEC of Faculdade de Ciências e Tecnologia, Universidade Nova de Lisboa, Caparica, Portugal

[137] Institute of Physics, Academy of Sciences of the Czech Republic, Prague, Czech Republic

[138] Czech Technical University in Prague, Prague, Czech Republic

[139] Faculty of Mathematics and Physics, Charles University, Prague, Czech Republic

[140] State Research Center Institute for High Energy Physics, NRC KI, Protvino, Russia

[141] Particle Physics Department, Rutherford Appleton Laboratory, Didcot, UK

[142] IRFU, CEA, Université Paris-Saclay, Gif-sur-Yvette, France

[143] Santa Cruz Institute for Particle Physics, University of California Santa Cruz, Santa Cruz, CA, USA

[144] [a]Departamento de Física, Pontificia Universidad Católica de Chile, Santiago, Chile; [b]Departamento de Física, Universidad Técnica Federico Santa María, Valparaíso, Chile

[145] Department of Physics, University of Washington, Seattle, WA, USA

[146] Department of Physics and Astronomy, University of Sheffield, Sheffield, UK

[147] Department of Physics, Shinshu University, Nagano, Japan

[148] Department Physik, Universität Siegen, Siegen, Germany

[149] Department of Physics, Simon Fraser University, Burnaby, BC, Canada

[150] SLAC National Accelerator Laboratory, Stanford, CA, USA

[151] Physics Department, Royal Institute of Technology, Stockholm, Sweden

[152] Departments of Physics and Astronomy, Stony Brook University, Stony Brook, NY, USA

[153] Department of Physics and Astronomy, University of Sussex, Brighton, UK

[154] School of Physics, University of Sydney, Sydney, Australia

[155] Institute of Physics, Academia Sinica, Taipei, Taiwan

[156] [a]E. Andronikashvili Institute of Physics, Iv. Javakhishvili Tbilisi State University, Tbilisi, Georgia; [b]High Energy Physics Institute, Tbilisi State University, Tbilisi, Georgia

[157] Department of Physics, Technion, Israel Institute of Technology, Haifa, Israel

[158] Raymond and Beverly Sackler School of Physics and Astronomy, Tel Aviv University, Tel Aviv, Israel

[159] Department of Physics, Aristotle University of Thessaloniki, Thessaloníki, Greece

[160] International Center for Elementary Particle Physics and Department of Physics, University of Tokyo, Tokyo, Japan

[161] Graduate School of Science and Technology, Tokyo Metropolitan University, Tokyo, Japan

[162] Department of Physics, Tokyo Institute of Technology, Tokyo, Japan

[163] Tomsk State University, Tomsk, Russia

[164] Department of Physics, University of Toronto, Toronto, ON, Canada

[165] [a]TRIUMF, Vancouver, BC, Canada; [b]Department of Physics and Astronomy, York University, Toronto, ON, Canada

[166] Division of Physics and Tomonaga Center for the History of the Universe, Faculty of Pure and Applied Sciences, University of Tsukuba, Tsukuba, Japan

[167] Department of Physics and Astronomy, Tufts University, Medford, MA, USA

[168] Department of Physics and Astronomy, University of California Irvine, Irvine, CA, USA

[169] Department of Physics and Astronomy, University of Uppsala, Uppsala, Sweden

[170] Department of Physics, University of Illinois, Urbana, IL, USA
[171] Instituto de Física Corpuscular (IFIC), Centro Mixto Universidad de Valencia-CSIC, Valencia, Spain
[172] Department of Physics, University of British Columbia, Vancouver, BC, Canada
[173] Department of Physics and Astronomy, University of Victoria, Victoria, BC, Canada
[174] Fakultät für Physik und Astronomie, Julius-Maximilians-Universität Würzburg, Würzburg, Germany
[175] Department of Physics, University of Warwick, Coventry, UK
[176] Waseda University, Tokyo, Japan
[177] Department of Particle Physics, Weizmann Institute of Science, Rehovot, Israel
[178] Department of Physics, University of Wisconsin, Madison, WI, USA
[179] Fakultät für Mathematik und Naturwissenschaften, Fachgruppe Physik, Bergische Universität Wuppertal, Wuppertal, Germany
[180] Department of Physics, Yale University, New Haven, CT, USA
[181] Yerevan Physics Institute, Yerevan, Armenia

[a] Also at Borough of Manhattan Community College, City University of New York, NY, USA
[b] Also at Centre for High Performance Computing, CSIR Campus, Rosebank, Cape Town, South Africa
[c] Also at CERN, Geneva, Switzerland
[d] Also at CPPM, Aix-Marseille Université, CNRS/IN2P3, Marseille, France
[e] Also at Département de Physique Nucléaire et Corpusculaire, Université de Genève, Geneva, Switzerland
[f] Also at Departament de Fisica de la Universitat Autonoma de Barcelona, Barcelona, Spain
[g] Also at Departamento de Física Teorica y del Cosmos, Universidad de Granada, Granada (Spain), Spain
[h] Also at Department of Applied Physics and Astronomy, University of Sharjah, Sharjah, United Arab Emirates
[i] Also at Department of Financial and Management Engineering, University of the Aegean, Chios, Greece
[j] Also at Department of Physics and Astronomy, University of Louisville, Louisville, KY, USA
[k] Also at Department of Physics and Astronomy, University of Sheffield, Sheffield, UK
[l] Also at Department of Physics, California State University, Fresno, CA, USA
[m] Also at Department of Physics, California State University, Sacramento, CA, USA
[n] Also at Department of Physics, King's College London, London, UK
[o] Also at Department of Physics, St. Petersburg State Polytechnical University, St. Petersburg, Russia
[p] Also at Department of Physics, University of Fribourg, Fribourg, Switzerland
[q] Also at Department of Physics, University of Michigan, Ann Arbor, MI, USA
[r] Also at Dipartimento di Fisica E. Fermi, Università di Pisa, Pisa, Italy
[s] Also at Giresun University, Faculty of Engineering, Giresun, Turkey
[t] Also at Graduate School of Science, Osaka University, Osaka, Japan
[u] Also at Hellenic Open University, Patras, Greece
[v] Also at Horia Hulubei National Institute of Physics and Nuclear Engineering, Bucharest, Romania
[w] Also at II Physikalisches Institut, Georg-August-Universität Göttingen, Göttingen, Germany
[x] Also at Institucio Catalana de Recerca i Estudis Avancats, ICREA, Barcelona, Spain
[y] Also at Institut für Experimentalphysik, Universität Hamburg, Hamburg, Germany
[z] Also at Institute for Mathematics, Astrophysics and Particle Physics, Radboud University Nijmegen/Nikhef, Nijmegen, The Netherlands
[aa] Also at Institute for Particle and Nuclear Physics, Wigner Research Centre for Physics, Budapest, Hungary
[ab] Also at Institute of Particle Physics (IPP), Canada
[ac] Also at Institute of Physics, Academia Sinica, Taipei, Taiwan
[ad] Also at Institute of Physics, Azerbaijan Academy of Sciences, Baku, Azerbaijan
[ae] Also at Institute of Theoretical Physics, Ilia State University, Tbilisi, Georgia
[af] Also at Istanbul University, Dept. of Physics, Istanbul, Turkey
[ag] Also at LAL, Université Paris-Sud, CNRS/IN2P3, Université Paris-Saclay, Orsay, France
[ah] Also at Louisiana Tech University, Ruston, LA, USA
[ai] Also at Manhattan College, New York, NY, USA
[aj] Also at Moscow Institute of Physics and Technology State University, Dolgoprudny, Russia
[ak] Also at National Research Nuclear University MEPhI, Moscow, Russia
[al] Also at Physikalisches Institut, Albert-Ludwigs-Universität Freiburg, Freiburg, Germany

[am] Also at School of Physics, Sun Yat-sen University, Guangzhou, China

[an] Also at The City College of New York, New York, NY, USA

[ao] Also at The Collaborative Innovation Center of Quantum Matter (CICQM), Beijing, China

[ap] Also at Tomsk State University, Tomsk, and Moscow Institute of Physics and Technology State University, Dolgoprudny, Russia

[aq] Also at TRIUMF, Vancouver, BC, Canada

[ar] Also at Universita di Napoli Parthenope, Naples, Italy

[*] Deceased